Physics – Uspekhi **61** (5) 449 – 479 (2018)

60th ANNIVERSARY OF THE BUDKER INSTITUTE OF NUCLEAR PHYSICS (BINP), SB RAS PACS numbers: **32.80. – t**, 41.60.Cr, **42.79. – e**

Beams of photons with nonzero projections of orbital angular momenta: new results

B A Knyazev, V G Serbo

DOI: https://doi.org/10.3367/UFNe.2018.02.038306

Contents

Abstract. Solving Maxwell's equations in cylindrical coordinates yields states in quantum theory with definite values of energy $\hbar\omega$, longitudinal momentum $\hbar k_z$, and total angular momentum projection $\hbar m$ on the z-axis (where $\hbar$ is the Planck constant). Experimentally, values of up to $\hbar m \sim 10^4\hbar$ have been obtained for the last quantity. The wave front of such states is like a meat grinder screw, with the lines of force of the Poynting vector representing the screw line. Such states differ from plane waves by the nonzero orbital angular momentum projection on the direction of motion, and from spherical waves, by the definite direction of motion. For brevity, these states are referred to as 'twisted photons'. In this paper, recent experimental and theoretical results on twisted photons are reviewed, to which the present authors actively contributed. Detailed discussion is given to recent experiments on the production of high-intensity beams of terahertz (wavelength: 140 μm) twisted photons performed on the Novosibirsk free electron laser at the Budker Institute of Nuclear Physics, SB RAS. Recent theoretical work on the interaction of twisted photons with atoms is summarized. Due to their extra degree of freedom — the projection of the total angular momentum on the direction of motion — twisted photons represent a novel research tool of potentially wide application in physics.

Keywords: spin angular momentum, orbital angular momentum, beams of twisted photons, interaction of twisted photons with atoms, terahertz radiation

B A Knyazev Budker Institute of Nuclear Physics,
Siberian Branch of the Russian Academy of Sciences,
prosp. Akademika Lavrent'eva 11, 630090 Novosibirsk,
Russian Federation;
Novosibirsk State University,
ul. Pirogova 2, 630090 Novosibirsk, Russian Federation
E-mail: ba_knyazev@phys.nsu.ru
V G Serbo Novosibirsk State University,
ul. Pirogova 2, 630090 Novosibirsk, Russian Federation;
Sobolev Institute of Mathematics,
Siberian Branch of the Russian Academy of Sciences,
prosp. Akademika Koptyuga 4, 630090 Novosibirsk, Russian Federation
E-mail: serbo@math.nsc.ru

Received 15 January 2018, revised 13 February 2018
Uspekhi Fizicheskikh Nauk **188** (5) 508 – 539 (2018)
DOI: https://doi.org/10.3367/UFNr.2018.02.038306
Translated by E N Ragozin; edited by A Radzig

1. Introduction

1.1 Twisted photons. First acquaintance

This review deals with electromagnetic waves and their corresponding photons–particles that possess a certain projection of the angular momentum on the direction of motion of a wave or a particle. The fact that electromagnetic waves may carry a spin angular momentum (SAM) has long been known. Linearly and circularly polarized photon beams may be described in terms of SAM. This circumstance is mentioned even in Poynting's paper [1] issued in 1909. The first experiment which demonstrated that circularly polarized light beams (beams with an SAM) can transfer angular momentum to a mechanical system was performed [2] in 1936. A round quarter-wave plate in a vacuum was suspended on a fine fiber attached to a rotation axis to make up a torsional pendulum. A circularly polarized light beam passed through the plate, reflected from a mirror, and passed through the plate once again, though with the changed direction of polarization. The plate's torsion demonstrated that a mechanical angular momentum was imparted to the plate.

Apart from spin momentum, radiation may also carry the orbital angular momentum (OAM). The projection $\hbar m_s$ of the SAM of an individual photon may assume only two values, $m_s = \pm 1$, in the units of Planck's constant $\hbar$, while the OAM projection $\hbar m_l$ may assume any integer values $m_l = 0, \pm 1, \pm 2, \pm 3, \ldots$. The projection of the total angular momentum (TAM) of the photon is the sum $\hbar m = \hbar m_s + \hbar m_l$.

It is well known that atomic and nuclear transitions may be attended by the emission of photons with certain values of the TAM and its projection. However, these states correspond to spherical waves and do not possess a certain direction of propagation. Meanwhile, to obtain photon beams with a certain direction of propagation and a nonzero OAM in the pre-laser era was a rather difficult task. The keen interest in beams with an OAM could not arise until the advent of lasers. The interest in beams with an OAM quickened when Allen et al. [3] published their paper in 1992, which is regarded as a pioneering work and is widely cited in modern literature. Proposed in Ref. [3] was a way to produce high-OAM beams by transforming Laguerre–Gaussian laser modes and an experimental scheme for measuring this momentum in its transfer to a mechanical system. Some possible applications of the beams with an OAM were also discussed in Ref. [3]. These states are briefly referred to as *twisted*.[1] Broadly speaking, twisted beams had been mentioned earlier. By way of example, we refer to the work of Baranova and Zel'dovich (see, for instance, Ref. [4]), Vasara et al. [5], and Bazhenov et al. [6, 7]. But Ref. [3] did awaken general interest and lent impetus to further research. In an experimental study by He et al. [8], it was shown that linearly polarized twisted photons gave rise to the rotation of microparticles that absorbed such light, the direction of rotation being determined by the OAM of the photons rather than their polarization. To date, photon beams with a TAM as high as $m = 10{,}010$ have been obtained [9].

It gradually became clear that twisted photons, which possess an additional degree of freedom — projection of the total angular momentum on the direction of its motion — are new and highly helpful research tools which may enjoy wide use in various areas of physics. Over the past 25 years, this research area has turned from a beautiful and exotic isle of laser physics into a broad field of activity involving the generation and use of twisted photons, not only in the optical region, but also in the radio and X-ray ones.

Furthermore, it turned out that other elementary particles, too, in a state with nonzero projection of the orbital angular momentum may find good application in atomic and nuclear physics, and even in elementary particle physics. The first work on the production of twisted electron beams was performed seven years ago, and now there are several hundred theoretical and experimental papers dedicated to twisted electrons (see excellent review [10] and references cited therein). Recently, the production of twisted cold neutrons was first examined experimentally [11], and the first calculation was made of the recombination of such neutrons on protons [12].

In Section 1.2, we present simple formulas for describing the main features of twisted states. In Section 1.3, we briefly review papers pertaining to the production techniques of twisted photons and their application areas. These studies are described in more detail in reviews [13–16]. In these reviews, however, the consideration of twisted light–atom interactions was restricted to only the force action of the light beam on the atom as a whole. Ignored in this case were the excitation and ionization of atoms by twisted photons, which are the main concern of our review.

In Sections 2 and 3, we outline the results of recent (2013–2017) theoretical and experimental work on twisted photons in which the present authors actively participated. Section 2, which was written by V G Serbo, covers a review of theoretical works dedicated to the basic interactions between twisted photons and atoms. Section 3, which was written by B A Knyazev, involves a detailed discussion of the recent experiments on the generation and use of high-power terahertz twisted photons (wavelength: 140 μm) performed at the Novosibirsk free electron laser in the Budker Institute of Nuclear Physics, Siberian Branch of the Russian Academy of Sciences. Since there are no reviews in Russian concerned with methods of twisted beam generation (with the exception of maybe Ref. [13]), we considered it expedient to include in the Introduction a brief discussion of the work on this subject.

1.2 Plane, spherical, and cylindrical (Bessel) waves

Let us recall the well-known facts about electromagnetic waves. Electric, $\mathbf{E}(\mathbf{r}, t)$, and magnetic, $\mathbf{B}(\mathbf{r}, t)$, fields in a vacuum satisfy the Maxwell equations

$$\nabla \times \mathbf{E}(\mathbf{r}, t) = -\frac{1}{c}\frac{\partial \mathbf{B}(\mathbf{r}, t)}{\partial t}\,, \qquad \nabla \times \mathbf{B}(\mathbf{r}, t) = \frac{1}{c}\frac{\partial \mathbf{E}(\mathbf{r}, t)}{\partial t}\,, \quad (1)$$

where c is the speed of light. By introducing the scalar, $A_0(\mathbf{r}, t)$, and vector, $\mathbf{A}(\mathbf{r}, t)$, potentials, which are related to electromagnetic fields by the equations

$$\mathbf{E}(\mathbf{r}, t) = -\nabla A_0(\mathbf{r}, t) - \frac{1}{c}\frac{\partial \mathbf{A}(\mathbf{r}, t)}{\partial t}\,, \quad \mathbf{B}(\mathbf{r}, t) = \nabla \times \mathbf{A}(\mathbf{r}, t)\,, \quad (2)$$

and using the Coulomb calibration of the potentials $A_0(\mathbf{r}, t) = 0$, $\nabla \mathbf{A}(\mathbf{r}, t) = 0$, the Maxwell equations are reduced to the wave equation for the vector potential

$$\left(\nabla^2 - \frac{1}{c^2}\frac{\partial^2}{\partial t^2}\right)\mathbf{A}(\mathbf{r}, t) = 0\,. \quad (3)$$

Next, we will consider the case of monochromatic waves with frequency ω:

$$\mathbf{A}(\mathbf{r}, t) = \mathbf{A}(\mathbf{r})\exp(-\mathrm{i}\omega t)\,, \quad (4)$$

whose amplitudes $\mathbf{A}(\mathbf{r})$ satisfy the Helmholtz equation

$$(\nabla^2 + k^2)\,\mathbf{A}(\mathbf{r}) = 0\,, \quad k = \frac{\omega}{c}\,. \quad (5)$$

For a time, we divert our attention from the vectorial nature of electromagnetic fields (in other words, from the photon spin) and find the solution of Eqn (5) in its scale version:

$$(\nabla^2 + k^2)\,\psi(\mathbf{r}) = 0\,, \quad k = \frac{\omega}{c}\,, \quad (6)$$

using the method of separation of variables.

In Cartesian coordinates x, y, z, we obtain *plane waves*

$$\psi_{\mathbf{k}}(\mathbf{r}) = \exp(\mathrm{i}\mathbf{k}\mathbf{r})\,, \quad (7)$$

which correspond to particles with momentum $\hbar\mathbf{k}$ and energy $\hbar\omega = c\hbar|\mathbf{k}|$ in quantum field theory. In spherical coordinates

[1] In fact, the terminology in this area has not yet become established. These states are also termed *vortex* states and the beams are often referred to as *swirling* or *spiral* beams.

r, θ_r, φ_r, we obtain *spherical waves*

$$\psi_{klm}(\mathbf{r}) = \sqrt{\frac{2\pi}{kr}}\, J_{l+1/2}(kr)\, Y_{lm}(\theta_r, \varphi_r)\,, \tag{8}$$

where $J_n(x)$ is the Bessel function, and $Y_{lm}(\theta_r, \varphi_r)$ is the spherical function. In quantum field theory, particles with momentum modulus $\hbar k$, energy $\hbar\omega = c\hbar k$, the square of the angular momentum $\hbar^2 l(l+1)$, and the z-projection $\hbar m$ of the angular momentum correspond to these solutions.

In cylindrical coordinates ρ, φ_r, z, we obtain *cylindrical* (*or Bessel*) *waves*

$$\psi_{\varkappa m k_z}(\mathbf{r}) = J_m(\varkappa\rho)\exp\left[\mathrm{i}(m\varphi_r + k_z z)\right]. \tag{9}$$

In quantum field theory, particles traveling along the z-axis with longitudinal momentum $\hbar k_z$, transverse momentum modulus $\hbar\varkappa$, energy $\hbar\omega = \hbar c\sqrt{\varkappa^2 + k_z^2}$, and the z-projection $\hbar m$ of the angular momentum correspond to these solutions. These states are briefly termed *twisted*. They differ from plane waves by the existence of a nonzero projection of the orbital angular momentum on the direction of motion, and from spherical waves by the existence of a certain direction of motion. It should be emphasized that precisely the *projection $\hbar m$ of the orbital angular momentum* is determinate for twisted states, while the values of the angular momentum l itself (to be more precise, of the square $\hbar^2 l(l+1)$ of the angular momentum) are undefined and are limited only by the condition $l \geqslant |m|$.

All three solutions are the complete systems of functions, which possess some common features: the functions are dimensionless, their modulus squared remains invariable in time, and any of them may be expressed in terms of a superposition of one of the two other functions. For instance, a plane wave may be represented as a superposition of cylindrical waves:

$$\exp(\mathrm{i}\mathbf{kr}) = \sum_{m=-\infty}^{\infty} \mathrm{i}^m \exp(-\mathrm{i}m\varphi_k)\, \psi_{k_\perp m k_z}(\mathbf{r})\,, \tag{10}$$

where vector $\mathbf{k} = (k_\perp\cos\varphi_k, k_\perp\sin\varphi_k, k_z)$. Similarly, a cylindrical wave may be represented in the form of a superposition of plane waves in the xy plane:

$$\begin{aligned}\psi_{\varkappa m k_z}(\mathbf{r}) &= \exp(\mathrm{i}k_z z)\int a_{\varkappa m}(\mathbf{k}_\perp)\exp(\mathrm{i}\mathbf{k}_\perp\boldsymbol{\rho})\,\frac{\mathrm{d}^2 k_\perp}{(2\pi)^2}\\ &= \int a_{\varkappa m}(\mathbf{k}_\perp)\exp(\mathrm{i}\mathbf{kr})\,\frac{\mathrm{d}^2 k_\perp}{(2\pi)^2}\,,\end{aligned} \tag{11}$$

where the Fourier amplitude

$$a_{\varkappa m}(\mathbf{k}_\perp) = \mathrm{i}^{-m}\exp(\mathrm{i}m\varphi_k)\,\frac{2\pi}{k_\perp}\,\delta(k_\perp - \varkappa) \tag{12}$$

is the eigenfunction of the operator of the z-projection of the orbital angular momentum $\hbar\hat{L}_z = -\mathrm{i}\hbar\,\partial/\partial\varphi_k$ (in the momentum representation) with the eigenvalue $\hbar m$.

Therefore, the plane waves that form a cylindrical wave have wave vectors located on the surface of a cone whose axis is aligned with the z-axis and whose cone angle (*opening angle*)

$$\theta_k = \arctan\frac{\varkappa}{k_z}\,. \tag{13}$$

The so-called *paraxial approximation* corresponds to small values of the opening angle θ_k.

In the limiting case of $\theta_k \to 0$ (in this case, $\varkappa \to 0$, $k_z \to k = \omega/c$, and $J_m(\varkappa\rho) \to \delta_{m0}$), we obtain

$$\psi_{\varkappa m k_z}(\mathbf{r})\Big|_{\theta_k \to 0} \to \delta_{m0}\exp(\mathrm{i}kz)\,, \tag{14}$$

i.e., in this limit and at $m = 0$, the cylindrical wave coincides with a plane wave propagating along the z-axis.

Like plane waves, Bessel waves form a very simple and convenient theoretical construction which corresponds to ideal stationary (nonspreading) states. However, they are nonintegrable[2] in the sense that $\int |\psi_{\varkappa m k_z}(\mathbf{r})|^2\,\mathrm{d}^3 r = \infty$. Instead of such nonintegrable waves, integrable (bounded) waves, which may be represented as the superposition of ideal Bessel waves, are used in a real experiment. In laser physics, for instance, in the domain of paraxial approximation, use is quite often made of so-called *Laguerre–Gaussian* beams, whose transverse (at $z = 0$) distribution, instead of the Bessel shape $\exp(\mathrm{i}m\varphi_r)\,J_m(\varkappa\rho)$, is of the form

$$\psi_n^m(\rho, \varphi_r) = N\exp(\mathrm{i}m\varphi_r)\,x^{|m|}\,L_n^{|m|}(x^2)\exp(-x^2)\,,\quad x = \frac{\sqrt{2}\,\rho}{w}\,, \tag{17}$$

where $L_n^m(x)$ is the generalized Laguerre polynomial, w is the effective beam size, and N is the normalizing constant. The integer n corresponds to the number of zeros in the dependence on variable ρ. Unlike ideal Bessel waves, for which the transverse momentum modulus $\varkappa$ is fixed, Laguerre-Gaussian beams have a distribution over $\varkappa$, so that function $\psi_n^m(\rho, \varphi_r)$ may be represented as a superposition of Bessel waves with different values of $\varkappa$:

$$\begin{aligned}\psi_n^m(\rho, \varphi_r) &= \int_0^\infty g(\varkappa)\exp(\mathrm{i}m\varphi_r)\,J_m(\varkappa\rho)\,\mathrm{d}\varkappa\,,\\ g(\varkappa) &= \frac{N}{\sqrt{2}\,wn!}\left(\frac{\varkappa w}{\sqrt{8}}\right)^{2n+m+1}\exp\left(-\frac{\varkappa^2 w^2}{8}\right).\end{aligned} \tag{18}$$

In those theoretical studies that go beyond the limits of paraxial approximation, use is sometimes made of bounded Bessel waves: the superposition of Bessel waves concentrated in the domain near $\varkappa = \varkappa_0$, which possess a Gaussian distribution with dispersion $\Delta\varkappa$ of the form

$$g(\varkappa) \propto \exp\left[-\frac{(\varkappa - \varkappa_0)^2}{2\Delta\varkappa^2}\right].$$

A detailed description of twisted photons with the inclusion of spin structure is given in Section 2.1. But first, we briefly recall the onset of research in this area.

1.3 Brief survey of experimental and theoretical work on twisted photons

1.3.1 Generation of twisted photons. Shortly after the publication of the article by Allen et al. [3], numerous papers appeared on the generation and application of twisted photon beams in *the optical region*. As regards the methods

[2] Plane waves are normalized to the delta function 'to a $\mathbf{k}/(2\pi)$ scale':

$$\int \psi^*_{\mathbf{k}'}(\mathbf{r})\psi_{\mathbf{k}}(\mathbf{r})\,\mathrm{d}^3 r = (2\pi)^3\delta(\mathbf{k}' - \mathbf{k})\,; \tag{15}$$

a similar relationship for Bessel waves has the form

$$\int \psi^*_{\varkappa' m' k_z'}(\mathbf{r})\,\psi_{\varkappa m k_z}(\mathbf{r})\,\mathrm{d}^3 r = \frac{4\pi^2}{\varkappa}\,\delta(\varkappa' - \varkappa)\,\delta_{m'm}\delta(k_z' - k_z)\,. \tag{16}$$

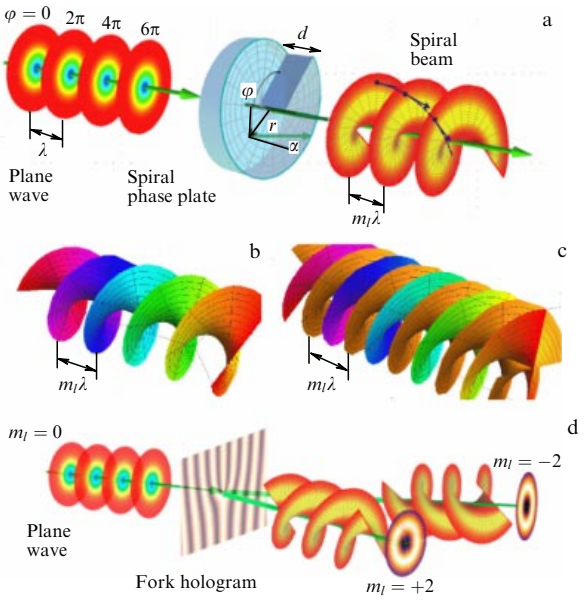

Figure 1. (Color online.) Methods for transforming a plane wave into waves with a helicoidal wave front. (a) Formation with a spiral phase plate; shown to the right of the plate is the beam wave front when $m_l = 1$. Black arrows serve to depict the sequential positions of the Poynting vector, which describes a helical line. (b) Surface of constant phase, and (c) 'embedded' wave fronts with phases of equal modulus 2π (for $m_l = 2$). (d) Helicoidal wave front formation with a fork hologram (figures (1a) and (1d) were borrowed from the site https://wikivisually.com/wiki/Angular_momentum_of_light.)

of their production, these papers may be divided into three groups. Classed with the first group are the studies which employ beams with an on-axis singularity, which naturally emerge in lasers with stable cavities [6, 17]. A popular description of this effect is found in Ref. [18]. However, the technique employed most frequently for producing twisted beams is the transformation of the plane wave fronts of laser radiation into spiral ones with the aid of diffraction optical elements or computer-generated holograms (including the use of spatial light modulators [19, 20]). To become familiar with this technique, the reader is referred to Refs [8, 21–34]. The third method of producing twisted beams involves their generation with the aid of free electrons. For instance, Hemsing et al. [35] implemented a scheme in which electron beams interacted with a laser bunch to acquire a helicoidal structure and subsequently passed through a planar undulator to radiate twisted photons at the fundamental harmonic with a wavelength of 800 nm.

By way of example, Fig. 1 shows two setups for transforming plane waves into beams with an orbital angular momentum. Figure 1a depicts a scheme in which a beam passes through a spiral phase plate, whose optical thickness is constant along radius and linearly increases with azimuth φ as $d = m_l\lambda\varphi/2\pi(n-1)$, where λ is the wavelength in a vacuum, and n is the refractive index of the plate material. This setup demonstrates most clearly the way of forming a spiral wave front. The phase difference of the waves transmitted near the step d in the air and inside the element is equal to $2\pi m_l$, and the wave fronts, which have turned into spiral sections, are perfectly 'stitched' together to form an infinite helicoid. Stitched at $m_l = 1$ are the adjacent wave fronts (for instance, 4π and 6π), and if $m_l = 3$, stitched together are the fronts $\varphi = 0$ and $\varphi = 6\pi$. In this case, the spatial helicoid period along the z-axis is equal to $m_l\lambda$ (Fig. 1b). However, when wave fronts of equal phase are depicted in the wave thus formed, we obtain m_l helical surfaces embedded into each other, the step between them being equal to λ (Fig. 1c).

In the case of a spiral phase plate, it is possible to form only one twisted beam collinear to the incident one. The diffraction of a plane wave from a fork hologram produces a zero-order beam and a set of twisted beams, whose twist orders increase in proportion to their diffraction orders [36]. Two beams of this set with opposite signs of m_l are shown in Fig. 1d. One can see from this example that twisted beams may, in principle, be employed for transmitting two or more signals at one optical frequency. By making a hologram which spatially separates many beams with different m_l values, it is possible to significantly increase the multiplexity of a communication channel.

Twisted X-ray photons with an energy of up to 15 keV were obtained at relativistic electron accelerators in several experiments. As shown in Refs [37, 38], relativistic electrons radiate twisted photons in a spiral undulator at all harmonics with the exception of the fundamental one. This idea was experimentally realized by Bahrdt et al. [39], who produced twisted photon beams in the soft X-ray range (energy: 99 eV) at the second harmonic of a spiral undulator installed at the Berliner Elektronenspeicherring-Gesellschaft für Synchrotronstrahlung II (BESSY-II) accelerator. As shown theoretically in Refs [40, 41], twisted photons of high energy (up to several GeV) can be obtained in the Compton scattering of twisted laser photons from ultrarelativistic electrons. Recently, data from experiments on the nonlinear inverse Compton effect [42] were interpreted by Taira et al. [43] as a consequence of the fact that the photons radiated at the second harmonic with an energy of about 10 keV are twisted photons. A more general investigation [44] shows that twisted photons are emitted at harmonics higher than the first one in the course of a spiral electron motion. A helpful review considering the generation and application of twisted beams in hard ultraviolet and soft X-ray ranges was made in Refs [45, 46].

In the domain of very low photon energies, mention should be made of progress in the generation of twisted photon beams in the *radio frequency* band [47, 48]. Meanwhile, there are only a few papers concerned with the production and investigation of beams with an orbital angular momentum in the *terahertz range*, in the domain between the near-infrared and the radio frequency bands. These papers are considered at length in Section 3.

1.3.2 Applications of twisted photons. To date, twisted photons have found applications in various areas of physics and technology. Without going into details, we briefly mention some of these achievements.

• Among important applications of twisted beams is the optical manipulation of microobjects, including the capture of particles in optical traps, which was minutely described in a thorough review by Soifer et al. [49]. Twisted beams were used for making microfluid pumps in Ref. [50], and for rotating microturbines in Ref. [51]. Evidently, this line of research will be actively developed in the nanotechnology area.

• Tamburini et al. [56] demonstrated (with the addition of a spectacular video available at http://iopscience.iop.org/1367-2630/14/3/033001) the employment of an additional degree of freedom in the form of TAM for increasing the density of communication channels. A detailed review of the

application of twisted beams in communication systems is found in Ref. [57].

• The application of beams with a phase singularity permits achieving superresolution in optical scanning microscopy [52, 53].

• When photographing a binary star, the use of a spiral phase plate in an optical coronograph has made it possible to suppress 97% of the intensity of the bright star with retention of the faint star intensity [54]. An elegant laboratory demonstration of the principle of operation of a 'vortical' optical coronograph was given in Ref. [55].

• Twisted beams of radio waves have been employed for investigating the ionosphere [47].

• Of interest in the area of quantum physics is the investigation of the rotation of Bose–Einstein atomic condensate in traps (see Ref. [15, Section 12.6.2]).

• The rotational velocity of objects was measured from the Doppler frequency shift of reflected twisted photons (see Ref. [15, Section 12.5.4]).

• Discussion is underway of possible applications of twisted photons in quantum informatics, for the production of entangled states of a new type, etc. (see Ref. [58, Section 5]).

A more detailed discussion of these investigations and references to the original work may be found in reviews [15, 16] mentioned above. Recent years have seen an increasing emphasis on the basic interactions of twisted photons with electrons and atoms. In Section 2, we consider the interaction of twisted photons with atoms. In particular, we discuss at length the photoionization and photoexcitation of atoms by twisted photons. Possible applications of twisted terahertz beams are discussed in Section 3.

2. Twisted photons in atomic physics

2.1 Twisted photons and their interaction with atoms. General relationships

In this section, we resume the description of twisted photons and their interactions, begun in the Introduction. In doing so, we restrict ourselves to a discussion of those problems in which only one twisted particle — a photon — in the initial state participates in the processes under consideration. In the general case, we may deal with processes in which two twisted particles interact in the initial state or twisted particles appear in the final state. Of special interest is the question of what reactions yield twisted particles in the final state. We note that the principle problems related to the decay and collisions of twisted particles (to the unusual kinematics of such collisions, in particular) were considered in Refs [40, 41, 59, 60]. However, a technically simple way of revealing the twist degree of the final particles in realistic processes has not been found so far.

2.1.1 Twisted photons. Detailed acquaintance. In this section, we follow mainly our studies [40, 41, 61].

We consider the vector solutions of the Helmholtz equation (5). The solution for plane waves with a certain *helicity* $\Lambda = \pm 1$ of the form

$$\mathbf{A}_{\mathbf{k}\Lambda}(\mathbf{r}) = \mathbf{e}_{\mathbf{k}\Lambda} \exp(\mathrm{i}\mathbf{k}\mathbf{r}) \tag{19}$$

contains the photon polarization vector $\mathbf{e}_{\mathbf{k}\Lambda}$, which is the eigenvector of helicity operator $\hat{\Lambda} = \hat{\mathbf{s}}\mathbf{k}/k$:

$$\hat{\Lambda}\,\mathbf{e}_{\mathbf{k}\Lambda} = \Lambda\,\mathbf{e}_{\mathbf{k}\Lambda}, \tag{20}$$

where $\hat{\mathbf{s}}$ is the photon spin operator, and possesses the following properties:

$$\mathbf{k}\mathbf{e}_{\mathbf{k}\Lambda} = 0\,, \qquad \mathbf{e}^{*}_{\mathbf{k}\Lambda'}\mathbf{e}_{\mathbf{k}\Lambda} = \delta_{\Lambda'\Lambda}\,. \tag{21}$$

Recall that a certain *circular polarization* corresponds to certain values of photon helicity Λ.

It is now evident that cylindrical (Bessel) waves for a *twisted photon* may be constructed in the form of a superposition of vector plane waves (19) by analogy with the scalar case (11):

$$\begin{aligned}\mathbf{A}_{\varkappa m k_z \Lambda}(\mathbf{r}) &= \int a_{\varkappa m}(\mathbf{k}_\perp)\,\mathbf{A}_{\mathbf{k}\Lambda}(\mathbf{r})\,\frac{\mathrm{d}^2 k_\perp}{(2\pi)^2} \\ &= \int a_{\varkappa m}(\mathbf{k}_\perp)\,\mathbf{e}_{\mathbf{k}\Lambda}\exp(\mathrm{i}\mathbf{k}\mathbf{r})\,\frac{\mathrm{d}^2 k_\perp}{(2\pi)^2}\,,\end{aligned} \tag{22}$$

where the Fourier amplitude $a_{\varkappa m}(\mathbf{k}_\perp)$ was defined by expression (12). Our selected polarization vector $\mathbf{e}_{\mathbf{k}\Lambda}$ corresponds to photon spin projection Λ on the direction of the photon momentum $\hbar\mathbf{k}$.

In the integration with respect to $\mathbf{k}_\perp$, we conveniently use the expansion of this vector in terms of the eigenvectors $\boldsymbol{\chi}_\sigma$ of the photon spin projection $\hat{s}_z$ on the z-axis:

$$\hat{s}_z\boldsymbol{\chi}_\sigma = \sigma\boldsymbol{\chi}_\sigma\,, \qquad \sigma = 0, \pm 1\,, \tag{23}$$

where

$$\boldsymbol{\chi}_0 = \begin{pmatrix}0\\0\\1\end{pmatrix}, \quad \boldsymbol{\chi}_{\pm 1} = \mp\frac{1}{\sqrt{2}}\begin{pmatrix}1\\ \pm\mathrm{i}\\0\end{pmatrix}, \quad \boldsymbol{\chi}^{*}_{\sigma'}\boldsymbol{\chi}_\sigma = \delta_{\sigma'\sigma}\,. \tag{24}$$

This expansion takes on the form [62]

$$\mathbf{e}_{\mathbf{k}\Lambda} = \sum_{\sigma=0,\pm 1} \exp(-\mathrm{i}\sigma\varphi_k)\,d^{1}_{\sigma\Lambda}(\theta_k)\,\boldsymbol{\chi}_\sigma\,, \tag{25}$$

where $d^{J}_{MM'}(\theta)$ are small Wigner matrices.[3] We take advantage of this formula and the well-known representation of Bessel functions:

$$\int_0^{2\pi} \exp\left[\mathrm{i}(n\phi + z\cos\phi)\right]\frac{\mathrm{d}\phi}{2\pi} = \mathrm{i}^n J_n(z) \tag{27}$$

to obtain[4]

$$\begin{aligned}\mathbf{A}_{\varkappa m k_z \Lambda}(\mathbf{r}) = \sum_{\sigma=0,\pm 1} \mathrm{i}^{-\sigma}\,d^{1}_{\sigma\Lambda}(\theta_k)\,J_{m-\sigma}(\varkappa\rho)\exp\left[\mathrm{i}(m-\sigma)\varphi_r\right] \\ \times\,\boldsymbol{\chi}_\sigma\exp(\mathrm{i}k_z z)\,.\end{aligned} \tag{30}$$

Figure 2 demonstrates the form of the y-component of this vector potential for $m = 5$, $\sin\theta_k = \varkappa/k = 0.2$, and

[3] The explicit form of these matrices is as follows:

$$\begin{aligned}&d^{1}_{\Lambda,\Lambda}(\theta) = \cos^2\frac{\theta}{2}\,, \quad d^{1}_{-\Lambda,\Lambda}(\theta) = \sin^2\frac{\theta}{2}\,,\\ &d^{1}_{0,\Lambda}(\theta) = \frac{\Lambda}{\sqrt{2}}\sin\theta\,, \quad \Lambda = \pm 1\,.\end{aligned} \tag{26}$$

[4] A similar technique may also be employed in the construction of the wave functions of twisted electrons and neutrons (see Appendix). We also note that relationships similar to relationships (10) and (16) have the form

$$\int \mathbf{A}^{*}_{\varkappa' m' k'_z \Lambda'}(\mathbf{r})\mathbf{A}_{\varkappa m k_z \Lambda}(\mathbf{r})\,\mathrm{d}^3 r = \frac{4\pi^2}{\varkappa}\,\delta(\varkappa' - \varkappa)\delta_{m'm}\delta(k'_z - k_z)\delta_{\Lambda'\Lambda}\,, \tag{28}$$

$$\mathbf{e}_{\mathbf{k}\Lambda}\exp(\mathrm{i}\mathbf{k}\mathbf{r}) = \sum_{m=-\infty}^{\infty}\mathrm{i}^m\exp(-\mathrm{i}m\varphi_k)\,\mathbf{A}_{k_\perp m k_z \Lambda}(\mathbf{r})\,. \tag{29}$$

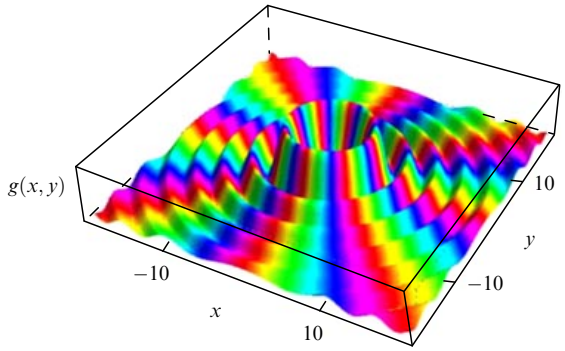

Figure 2. (Color online.) Vector potential (30) of a twisted photon with parameters $m = 5$, $\sin\theta_k = \varkappa/k = 0.2$, and $\Lambda = 1$ [40]. Shown is the modulus squared of the y-component of the vector potential, i.e., the function $g(x,y) = |A^{y}_{\varkappa m k_z \Lambda}(x,y,0)|^2$ in relation to coordinates x and y in the transverse plane (in $1/\varkappa$ units). The phase of the vector potential from zero to 2π is color coded using the rainbow scale.

$\Lambda = 1$. One can clearly see the rings of Bessel maxima and the zero intensity at the origin. From formula (30) and the initial expression (22), it is evident that a twisted photon resides a state with a certain longitudinal momentum $\hbar k_z$, transverse momentum modulus $\hbar\varkappa$, energy $\hbar\omega = \hbar c\sqrt{\varkappa^2 + k_z^2}$, and helicity Λ. Furthermore, individual items

$$\exp\left[\mathrm{i}(m-\sigma)\varphi_r\right]\boldsymbol{\chi}_\sigma \tag{31}$$

in sum (30) are the eigenfunctions of operators $\hat{s}_z$, $\hat{L}_z$, and $\hat{J}_z = \hat{L}_z + \hat{s}_z$ with eigenvalues $m_s = \sigma$, $m_l = m - \sigma$, and m, respectively. The twisted photon therefore possesses a certain value of the z-projection $\hat{J}_z$ of the total angular momentum, equal to m. This quantum number assumes integer values: $m = 0, \pm1, \pm2, \ldots$. At the same time, the twisted photon is the superposition of states in which the z-projection $\hat{s}_z$ of the spin angular momentum assumes values $m_s = 0, \pm1$, and the z-projection $\hat{L}_z$ of the orbital angular momentum takes on the values[5] $m_l = m, m \mp 1$. It is noteworthy that, for $|m| > 1$, the Bessel function $J_{m-\sigma}(\varkappa\rho) \to 0$ as $\rho \to 0$, and the electromagnetic field therefore vanishes at the beam center.

A considerable proportion of experiments on twisted photons are performed for small conic angles θ_k, which corresponds to the so-called *paraxial approximation*. Under these conditions, sum (30) is dominated by the term with $\sigma = \Lambda$:

$$\mathbf{A}_{\varkappa m k_z \Lambda}(\mathbf{r}) \approx \mathrm{i}^{-\Lambda}\cos^4\left(\frac{\theta_k}{2}\right) J_{m-\Lambda}(\varkappa\rho)\exp\left[\mathrm{i}(m-\Lambda)\varphi_r\right] \times \boldsymbol{\chi}_\Lambda \exp\left(\mathrm{i}k_z z\right), \tag{32}$$

and therefore in this approximation the z-projection m of the total angular momentum is unambiguously made up of the spin angular momentum projection, which is approximately Λ, and the projection of the orbital angular momentum, which is approximately $m - \Lambda$. When $m - \Lambda \neq 0$, the electromagnetic field at the center of this beam is equal to zero and the first maximum is about a distance $\rho \approx (m-\Lambda)/(k\sin\theta_k)$ from the beam axis.

Lastly, in the limit $\theta_k \to 0$ (in this case, $\varkappa \to 0$, $k_z \to k = \omega/c$, $d^1_{\sigma\Lambda}(\theta_k) \to \delta_{\sigma\Lambda}$, and $J_{m-\sigma}(\varkappa\rho) \to \delta_{m\sigma}$), we obtain

$$\mathbf{A}_{\varkappa m k_z \Lambda}(\mathbf{r})\Big|_{\theta_k \to 0} \to \delta_{m\Lambda}\,\mathrm{i}^{-\Lambda}\,\boldsymbol{\chi}_\Lambda \exp\left(\mathrm{i}kz\right), \tag{33}$$

i.e., in this limit and at $m = \Lambda$ the cylindrical wave coincides, correct to a phase factor $\mathrm{i}^{-\Lambda}$, with a plane wave propagating along the z-axis.

The electric and magnetic fields of plane-wave photons,

$$\mathbf{E}_{\mathbf{k}\Lambda}(\mathbf{r},t) = \frac{\mathrm{i}\omega}{c}\,\mathbf{e}_{\mathbf{k}\Lambda}\exp\left[\mathrm{i}(\mathbf{kr} - \omega t)\right], \qquad \mathbf{B}_{\mathbf{k}\Lambda}(\mathbf{r},t) = \frac{\mathbf{k}}{k}\times\mathbf{E}_{\mathbf{k}\Lambda}(\mathbf{r},t), \tag{34}$$

are orthogonal to the direction of photon motion — to the vector $\mathbf{k}$ — and correspond to a constant energy density:

$$\frac{|\mathbf{E}_{\mathbf{k}\Lambda}|^2 + |\mathbf{B}^2_{\mathbf{k}\Lambda}|}{4\pi} = \frac{\omega^2}{2\pi c^2} = \frac{k^2}{2\pi}, \tag{35}$$

and a constant energy flux density (a constant Poynting vector) along the direction of the vector $\mathbf{k}$:

$$\mathbf{S} = \frac{c}{2\pi}\,\mathrm{Re}\left(\mathbf{E}_{\mathbf{k}\Lambda}\times\mathbf{B}^*_{\mathbf{k}\Lambda}\right) = \frac{\omega}{2\pi}\,\mathbf{k}. \tag{36}$$

The electric and magnetic fields of twisted photons,

$$\mathbf{E}_{\varkappa m k_z \Lambda}(\mathbf{r},t) = \exp\left[\mathrm{i}(m\varphi_r + k_z z - \omega t)\right]\mathbf{E}(\rho), \qquad \mathbf{B}_{\varkappa m k_z \Lambda}(\mathbf{r},t) = -\mathrm{i}\,\Lambda\mathbf{E}_{\varkappa m k_z \Lambda}(\mathbf{r},t), \tag{37}$$

have components not only in the xy plane transverse to the direction of photon motion, viz.

$$E_\rho(\rho) = -\frac{\omega}{\sqrt{2}c}\left(d^1_{1\Lambda}(\theta_k)\,J_{m-1}(\varkappa\rho) + d^1_{-1,\Lambda}(\theta_k)\,J_{m+1}(\varkappa\rho)\right), \tag{38}$$

$$E_{\varphi_r}(\rho) = -\frac{\mathrm{i}\omega}{\sqrt{2}c}\left(d^1_{1\Lambda}(\theta_k)\,J_{m-1}(\varkappa\rho) - d^1_{-1,\Lambda}(\theta_k)\,J_{m+1}(\varkappa\rho)\right), \tag{39}$$

but also along the z-axis:

$$E_z(\rho) = \frac{\mathrm{i}\omega}{\sqrt{2}c}\,\Lambda J_m(\varkappa\rho)\sin\theta_k, \tag{40}$$

and the surface of constant phase of these fields (for a fixed time) is reminiscent of a meat grinder screw, as shown in Fig. 1a.

The density of twisted photons depends on variable ρ and quantum numbers m and Λ:

$$w^{\mathrm{tw}}(\rho) = \frac{k}{2\pi\hbar c}\sum_{\sigma=0,\,\pm1}\left(d^1_{\sigma\Lambda}(\theta_k)\,J_{m-\sigma}(\varkappa\rho)\right)^2. \tag{41}$$

This function is plotted in Fig. 3 at $\Lambda = 1$ and different values of m. The Poynting vector of a twisted photon possesses not only component S_z along the axis of motion, but also an S_{φ_r} component in the xy plane:

$$S_z(\rho) = \frac{\omega^2}{2\pi c}\,\Lambda\left(\left(d^1_{1\Lambda}(\theta_k)J_{m-1}(\varkappa\rho)\right)^2 - \left(d^1_{-1,\Lambda}(\theta_k)J_{m+1}(\varkappa\rho)\right)^2\right), \tag{42}$$

[5] It is useful to point out that the quantity m_l coincides with the *topological charge* ℓ. The notion of topological charge is widely used in the theory of vortical or helical fields (see reviews [13, 16]). However, the topological charge $\ell = m_l$, which may assume both positive and negative values, must be distinguished from the positive quantity $l \geqslant |m_l|$, which defines the square of the orbital angular momentum $\hbar^2 l(l+1)$.

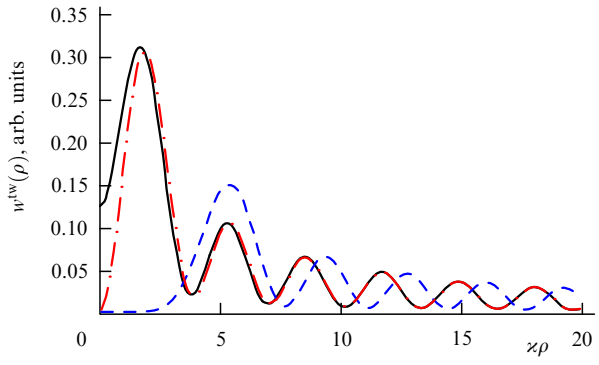

Figure 3. Photon density $w^{\rm tw}(\rho)$ from formula (41) as a function of $\varkappa\rho$ at $\Lambda = 1$, $\theta_k = 30^\circ$, and $m = 0$ (solid curve), $m = 2$ (dashed-dotted curve), and $m = 5$ (dashed curve).

$$S_{\varphi_r}(\rho) = \frac{\omega^2}{2\pi c}\,\Lambda \sin\theta_k\, J_m(\varkappa\rho) \times \left(d^1_{1\Lambda}(\theta_k)\, J_{m-1}(\varkappa\rho) + d^1_{-1,\Lambda}(\theta_k)\, J_{m+1}(\varkappa\rho)\right), \tag{43}$$

$$S_\rho = 0\,. \tag{44}$$

The fact that the Poynting vector is time-independent and $S_\rho = 0$ signify that a twisted wave does not experience spreading. The $\mathbf{S}(\rho)$ vector lines of force at a fixed value of ρ are helical curves $z = (S_z/S_{\varphi_r})\,\rho\varphi_r + \text{const}$ (Fig. 1a).

2.1.2 Interaction between twisted photons and atoms. In this section, we follow mainly our papers [63, 64].

Let us discuss the general issues related to photon–atom interactions [for instance, we will bear in mind processes like photoexcitation or photoionization of atoms (for more details, see Sections 2.2 and 2.3)]. In the ordinary case in the nonrelativistic approximation, the operator of photon interaction with a separate electron (of mass $m_{\rm e}$ and charge $-e$),

$$\hat{V}^{\rm pl} = \frac{e}{m_{\rm e}c}\,\mathbf{A}(\mathbf{r})\,\hat{\mathbf{p}}\,, \qquad \hat{\mathbf{p}} = -\mathrm{i}\hbar\nabla\,, \tag{45}$$

depends linearly on the vector potential $\mathbf{A}(\mathbf{r})$. The same property is inherent in the photon–atom interaction operator

$$\hat{V}^{\rm pl} = \frac{e}{m_{\rm e}c}\sum_a \mathbf{A}_{\mathbf{k}\Lambda}(\mathbf{r}_a)\,\hat{\mathbf{p}}_a\,, \tag{46}$$

where summation is performed over all atomic electrons. It is therefore possible to introduce a convenient interaction characteristic — the *differential cross section* of the process:

$$\mathrm{d}\sigma^{\rm pl} = \frac{\mathrm{d}\dot{W}^{\rm pl}}{j^{\rm pl}}\,, \tag{47}$$

which is defined as the ratio of the corresponding $|i\rangle \to |f\rangle$ transition probability per unit time,

$$\mathrm{d}\dot{W}^{\rm pl} \propto \left|M^{\rm pl}_{fi}\right|^2, \qquad M^{\rm pl}_{fi} = \left\langle f\right|\hat{V}^{\rm pl}\left|i\right\rangle, \tag{48}$$

to the permanent photon flux density $j^{\rm pl}$. Since the photon density has the form

$$w^{\rm pl} = \frac{|\mathbf{E}_{\mathbf{k}\Lambda}|^2 + |\mathbf{B}^2_{\mathbf{k}\Lambda}|}{4\pi\hbar\omega} = \frac{k}{2\pi\hbar c}\,, \tag{49}$$

the photon flux density is expressed as

$$\mathbf{j}^{\rm pl} = \frac{\mathbf{S}}{\hbar\omega} = cw^{\rm pl}\,\frac{\mathbf{k}}{k} = \frac{\mathbf{k}}{2\pi\hbar}\,. \tag{50}$$

The process cross section is convenient in that it is independent of the incident flux and yields information about the character of the photon–atom interaction.

In the case of twisted photon–atom interaction, the perturbation operator is of the form

$$\hat{V}^{\rm tw} = \frac{e}{m_{\rm e}c}\sum_a \mathbf{A}_{\varkappa m k_z \Lambda}(\mathbf{r}_a)\,\hat{\mathbf{p}}_a\,, \tag{51}$$

and the transition probability, as before, is uniquely related to the matrix element of this operator:

$$\mathrm{d}\dot{W}^{\rm tw} \propto \left|M^{\rm tw}_{fi}\right|^2, \qquad M^{\rm tw}_{fi} = \left\langle f\right|\hat{V}^{\rm tw}\left|i\right\rangle. \tag{52}$$

Considering relationship (22) between the vector potentials of the twisted and plane-wave photons, it is easy to determine also the relation between the corresponding matrix elements.

By way of example, we consider the photoexcitation of atomic hydrogen from the initial state $\psi_i(\mathbf{r})$ to the final state $\psi_f(\mathbf{r})$. In this case, account should be taken of the fact that the matrix element $V^{\rm tw}_{fi}$ depends on the impact parameter $\mathbf{b} = b\,(\cos\varphi_b,\, \sin\varphi_b,\, 0)$, which defines the position of the atom relative to the z-axis — the axis of motion of the twisted photon. Therefore, if

$$M^{\rm pl}_{fi}(\mathbf{k}, \Lambda) = \frac{e}{m_{\rm e}c}\int \psi^*_f(\mathbf{r})\mathbf{A}_{\mathbf{k}\Lambda}(\mathbf{r})\,\hat{\mathbf{p}}\psi_i(\mathbf{r})\,\mathrm{d}^3 r\,, \tag{53}$$

then

$$M^{\rm tw}_{fi}(\varkappa, m, k_z, \Lambda, \mathbf{b}) = \frac{e}{m_{\rm e}c}\int \frac{\mathrm{d}^2 k_\perp}{(2\pi)^2}\, a_{\varkappa m}(\mathbf{k}_\perp)\,\psi^*_f(\mathbf{r}-\mathbf{b}) \times \mathbf{A}_{\mathbf{k}\Lambda}(\mathbf{r})\,\hat{\mathbf{p}}\psi_i(\mathbf{r}-\mathbf{b})\,\mathrm{d}^3 r\,. \tag{54}$$

We make the substitution $\mathbf{r} - \mathbf{b} = \mathbf{r}'$ in the above expression and integrate it with respect to $\mathbf{r}'$ to obtain the desired relationship:

$$M^{\rm tw}_{fi}(\varkappa, m, k_z, \Lambda, \mathbf{b}) = \int \frac{\mathrm{d}^2 k_\perp}{(2\pi)^2}\, a_{\varkappa m}(\mathbf{k}_\perp)\exp\left(\mathrm{i}\mathbf{k}_\perp\mathbf{b}\right) M^{\rm pl}_{fi}(\mathbf{k}, \Lambda). \tag{55}$$

In view of the explicit form (12) of function $a_{\varkappa m}(\mathbf{k}_\perp)$, this integral may be reduced to a single integral over the azimuthal angle φ_k of vector $\mathbf{k} = (\varkappa\cos\varphi_k, \varkappa\sin\varphi_k, k_z)$:

$$M^{\rm tw}_{fi}(\varkappa, m, k_z, \Lambda, \mathbf{b}) = \mathrm{i}^{-m}\int_0^{2\pi}\frac{\mathrm{d}\varphi_k}{2\pi}\exp\left[\mathrm{i}m\varphi_k + \mathrm{i}\varkappa b\cos(\varphi_k - \varphi_b)\right] M^{\rm pl}_{fi}(\mathbf{k}, \Lambda)\,. \tag{56}$$

When the atomic wave functions $\psi_i(\mathbf{r})$ and $\psi_f(\mathbf{r})$ describe states with certain values of m_i and m_f of the projection of the angular momentum onto the z-axis, the dependence of $M^{\rm pl}_{fi}(\mathbf{k}, \Lambda)$ on the azimuthal angle φ_k is entirely defined by the factor $\exp\left[\mathrm{i}(m_i - m_f)\varphi_k\right]$, and, therefore, the integration with respect to φ_k may be performed analytically [see expression (27)]:

$$\mathrm{i}^{-m}\int_0^{2\pi}\frac{\mathrm{d}\varphi_k}{2\pi}\exp\left[\mathrm{i}(m + m_i - m_f)\varphi_k + \mathrm{i}\varkappa b\cos\left(\varphi_k - \varphi_b\right)\right] = \mathrm{i}^{m_i - m_f}\exp\left[\mathrm{i}(m + m_i - m_f)\varphi_b\right] J_{m+m_i-m_f}(\varkappa b)\,. \tag{57}$$

Eventually, the matrix element of the twisted photon turns out to be related to the matrix elements of a plane-wave photon by a simple algebraic relationship, which proves to be highly convenient for further calculations. Furthermore, the dependence of the matrix element of the twisted photon on the impact parameter is entirely defined by the sole factor $J_{m+m_i-m_f}(\varkappa b)$.

An important feature of twisted waves is the fact that the photon flux density $S_z(\rho)/(\hbar\omega)$ along the direction of wave propagation is neither constant nor positively defined [see expression (42)]. This means that there is no way of introducing a standard definition of the cross section for the processes involving twisted photons and that this notion has to be generalized. We discuss one such generalization (which, of course, is not the only possible one) in more detail. In doing so, we will proceed from the requirement that our generalized cross section coincide with the standard one in the limit $\theta_k \to 0$. We will also have to take into consideration that the twisted photon–atom interaction probability $\mathrm{d}\dot{W}^{\mathrm{tw}}(\mathbf{b})$ depends on the impact parameter $\mathbf{b}$, which defines the atom's position relative to the axis of motion of the twisted photon.

Let a twisted photon propagate along the z-axis and its density $w^{\mathrm{tw}}(\rho)$ [see expression (41)] be a positively defined function of coordinates in the transverse plane dependent on the quantum numbers m and Λ. Notice that

$$w^{\mathrm{tw}}(\rho)\Big|_{\theta_k\to 0} = \frac{k}{2\pi\hbar c}\,\delta_{m\Lambda}\,, \tag{58}$$

i.e., in this limit, the standard expression (49) for the density at $m = \Lambda = \pm 1$ is recovered. Furthermore, at $m = \Lambda = \pm 1$, the density is nonzero at the origin:

$$w^{\mathrm{tw}}(\rho)\Big|_{\rho\to 0} = \frac{k}{2\pi\hbar c}\cos^4\left(\frac{\theta_k}{2}\right). \tag{59}$$

Therefore, the definition of the density of twisted-photon flux along the z-axis, which is convenient for the subsequent discussion, is naturally introduced by the following expression

$$\begin{aligned} j_z^{\mathrm{tw}}(\rho) &= v_z w^{\mathrm{tw}}(\rho, m=\Lambda=1) \\ &= \frac{k\cos\theta_k}{2\pi\hbar}\left[\cos^4\left(\frac{\theta_k}{2}\right) J_0^2(\varkappa\rho) + \frac{1}{2}\sin^2\theta_k\, J_1^2(\varkappa\rho)\right. \\ &\quad \left. + \sin^4\left(\frac{\theta_k}{2}\right) J_2^2(\varkappa\rho)\right], \end{aligned} \tag{60}$$

where $v_z = c\cos\theta_k$. This expression is a positively defined function, has a good plane-wave limit

$$j_z^{\mathrm{tw}}(\rho)\Big|_{\theta_k\to 0} = \frac{k}{2\pi\hbar}\,, \tag{61}$$

and is nonzero at the origin.

First, we consider the case of the simplest experiment formulation, when the target is *macroscopic* and corresponds to atoms quite uniformly distributed over the entire transverse plane. In this case, the process is conveniently characterized by the *differential cross section* $\mathrm{d}\bar{\sigma}^{\mathrm{tw}}$ *averaged over the impact parameters of atoms* in a domain of large radius $\mathcal{R}$. We define $\mathrm{d}\bar{\sigma}^{\mathrm{tw}}$ as the ratio between the transition probability integrated with respect to the impact parameters and the quantity

$$J_z = \int j_z^{\mathrm{tw}}(\rho)\,\mathrm{d}^2\rho = \frac{k\mathcal{R}}{\pi\hbar\varkappa}\cos\theta_k\,, \tag{62}$$

i.e., to the twisted-photon flux density $j_z^{\mathrm{tw}}(\rho)$ integrated with respect to $\boldsymbol{\rho}$ over the same domain of large radius $\mathcal{R}$. As a result, the averaged cross section is defined as

$$\mathrm{d}\bar{\sigma}^{\mathrm{tw}} = \frac{1}{J_z}\int \mathrm{d}^2 b\;\mathrm{d}\dot{W}^{\mathrm{tw}}(\mathbf{b})\,. \tag{63}$$

It may be shown (see, for instance, Ref. [63, Section II.B]) that the averaged cross section is independent of the artificially introduced parameter $\mathcal{R}$ and is expressed as follows:

$$\mathrm{d}\bar{\sigma}^{\mathrm{tw}} = \int_0^{2\pi}\frac{\mathrm{d}\varphi_k}{2\pi}\,\frac{\mathrm{d}\sigma^{\mathrm{pl}}(\mathbf{k})}{\cos\theta_k}\,. \tag{64}$$

In the limit $\theta_k \to 0$, the thus defined cross section coincides with the standard plane-wave cross section. One can see from formula (64) that the averaged cross section depends on the conical angle θ_k of the twisted photon, but is independent of the quantum number m. Of course, the absence of dependence on the projection m of the total angular momentum substantially impoverishes the information obtained with this simple experiment set-up. However, mention should immediately be made of an experiment modification that partly recovers this dependence. For instance, when the initial state is a coherent superposition of two twisted states with different projection values m_1 and m_2, the averaged cross section may depend on the difference $m_2 - m_1$.

Let us consider the case when the target is bounded, its center is displaced a distance $\mathbf{b}_{\mathrm{t}}$ from the beam axis, and the classical distribution of atoms inside the target is described by the function $n(\mathbf{b}-\mathbf{b}_{\mathrm{t}})$, the impact parameter $\mathbf{b}$ being, as before, the distance of an individual target atom from the beam axis. For brevity, this target will be termed *mesoscopic*. In this case, the process is conveniently characterized by the differential cross section $\mathrm{d}\sigma^{\mathrm{tw}}(\mathbf{b}_{\mathrm{t}})$ averaged over the impact parameters of the atoms of the bounded target. The differential cross section is defined as follows:

$$\mathrm{d}\sigma^{\mathrm{tw}}(\mathbf{b}_{\mathrm{t}}) = \frac{1}{\mathcal{J}_z}\int \mathrm{d}^2 b\, n(\mathbf{b}-\mathbf{b}_{\mathrm{t}})\,\mathrm{d}\dot{W}^{\mathrm{tw}}(\mathbf{b})\,, \tag{65}$$

where $\mathcal{J}_z$ is the twisted-photon flux density (60) integrated with respect to $\boldsymbol{\rho}$ with consideration for the atomic distribution in the *nondisplaced target*:

$$\mathcal{J}_z = \int j_z^{\mathrm{tw}}(\rho)\, n(\boldsymbol{\rho})\,\mathrm{d}^2\rho\,. \tag{66}$$

In the limiting case, when the target consists of one ion located a distance $\mathbf{b}$ from the beam axis, function $n(\mathbf{b}) = \delta(\mathbf{b})$ and the corresponding cross section is defined as

$$\mathrm{d}\sigma^{\mathrm{tw}}(\mathbf{b}) = \frac{2\pi\hbar}{k\cos\theta_k\cos^4(\theta_k/2)}\;\mathrm{d}\dot{W}^{\mathrm{tw}}(\mathbf{b})\,. \tag{67}$$

For specific calculations, below we will use the Gaussian distribution

$$n(\mathbf{b}-\mathbf{b}_{\mathrm{t}}) = \frac{1}{2\pi w^2}\exp\left[-\frac{(\mathbf{b}-\mathbf{b}_{\mathrm{t}})^2}{2w^2}\right], \tag{68}$$

which is usually realized in ion traps, with dispersion w characterizing the target size. In this case, integration in expression (66) may be performed analytically:

$$\mathcal{J}_z = \frac{\omega\cos\theta_k}{2\pi c}\left[\cos^4\left(\frac{\theta_k}{2}\right) I_0(\varkappa^2 w^2) + \frac{1}{2}\sin^2\theta_k\, I_1(\varkappa^2 w^2) + \sin^4\left(\frac{\theta_k}{2}\right) I_2(\varkappa^2 w^2)\right]\exp\left(-\varkappa^2 w^2\right). \quad (69)$$

Here, $I_n(x)$ is the Bessel function of an imaginary argument. With the use of formulas (65) and (69), it is easily shown that cross section (65) when $\theta_k \to 0$ coincides with the standard one (47); for a large target size, $w \to \infty$; coincides with cross section (64) for a macroscopic target; and for a small target size, $w \to 0$, coincides with cross section (67), which corresponds to scattering by a separate atom.

2.2 Photoexcitation of atoms by twisted photons

2.2.1 Relation between matrix elements; selection rules. Picón et al. [65] considered the excitation of atoms with the twisted photons of a Laguerre–Gaussian beam by proceeding from the numerical solution of the nonrelativistic Schrödinger equation and obtained new selection rules in the paraxial approximation. To calculate the transition amplitude, Afanasev et al. [66] used the coordinate representation of the twisted-photon wave function and obtained selection rules beyond the framework of the paraxial approximation. They also discovered that the dependence of transition amplitude on the impact parameter is determined by a simple factor in the form of the Bessel function of argument $\varkappa b$.

The next substantial step was made in our paper [63], in which advantage was taken of the momentum representation of the twisted-photon wave function, and we obtained the important relationships (55), (56) between the transition amplitudes induced by twisted and plane-wave photons. This permitted performing a detailed analysis of the $1s \to 2p$ and $2p \to 3d$ transitions in hydrogen atoms, including the basic characteristics of the subsequent fluorescence emission (after the excitation of atoms by twisted photons). Let us consider these issues in more detail.

Let the initial and final states of a hydrogen atom be defined by the wave functions $\psi_i(\mathbf{r}) = \psi_{n_i l_i m_i}(\mathbf{r})$ and $\psi_f(\mathbf{r}) = \psi_{n_f l_f m_f}(\mathbf{r})$, which are the well-known solutions of the nonrelativistic Schrödinger equation (here, n is the principal quantum number, l and m are the orbital angular momentum and its projection on the z-axis). The twisted photon has projection m_γ of the total angular momentum on the same z-axis. In this case, the transition matrix element,

$$M^{\rm pl}_{m_f m_i}(\theta_k, \varphi_k, \Lambda) \equiv M^{\rm pl}_{fi}(\mathbf{k}, \Lambda) = \frac{e}{m_e c}\int \psi^*_{n_f l_f m_f}(\mathbf{r})\mathbf{A}_{\mathbf{k}\Lambda}(\mathbf{r})\,\hat{\mathbf{p}}\,\psi_{n_i l_i m_i}(\mathbf{r})\,{\rm d}^3 r', \quad (70)$$

when the plane-wave photon moves along the z'-axis parallel to vector $\mathbf{k}$, may be expressed in terms of the matrix elements $M^{\rm pl}_{m'_f m'_i}(0,0,\Lambda)$ of a photon moving along the z-axis. The frame of reference $S'(x', y', z')$ with the z'-axis may be obtained from the frame $S(x, y, z)$ with the z-axis by way of rotation through an angle θ_k about the y-axis, and through an angle ϕ_k about the z-axis, and therefore

$$\psi_{nlm}(\mathbf{r}) = \exp({\rm i}m\varphi_k)\sum_{m'=-l}^{l} d^{\,l}_{mm'}(\theta_k)\,\psi_{nlm'}(\mathbf{r}'). \quad (71)$$

Using relationship (71), we obtain

$$M^{\rm pl}_{m_f m_i}(\theta_k, \varphi_k, \Lambda) = \exp\left[{\rm i}(m_i - m_f)\varphi_k\right] \times \sum_{m'_f m'_i} d^{\,l_f}_{m_f m'_f}(\theta_k)\, d^{\,l_i}_{m_i m'_i}(\theta_k) M^{\rm pl}_{m'_f m'_i}(0,0,\Lambda). \quad (72)$$

The matrix element $M^{\rm pl}_{m_f m_i}(0,0,\Lambda)$ corresponds to the plane-wave photon propagating along the z-axis with helicity Λ, and, therefore, the conservation law for the projection of the angular momentum leads to the well-known selection rules:

$$m_f = m_i + \Lambda, \qquad l_f \geqslant |m_f|. \quad (73)$$

As a result, the double sum turns into a single one:

$$M^{\rm pl}_{m_f m_i}(\theta_k, \varphi_k, \Lambda) = \exp\left[{\rm i}(m_i - m_f)\varphi_k\right] \times \sum_{m'_i} d^{\,l_f}_{m_f, m'_i+\Lambda}(\theta_k)\, d^{\,l_i}_{m_i m'_i}(\theta_k) M^{\rm pl}_{m'_i+\Lambda, m'_i}(0,0,\Lambda), \quad (74)$$

and a very simple relation results for the 1s initial atomic state:

$$M^{\rm pl}_{m_f, m_i=0}(\theta_k, \varphi_k, \Lambda) = \exp(-{\rm i}\Lambda\varphi_k) d^{\,l_f}_{m_f \Lambda}(\theta_k)\, M^{\rm pl}_{\Lambda 0}(0,0,\Lambda). \quad (75)$$

We use expressions (57) and (74) to obtain the main formula linking the matrix elements for twisted and plane-wave photons:

$$M^{\rm tw}_{m_f m_i}(m_\gamma, \Lambda, \mathbf{b}) \equiv M^{\rm tw}_{fi}(\varkappa, m_\gamma, k_z, \Lambda, \mathbf{b}) = {\rm i}^{\,m_i - m_f}\exp\left[{\rm i}(m_\gamma + m_i - m_f)\varphi_b\right] J_{m_\gamma + m_i - m_f}(\varkappa b) \times \sum_{m'_i} d^{\,l_f}_{m_f, m'_i+\Lambda}(\theta_k)\, d^{\,l_i}_{m_i m'_i}(\theta_k) M^{\rm pl}_{m'_i+\Lambda, m'_i}(0,0,\Lambda). \quad (76)$$

Hence, it is easy to obtain the following *selection rules* for the matrix element with a twisted photon:

• when the atom is located on the z-axis,

$$m_f = m_i + m_\gamma, \qquad l_f \geqslant |m_f|, \quad (77)$$

since $J_n(\varkappa b) = \delta_{n0}$ at $b = 0$;

• for $b \neq 0$, there are no limitations on the quantum number m_f, i.e.,

$$m_f \text{ is arbitrary}, \qquad l_f \geqslant |m_f|. \quad (78)$$

It is noteworthy that

$$M^{\rm tw}_{m_f m_i}(m_\gamma, \Lambda, \mathbf{b})\Big|_{\theta_k \to 0} \to {\rm i}^{-\Lambda} M^{\rm pl}_{m_f m_i}(0,0,\Lambda)\,\delta_{m_\gamma \Lambda}, \quad (79)$$

i.e., the standard expression recovers in this limit, because in this case $\varkappa \to 0$, $J_n(\varkappa b) \to \delta_{n0}$, and $d^{\,l}_{mm'}(\theta_k) \to \delta_{mm'}$.

2.2.2 Macroscopic target. By taking advantage of relationships (64) and (74), in the simple case of the interaction between a twisted photon and a macroscopic target, it is possible to obtain the averaged partial cross section:

$$\bar{\sigma}^{\rm tw}_{m_f}(\theta_k, \Lambda) = \frac{4\pi^2 c}{\omega\cos\theta_k}\frac{1}{2l_i + 1} \times \sum_{m_i}\left|M^{\rm pl}_{m_f m_i}(\theta_k, \varphi_k = 0, \Lambda)\right|^2 \delta(\hbar\omega + E_i - E_f). \quad (80)$$

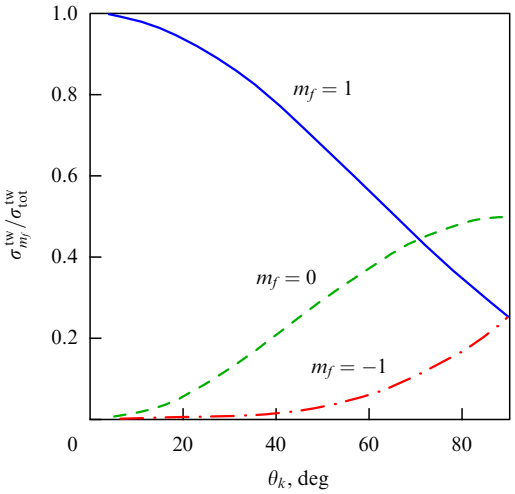

Figure 4. Relative values of the partial cross sections $\sigma^{\rm tw}_{m_f}(\theta_k, \Lambda)/\sigma^{\rm tw}_{\rm tot}(\theta_k, \Lambda)$ for the 1s → 2p photoexcitation of atomic hydrogen by a twisted photon as functions of the conical angle θ_k of this photon [63].

Cross section (80) is independent of the projection m_γ of the total angular momentum of the photon, but is sensitive to the magnitude of the transverse momentum $\varkappa = (\omega/c)\sin\theta_k$ of the twisted photon. For the transition 1s → $n_f l_f m_f$ from the ground state this formula is simplified:

$$\bar{\sigma}^{\rm tw}_{m_f}(\theta_k, \Lambda) = \frac{d^{\,l_f}_{m_f\Lambda}(\theta_k)}{\cos\theta_k}\,\sigma^{\rm pl}_{\rm tot}(\theta_k = 0, \Lambda)\,. \tag{81}$$

We consider the 1s → 2p transition. Let, for definiteness, the photon helicity $\Lambda = 1$. In this case, a plane-wave photon will be able to excite only the 2p state with projection $m_f = \Lambda = 1$. But the twisted photon participates in the excitation of all three 2p states with projections $m_f = 0, \pm 1$, as shown in Fig. 4. Only the $m_f = 1$ state is excited at an angle $\theta_k = 0$, i.e., the results for the twisted photon coincide with the standard ones. With an increase in this angle, the $m_f = 0$ and $m_f = -1$ states also come to experience excitation, the excitation cross section for the $m_f = 0$ state turning out to be greater than the excitation cross section for the $m_f = 1$ state for angles $\theta_k > 71°$. As a consequence, the polarization of the subsequent fluorescence radiation may greatly differ from that in the standard case. Let us consider the linear polarization of such radiation (the α line in the Lyman series) when the photon is emitted at a right angle to the z-axis, assuming that the fine structure of the 2p level is unresolved. The corresponding Stokes parameter

$$P_1 = \frac{I_\parallel - I_\perp}{I_\parallel + I_\perp}\,, \tag{82}$$

where $I_\parallel$ and $I_\perp$ are the intensities of light polarized linearly in the reaction plane formed by the z-axis and the direction of momentum vector and polarized perpendicular to this plane, respectively. Using formulas (81), it is possible to calculate that

$$P_1(\theta_k) = \frac{3 + 9\cos(2\theta_k)}{-47 + 3\cos(2\theta_k)}\,. \tag{83}$$

With reference to Fig. 5, in the paraxial mode (when $\theta_k \lesssim 5°$) the parameter $P_1(\theta_k) \approx -0.3$, which corresponds to

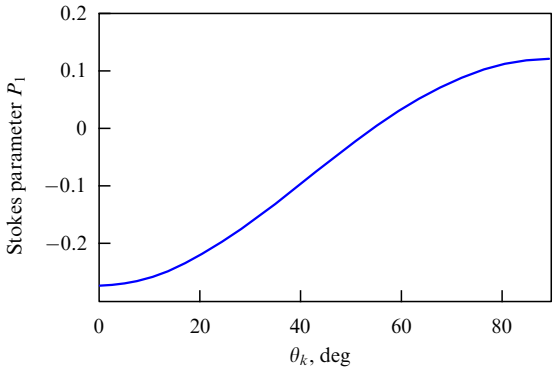

Figure 5. Stokes parameter (83) of the Lyman-α fluorescence radiation following the 1s → 2p excitation of atomic hydrogen by twisted light as a function of the conical angle θ_k [63].

a significant polarization *perpendicular* to the reaction plane. As the angle θ_k increases, the situation qualitatively changes, and for $\theta_k > 58°$, parameter $P_1(\theta_k)$ becomes positive, which corresponds to the radiation polarized primarily in the reaction plane. This change in fluorescence radiation polarization in relation to the conical angle θ_k of the twisted photon may be easily examined in experiments, and it may yield valuable information about the twisted beam–atom interaction.

Using the formalism developed by Scholz–Marggraf et al. [63], Afanasev et al. [67, 68] analyzed new possibilities for multipole transitions induced by twisted photons. Among other theoretical work, mention should be made of Ref. [69] concerned with the excitation of Rydberg atoms by Laguerre–Gaussian beams, of Ref. [70], in which new selection rules were found with the inclusion of the nuclear recoil effect, and of Ref. [71], which studied twisted photon–atom interactions in the impact parameter representation.

Owing to its simplicity, the case of a macroscopic target of hydrogen atoms considered in Ref. [63] is highly convenient for illustrating general relationships. The much more complicated case of the excitation of many-electron atoms and ions by twisted light was considered in the framework of the relativistic Dirac equation in our paper [72]. Special emphasis was placed on the populations of the magnetic sublevels of excited atomic states described with the aid of alignment parameters. A general expression was obtained for these parameters in Ref. [72] in the case when the photon beam is prepared as a coherent superposition of two twisted Bessel waves incident on a macroscopic target. That is, instead of the vector potential (22), use was made of the superposition of such potentials with two different values, m_1 and m_2, of the projection of the total angular momentum, but with equal values of the longitudinal momentum $\hbar k_z$, transverse momentum modulus $\hbar\varkappa$, energy $\hbar\omega = \hbar c\sqrt{\varkappa^2 + k_z^2}$, and helicity Λ:

$$\begin{aligned} &c_1 \mathbf{A}_{\varkappa m_1 k_z \Lambda}(\mathbf{r}) + c_2 \mathbf{A}_{\varkappa m_2 k_z \Lambda}(\mathbf{r})\,, \\ &c_n = |c_n|\exp(\mathrm{i}\alpha_n)\,, \quad |c_1|^2 + |c_2|^2 = 1\,. \end{aligned} \tag{84}$$

The qualitative difference between the cases of a single Bessel beam and the superposition of two Bessel beams is clearly seen, even from the transverse energy density distribution pattern shown in Fig. 6. While this distribution for one beam (Fig. 6a) possesses cylindrical (azimuthal) symmetry for any m_1 value, for two beams (Figs 6b–6d) this symmetry is

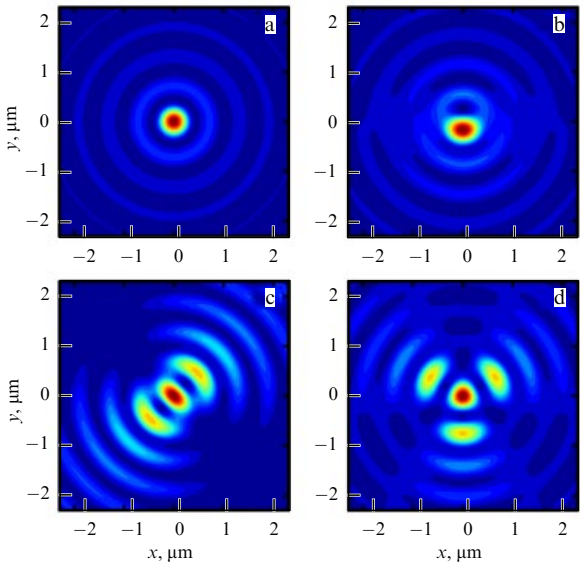

Figure 6. (Color online.) Energy density in the transverse plane, which corresponds to a single Bessel beam (22) or the superposition of two Bessel beams (84) with different projections of the total angular momentum [72]. (a) One beam with $m_1 = 1$; (b) two beams with $m_1 = 1$ and $m_2 = 2$; (c) two beams with $m_1 = 1$ and $m_2 = 3$, and (d) two beams with $m_1 = 1$ and $m_2 = 4$. The results were obtained for a conical angle $\theta_k = 45°$, photon energy $\hbar\omega = 2{,}104$ eV, and phases $\alpha_1 = 0$ and $\alpha_2 = \pi/2$. The energy density (in arb. units) is color-coded, the transition from blue to red corresponding to increasing energy density.

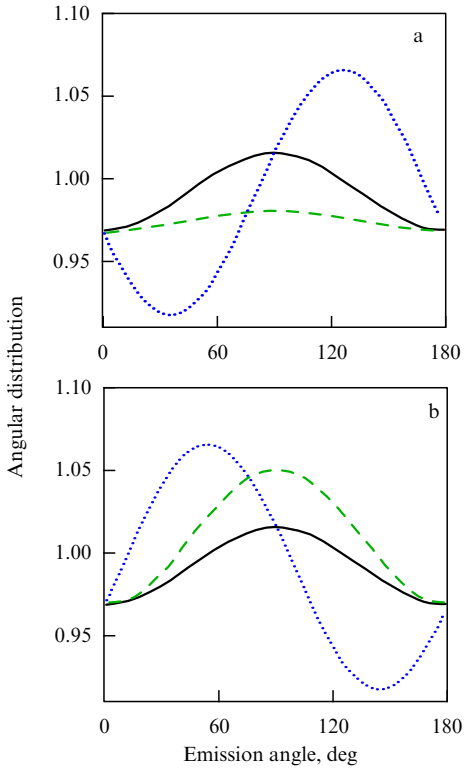

Figure 7. Normalized angular distribution of the fluorescence radiation corresponding to the $3p\,^2P_{3/2} \to 3s\,^2S_{1/2}$ transition following the excitation of a macroscopic target of Na atoms ($Z = 11$) by the coherent superposition (84) of two Bessel beams [72]. The beams were prepared in the state with a conical angle $\theta_k = 60°$, and phases $\alpha_1 = 0, \alpha_2 = \pi/3$ (a) and $\alpha_1 = 0, \alpha_2 = 4\pi/3$ (b). Projections of the total angular momentum $m_1 = 1$ and $m_2 = 2$ (dotted curves), $m_1 = 1$ and $m_2 = 3$ (dashed curves), and $m_1 = 1$ and $m_2 = 4$ (solid curves).

broken and the distribution depends heavily on the difference between the quantum numbers $m_{1,2}$ as well as on the $\alpha_{1,2}$ phase difference.

In the case of two beams, the populations of excited atom sublevels turn out to be sensitive not only to the conical angle of the initial photons, but also to the projections of their total angular momenta. Although the resultant formulas may be used for describing the photoexcitation of any atoms, irrespective of their shell structure and the number of electrons, specific calculations were carried out for the $3s \to 3p$ transition in sodium. These calculations suggest that the twist of the initial photon beam may result in measurable changes to alignment parameters of the excited $^2P_{3/2}$ state and changes to the angular distribution of subsequent fluorescence radiation. By way of example we cite from Ref. [72] the normalized angular distributions for the $3p\,^2P_{3/2} \to 3s\,^2S_{1/2}$ transition in sodium after two-beam photoexcitation (Fig. 7).

2.2.3 Mesoscopic target. In our study [64], we considered the interaction of twisted light with a mesoscopic target of hydrogen atoms. In this case, the atomic target is assumed to have a Gaussian spatial distribution (68). A theoretical analysis of the process was performed in the framework of the nonrelativistic Born approximation. Expressions were calculated for the excitation cross section and for the alignment parameters of individual atomic states.

Let us discuss in more detail the results for the $1s \to 2p$ transition, which are instructive for a comparison with the results of calculations for the macroscopic target given above. It is clear *a priori* that in the mesoscopic target case it is possible to gather much more information about the light–atom interaction itself, as well as of the target or twisted-light parameters. In particular, when the target dimensions are comparable to the spacing of Bessel intensity rings in the incident beam, one might expect that the measurements of excitation probabilities and fluorescence radiation polarizations in relation to target transverse displacement may be validly used for diagnosing the beam.

The relative total excitation cross sections $R \equiv \sigma_{\rm tot}^{\rm tw}(\theta_k, m_\gamma, \Lambda)/\sigma_{\rm tot}^{\rm pl}(\Lambda)$ are plotted in Fig. 8 as functions of the target size w (Figs 8a and 8b) and the distance $b_{\rm t}$ between the target center and the beam axis (Figs 8c and 8d). As is seen in Figs 8a and 8b, for an atomic target under 200 nm in size, twisted photons with different m_γ values exert a significant effect on the population of magnetic sublevels of the 2p excited state. For targets of significantly greater size, the excitation cross sections tend to a common limit: $R = 1/\cos\theta_k = 1.06$ corresponding to the macroscopic target. At the same time, in the case of a small target size, as is clear from Figs 8c and 8d, the dependence of R on the impact parameter is quite close to the intensity distribution of a beam twisted in the transverse plane (Fig. 9).

The Stokes parameter P_1, which characterizes the linear polarization (82) of fluorescence radiation, is plotted in relation to the target size w and the distance $b_{\rm t}$ from the target center to the beam axis in Fig. 10. As is seen in Figs 10a and 10b, for an atomic target under 200 nm in size, the twisted photons with different m_γ values have a highly significant effect on the polarization of the subsequent (fluorescence) radiation. On the other hand, the P_1 parameter is hardly dependent on m_γ and $b_{\rm t}$ for a target of appreciably larger size.

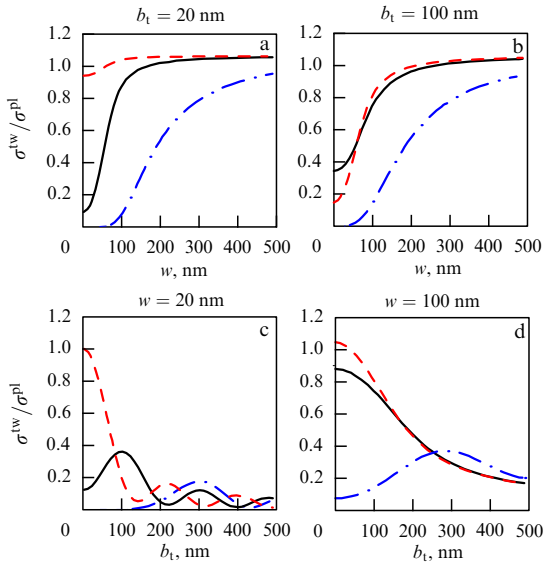

Figure 8. Relative total cross sections $\sigma_{tot}^{tw}(\theta_k, m_\gamma, \Lambda)/\sigma_{tot}^{pl}(\Lambda)$ for the twisted-photon excitation (conical angle $\theta_k = 20°$, helicity $\Lambda = 1$) of the $1s \to 2p$ transition in a mesoscopic target of hydrogen atoms [64]. The cross sections are presented in relation to the target size w for two distances between the beam axis and the target center: $b_t = 20$ nm (a) and $b_t = 100$ nm (b), as well as in relation to the target center position b_t for two target sizes: $w = 20$ nm (c) and $w = 100$ nm (d). The dependences are given for three projections of the total angular momentum of the twisted beam: $m_\gamma = 0$ (solid curves), $m_\gamma = 1$ (dashed curves), and $m_\gamma = 5$ (dashed–dotted curves).

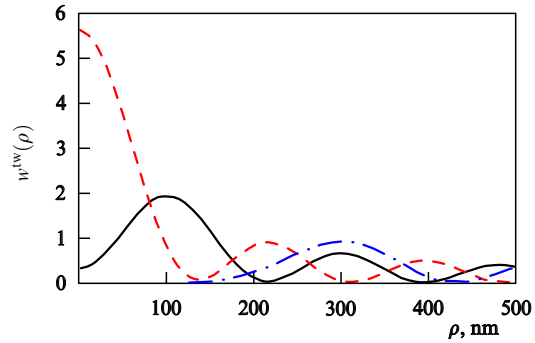

Figure 9. Twisted-photon beam density $w^{tw}(\rho)$ (41) in relation to the distance ρ from the beam axis in the transverse plane. The photon energy $\hbar\omega = 10.2$ eV corresponds to the $1s \to 2p$ transition energy in hydrogen atoms, the conical angle $\theta_k = 20°$, and helicity $\Lambda = 1$. Solid curve — $m_\gamma = 0$; dashed curve — $m_\gamma = 1$, and dashed–dotted curve — $m_\gamma = 5$.

One can clearly see in Figs 10c and 10d that the Stokes parameter oscillates upon shifting a target of small size ($w = 20$ nm), the positions of the first peaks for $m_\gamma = 1$ and $m_\gamma = 5$ being in a qualitative agreement with the positions of such peaks in the twisted-light intensity curves (see Fig. 9).

These calculations for a mesoscopic target were initiated by the experiments of Schmiegelow et al. [73], who studied the Laguerre–Gaussian beam excitation of $^{40}Ca^+$ ions in the form of a well-localized target under 60 nm in size in an ion trap. The data from a new experiment of this type were recently compared [74] in detail with the data obtained from numerical calculations. The new data were given as a function of the position of a single-ion $^{40}Ca^+$ target relative to the twisted-beam axis. These data agreed nicely with the corresponding theoretical calculations.

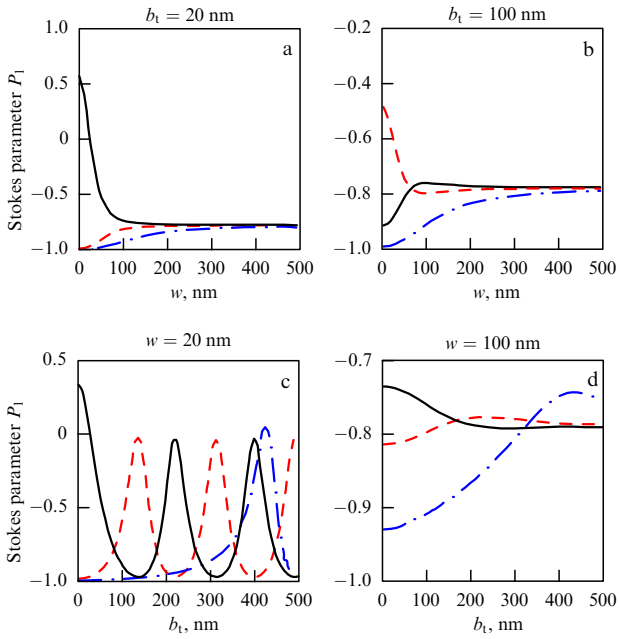

Figure 10. The same as in Fig. 8, but for the Stokes parameter P_1 (82) of $2p \to 1s$ fluorescence radiation following mesoscopic target excitation by twisted photons [64].

2.3 Photoionization of atoms by twisted photons

One of the first investigations of atomic ionization by twisted photons in the paraxial approximation was made by Picón et al. [65, 75], who considered numerical solutions of the nonrelativistic Schrödinger equation for the interaction of hydrogen atoms with the photons of a Laguerre–Gaussian beam. For the first time, this made it possible to consider the time evolution of electrons in the course of ionization.

2.3.1 Nonrelativistic Born approximation. The ionization of a hydrogenlike atom with a nuclear charge Ze by twisted light was considered beyond the framework of paraxial approximation in our paper [61], where the calculation was performed in the nonrelativistic Born approximation. As is well known, the small parameters in this approximation are not only the quantity $Z\alpha$, but also the parameter

$$v = Z\alpha\,\frac{c}{v}\,, \qquad \alpha = \frac{e^2}{\hbar c} \approx \frac{1}{137}\,, \tag{85}$$

where v is the final electron velocity. To state it in different terms, the electron velocity must satisfy the conditions $Z\alpha c \ll v = p/m_e \ll c$. In this approximation, the electron spin may be disregarded and use can be made of the nonrelativistic atomic wave function $\psi_i(\mathbf{r}) = \psi_{nlm}(\mathbf{r})$, while the wave function of the final electron may be taken in the form of a plane wave $\psi_f(\mathbf{r}) = \exp(\mathrm{i}\mathbf{pr}/\hbar)$ with momentum $\mathbf{p}$. Substituting these wave functions into formula (53), in the standard case we obtain the matrix element in the form

$$M_\Lambda^{pl}(\mathbf{k}, \mathbf{p}) = \frac{e}{m_e c}\,(\mathbf{e}_{\mathbf{k}\Lambda}\mathbf{p})\,\tilde{\psi}_{nlm}(\mathbf{q})\,, \qquad \mathbf{q} = \mathbf{p} - \hbar\mathbf{k}\,, \tag{86}$$

where $\tilde{\psi}_{nlm}(\mathbf{q})$ is the Fourier image of function $\psi_{nlm}(\mathbf{r})$ (see formula (A.1) in Ref. [61]). Using formula (56), we arrive at

$$M_\Lambda^{tw}(m_\gamma, \mathbf{p}, \mathbf{b}) = \frac{e\,\mathrm{i}^{-m_\gamma}}{m_e c}\int_0^{2\pi}(\mathbf{e}_{\mathbf{k}\Lambda}\mathbf{p}) \times \exp\left[\mathrm{i}m_\gamma\varphi_k + \mathrm{i}\varkappa b\cos(\varphi_k - \varphi_b)\right]\tilde{\psi}_{nlm}(\mathbf{q})\,\frac{\mathrm{d}\varphi_k}{2\pi}\,. \tag{87}$$

The subsequent integration over angle φ_k leads to rather complex expressions, which were employed in the original paper by Matula et al. [61], who obtained and considered at length only the normalized angular distributions of the final electron for a target involving a single atom.

However, it is possible to derive appreciably simpler formulas when it is considered that the inequality $\hbar k \ll p$ is fulfilled under the approximation in use, which permits making the substitution

$$\tilde{\psi}_{nlm}(\mathbf{q}) \to \tilde{\psi}_{nlm}(\mathbf{p}) = \tilde{R}_{nl}(p)\, Y_{lm}(\theta_p, \varphi_p) \tag{88}$$

and performing integration with respect to φ_k by applying formulas (24) and (25):

$$M_{\Lambda}^{\mathrm{tw}}(m_\gamma, \mathbf{p}, \mathbf{b}) = \frac{ep}{m_e c}\, \tilde{\psi}_{nlm}(\mathbf{p}) \exp\left(\mathrm{i} m_\gamma \varphi_b\right) G(\theta_p, \varphi_p)\,, \tag{89}$$

where the factor

$$\begin{aligned} G(\theta_p, \varphi_p) &= \sum_{\sigma=0,\pm1} \mathrm{i}^{-\sigma} \exp\left[\mathrm{i}\sigma(\varphi_p - \varphi_b)\right] G_\sigma(\theta_p)\,, \\ G_\sigma(\theta_p) &= \sqrt{\frac{4\pi}{3}}\, d^1_{\sigma\Lambda}(\theta_k) J_{m_\gamma - \sigma}(\varkappa b)\, Y_{1\sigma}(\theta_p, \varphi_p = 0)\,, \end{aligned} \tag{90}$$

is independent of the quantum numbers of the atomic state but depends on the impact parameter **b**. Whence follows the normalized electron angular distribution in the form

$$W_{\Lambda}^{\mathrm{tw}}(\theta_p, \varphi_p) = N \left| Y_{lm}(\theta_p, 0)\, G(\theta_p, \varphi_p) \right|^2, \tag{91}$$

where

$$\begin{aligned} \left|G(\theta_p, \varphi_p)\right|^2 &= B + C\sin(\varphi_p - \varphi_b) + D\cos\left[2(\varphi_p - \varphi_b)\right], \\ B = G_1^2 + G_0^2 + G_{-1}^2\,, &\quad C = 2G_0(G_1 + G_{-1})\,, \quad D = -2G_1 G_{-1}\,, \end{aligned} \tag{92}$$

and the normalizing coefficient N is defined by the condition

$$\int W_{\Lambda}^{\mathrm{tw}}(\theta_p, \varphi_p)\, \mathrm{d}\Omega_p = 1 \tag{93}$$

or the condition

$$\frac{1}{N} = \int \left| Y_{lm}(\theta_p, 0) \right|^2 (G_0^2 + G_1^2 + G_{-1}^2)\, \mathrm{d}\Omega_p\,. \tag{94}$$

It is well known that in the case of a plane-wave photon with a given helicity Λ the angular distribution is independent of the azimuthal escape angle φ_p of a final electron. By contrast, in the case of twisted photons, one might expect a significant azimuthal asymmetry, especially for those values of impact parameter b whereby the photon density varies most rapidly and, therefore, the phase of the incident wave would also be expected to vary rapidly. This is precisely why it is interesting to trace the angular distribution over φ_p as a function of the projection m_γ of the total angular momentum of the twisted photon and the atom's distance b from the beam axis. To this end, we represent distribution (91) in the form

$$\begin{aligned} W_{\Lambda}^{\mathrm{tw}}(\theta_p, \varphi_p) &= N \left| Y_{lm}(\theta_p, 0) \right|^2 \\ &\times B\Big\{1 + A_1 \sin(\varphi_p - \varphi_b) + A_2 \cos\left[2(\varphi_p - \varphi_b)\right]\Big\}, \end{aligned} \tag{95}$$

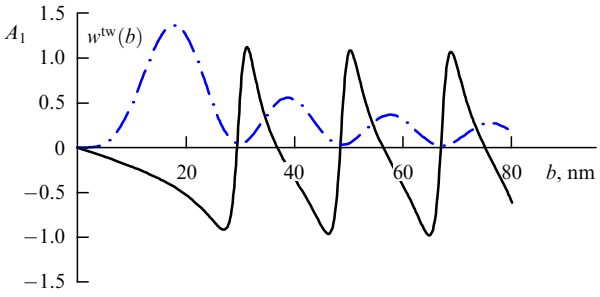

Figure 11. Parameter A_1 (96) (solid curve) of the azimuthal asymmetry of final electron escape as a function of the distance b of an atom's transverse displacement from the beam axis. Twisted photon energy is 100 eV. Projection of the total angular momentum $m_\gamma = 3$, helicity $\Lambda = 1$, conical angle $\theta_k = 20°$, electron polar escape angle $\theta_p = 45°$. Also shown for comparison is the twisted-photon beam density $w^{\mathrm{tw}}(b)$ (41) (dashed-dotted curve, arb. units).

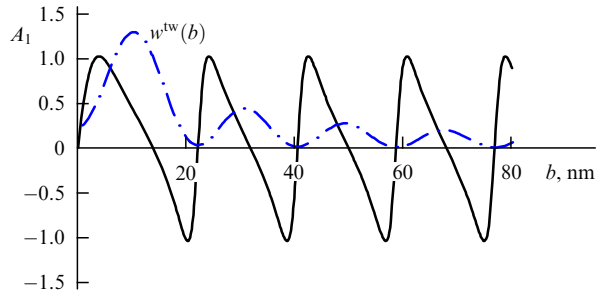

Figure 12. The same as in Fig. 11, but at $m_\gamma = 0$.

in which the azimuthal asymmetry parameters,

$$A_1 = \frac{C}{B} = \frac{2G_0(G_1 + G_{-1})}{G_0^2 + G_1^2 + G_{-1}^2}\,, \quad A_2 = \frac{D}{B} = -\frac{2G_1 G_{-1}}{G_0^2 + G_1^2 + G_{-1}^2}\,., \tag{96}$$

are explicitly separated out. It is remarkable that *these parameters possess some universality*: *they are independent of the atomic state*.

We consider the behavior of these parameters in relation to an atom's displacement b along the x-axis (i.e., at $\varphi_b = 0$). The twisted photons will be assumed to have an energy of 100 eV, a helicity $\Lambda = 1$, and a conical angle $\theta_k = 20°$. For definiteness, we fix the electron polar escape angle: $\theta_p = 45°$. Function $A_1(b)$ is plotted in Fig. 11 for a twisted photon with $m_\gamma = 3$ (solid curve). Shown for comparison is the dependence of the twisted-photon density $w^{\mathrm{tw}}(b)$ (41) (the dashed–dotted curve). Similar curves for the $m_\gamma = 0$ case are plotted in Fig. 12. One can see that the azimuthal asymmetry turns out to be significant and exhibits appreciable correlations with the photon density distribution in the beam. In the examples under consideration, parameter A_2 (96) turns out to be smaller by nearly an order of magnitude: $|A_2| < 0.062$.

2.3.2 Going beyond the framework of the Born approximation. The ionization of a hydrogenlike atom by a twisted photon was treated more exactly and comprehensively in our study [76] with consideration of relativistic effects and the final electron interaction with the atomic nucleus. In outlining these results, we will use the relativistic units $c = 1$ and $\hbar = 1$, in which $e^2 = \alpha \approx 1/137$. In other words, parameters $Z\alpha$ and

$v = Z\alpha/v$ are not assumed to be small. Considered in Ref. [76] was not only the normalized angular distribution, but also the more detailed characteristics of the process, including the twisted-photon absorption cross section by atomic targets of various sizes. It should be noted that the photoionization of a hydrogenlike atom is the process inverse to radiative recombination, which was recently considered beyond the framework of the Born approximation in our paper [77]. Some formulas may therefore be obtained by simple substitutions in the corresponding formulas for the recombination.

The final electron in this approximation is described by the exact solution $\Psi^{(-)}_{\mathbf{p}\lambda}(\mathbf{r})$ of the Dirac equation, whose asymptotic form contains a plane wave $\psi_{\mathbf{p}\lambda}(\mathbf{r})$ along with an ingoing spherical wave:

$$\Psi^{(-)}_{\mathbf{p}\lambda}(\mathbf{r}) \underset{r\to\infty}{\longrightarrow} \psi_{\mathbf{p}\lambda}(\mathbf{r}) + G^{(-)}_{\lambda}(\mathbf{n}_p, \mathbf{n}_r)\,\frac{\exp(-\mathrm{i}pr)}{r}\,, \tag{97}$$

where $\mathbf{n}_p = \mathbf{p}/p$ and $\mathbf{n}_r = \mathbf{r}/r$. The plane wave $\psi_{\mathbf{p}\lambda}(\mathbf{r})$ represents a state with a certain momentum $\mathbf{p}$, energy $\varepsilon = \sqrt{\mathbf{p}^2 + m_\mathrm{e}^2}$, and helicity λ:

$$\psi_{\mathbf{p}\lambda}(\mathbf{r}) = u_{\mathbf{p}\lambda}\exp(\mathrm{i}\mathbf{p}\mathbf{r})\,, \tag{98}$$

where $u_{\mathbf{p}\lambda}$ is the Dirac bispinor (see Appendix for details). This function is normalized by the condition

$$\int \bar{\psi}_{\mathbf{p}\lambda}(\mathbf{r})\,\psi_{\mathbf{p}'\lambda'}(\mathbf{r})\,\mathrm{d}^3 r = (2\pi)^3\delta(\mathbf{p}-\mathbf{p}')\,2m_\mathrm{e}\,\delta_{\lambda\lambda'}\,. \tag{99}$$

The normalization condition for the function $\Psi^{(-)}_{\mathbf{p}\lambda}(\mathbf{r})$ is determined by long distances and therefore remains the same as for the function $\psi_{\mathbf{p}\lambda}(\mathbf{r})$.

The standard matrix element of the reaction (see Ref. [78, § 56 and § 57]) is given by

$$M^{\mathrm{pl}}_{\Lambda\lambda}(\mathbf{k},\mathbf{p}) = \int \Psi^{(-)\,\dagger}_{\mathbf{p}\lambda}(\mathbf{r})\big(\boldsymbol{\alpha}\mathbf{A}_{\mathbf{k}\Lambda}(\mathbf{r})\big)\psi_i(\mathbf{r})\,\mathrm{d}^3 r\,, \tag{100}$$

where α is the Dirac vector matrix defining the ionization probability and the differential cross section:

$$\frac{\mathrm{d}\sigma^{\mathrm{pl}}_{\Lambda\lambda}}{\mathrm{d}\Omega_p} = \frac{1}{j_z}\frac{\mathrm{d}\dot{W}^{\mathrm{pl}}}{\mathrm{d}\Omega_p} = \frac{\alpha}{4\pi}\frac{p}{\omega}\left|M^{\mathrm{pl}}_{\Lambda\lambda}(\mathbf{k},\mathbf{p})\right|^2. \tag{101}$$

The matrix element for ionization by a twisted photon, as before, is conveniently expressed in terms of the standard matrix element:

$$M^{\mathrm{tw}}_{\Lambda\lambda}(\varkappa, m_\gamma, k_z, \mathbf{p}, \mathbf{b}) = \mathrm{i}^{-m_\gamma}\int_0^{2\pi} M^{\mathrm{pl}}_{\Lambda\lambda}(\mathbf{k},\mathbf{p})\exp\left[\mathrm{i}m_\gamma\varphi_k + \mathrm{i}\varkappa b\cos(\varphi_k-\varphi_b)\right]\frac{\mathrm{d}\varphi_k}{2\pi}\,, \tag{102}$$

with vector $\mathbf{k} = (\varkappa\cos\varphi_k, \varkappa\sin\varphi_k, k_z)$ in this formula. In the limit of $\theta_k \to 0$ at $m_\gamma = \Lambda = \pm 1$, this matrix element coincides with the standard expression. The subsequent calculations were performed numerically with the use of the modified Radial code package [79], which is required for finding the radial parts of the solution to the Dirac equation for an electron in the central field of an extended nucleus.

For details of the calculations and an extensive description of the results obtained, we refer the reader to the original study [76]. Here, we consider only the nonrelativistic case, i.e., the final electron velocity is assumed to be low, $v \ll 1$, but parameter $v = Z\alpha/v$ is not assumed to be small. It would be instructive to compare the results obtained in this approximation with the Born approximation. In the nonrelativistic approximation, the electron spin may be ignored and simplifications can be made in the matrix element (100), corresponding to the dipole approximation. (For the subsequent calculations, see book [78, § 56].) When the photoionization occurs from the ground state of a hydrogenlike atom, the matrix element is expressed as

$$M^{\mathrm{pl}}_{\Lambda}(\mathbf{p},\mathbf{k}) = \sqrt{\frac{8\pi F(v)}{m_\mathrm{e}p(1+v^2)}}\,(\mathbf{n}_p\mathbf{e}_{\mathbf{k}\Lambda})\,, \qquad F(v) = 2^5\pi\,\frac{v^6}{(1+v^2)^2}\,\frac{\exp(-4v\,\mathrm{arccot}\,v)}{1-\exp(-2\pi v)}\,. \tag{103}$$

The differential cross section takes on the form

$$\frac{\mathrm{d}\sigma^{\mathrm{pl}}_{\Lambda}}{\mathrm{d}\Omega_p} = \frac{\alpha}{m_\mathrm{e}^2}\,\frac{\mathbf{p}^2}{\omega^2}\,F(v)\,|\mathbf{n}_p\mathbf{e}_{\mathbf{k}\Lambda}|^2\,. \tag{104}$$

This cross section is independent of Λ and φ_p, and is minimum in the forward and backward directions (for $\mathbf{k} = (0,0,\omega)$):

$$\frac{\mathrm{d}\sigma^{\mathrm{pl}}_{\Lambda}}{\mathrm{d}\Omega_p} = \frac{\alpha}{2m_\mathrm{e}^2}\,\frac{\mathbf{p}^2}{\omega^2}\,F(v)\,\sin^2\theta_p\,. \tag{105}$$

In the Born approximation (for $v \to 0$), the function $F(v) = 16\,v^5$. The ratio of the cross section (104) obtained with consideration of the exact wave function of the final electron to the Born cross section is independent of the electron escape angle, and the photon polarization is expressed as

$$R(v) = \frac{\mathrm{d}\sigma^{\mathrm{pl}}_{\Lambda}/\mathrm{d}\Omega_p}{\mathrm{d}\sigma^{(\mathrm{pl,\,Born})}_{\Lambda}/\mathrm{d}\Omega_p} = \frac{2\pi v}{(1+v^2)^2}\,\frac{\exp(-4v\,\mathrm{arccot}\,v)}{1-\exp(-2\pi v)}\,. \tag{106}$$

This function declines rapidly with increasing parameter v (Fig. 13).

The differential and total cross sections averaged over the initial photon polarizations are of the form

$$\frac{\mathrm{d}\sigma^{\mathrm{pl}}}{\mathrm{d}\Omega_p} = W^{\mathrm{pl}}(\theta_p)\,\sigma^{\mathrm{pl}}\,, \qquad \sigma^{\mathrm{pl}} = \frac{4\pi\alpha}{3m_\mathrm{e}^2}\,\frac{\mathbf{p}^2}{\omega^2}\,F(v)\,, \tag{107}$$

where the normalized angular distribution

$$W^{\mathrm{pl}}(\theta_p) = \frac{3}{8\pi}\sin^2\theta_{\mathbf{pk}} = \frac{1}{4\pi}\left[1 - P_2(\cos\theta_{\mathbf{pk}})\right], \qquad P_2(x) = \frac{1}{2}\,(3x^2-1) \tag{108}$$

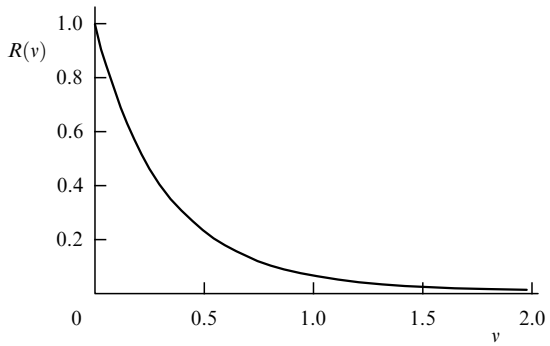

Figure 13. Function $R(v)$ described by expression (106).

does not differ from that in the Born approximation. The function $W^{\rm pl}(\theta_p)$ has a maximum in the direction perpendicular to vector $\mathbf{k}$.

We use formula (102) to find the explicit form of the matrix element for the twisted-photon ionization from the ground state:

$$M_{\Lambda}^{\rm tw}(\varkappa, m_\gamma, k_z, \mathbf{p}, \mathbf{b}) = \sqrt{\frac{8\pi}{m_{\rm e} p}\,\frac{F(v)}{1+v^2}}\,\exp\left(i m_\gamma \varphi_p\right) G(\theta_p, \varphi_p)\,, \tag{109}$$

where function $G(\theta_p, \varphi_p)$ is defined by expression (90).

Let us compare the resultant data with the Born approximation, in which parameter v is assumed to be small. By way of example, we consider the ionization of a hydrogen atom by a 100-eV photon, which was discussed in Ref. [61]. In this case, the final electron is nonrelativistic and its velocity is low, $v = 0.018$, but parameter ν is no longer small: $\nu = 0.4$. This leads to a ratio $R = 0.31$ [see formula (106)], i.e., this value is one third that of the Born value. When we consider the ionization of an ion with a charge $Z = 2$ by the same photon, the ratio $R = 0.056$, i.e., 18 times smaller than the Born one. It is noteworthy that considered in Ref. [61] were only the normalized angular distributions and not the absolute values of the differential cross sections. As it turned out, the exact and Born values coincide for this distribution both for plane-wave and twisted photons!

It should be emphasized, however, that the departure from the Born approximation for photon energies on the order of 10 eV, which were discussed in Ref. [80], are highly significant; for instance, at $\omega = 15$ eV and $Z = 1$, the ratio $R = 0.0036$.

Next, we consider the twisted-photon ionization of different hydrogen targets described in Sections 2.2.2 and 2.2.3.

Single-atom target. When the target consists of one atom located at a distance b from the twisted-photon beam axis, the total cross section has the form [see formula (67)]

$$\sigma^{\rm tw}(\varkappa, m_\gamma, b) = \frac{\sigma^{\rm pl}}{2\cos\theta_k \cos^4(\theta_k/2)} \times \left\{2J_{m_\gamma}^2(\varkappa b)\sin^2\theta_k + \left[J_{m_\gamma-1}^2(\varkappa b) + J_{m_\gamma+1}^2(\varkappa b)\right](1+\cos^2\theta_k)\right\}. \tag{110}$$

Figure 14 depicts the ratio of this cross section to the standard cross section $\sigma^{\rm pl}$ (107) as a function of distance b.

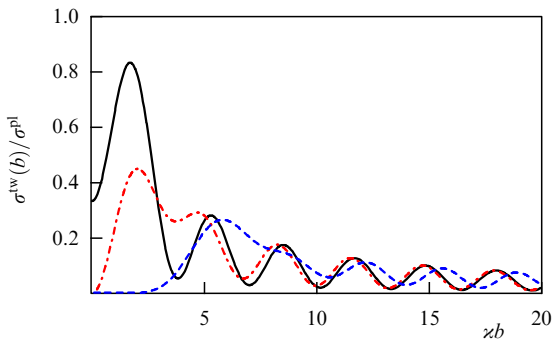

Figure 14. Ratio $\sigma^{\rm tw}(\varkappa, m_\gamma, b)/\sigma^{\rm pl}$ from formula (110) as a function of $\varkappa b$ at $\Lambda = 1$, $\theta_k = 30°$, and $m_\gamma = 0$ (solid curve), $m_\gamma = 2$ (dashed–dotted curve), and $m_\gamma = 5$ (dashed curve).

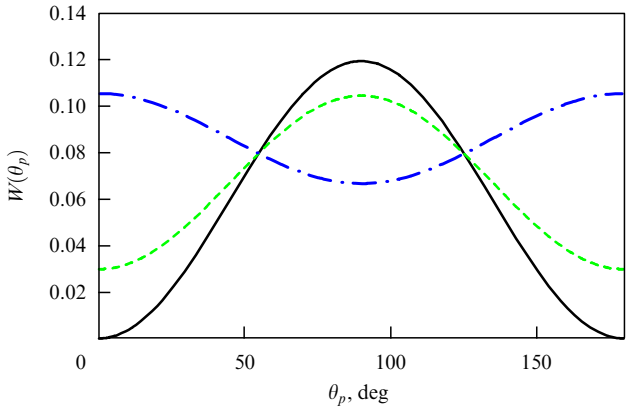

Figure 15. Normalized angular distribution $W_{\Lambda}^{\rm tw}(\theta_p)$ (112) for a macroscopic target at three values of the conical angle: $\theta_k = 1°$ (solid curve), $\theta_k = 30°$ (dashed curve), and $\theta_k = 70°$ (dashed–dotted curve).

When these curves are compared with the twisted-photon density curves in Fig. 3 for the same values of quantum numbers m_γ and Λ, it becomes evident that the single-atom target is highly sensitive to the density variations of the incident twisted photon.

Macroscopic target. Twisted photons with a certain J_z value. Using the formulas derived above, it is easily shown that the differential cross section averaged over the impact parameters of the atoms may be expressed in terms of the standard total cross section $\sigma^{\rm pl}$ defined by expression (107):

$$\frac{{\rm d}\bar{\sigma}_{\Lambda}^{\rm tw}}{{\rm d}\Omega_p} = \frac{\sigma^{\rm pl}}{\cos\theta_k}\,W_{\Lambda}^{\rm tw}(\theta_p)\,, \tag{111}$$

where the normalized angular distribution of final electrons,

$$W_{\Lambda}^{\rm tw}(\theta_p) \equiv \frac{1}{\bar{\sigma}_{\Lambda}^{\rm tw}}\frac{{\rm d}\bar{\sigma}_{\Lambda}^{\rm tw}}{{\rm d}\Omega_p} = \frac{1}{4\pi}\left(1 - P_2(\cos\theta_k)\,P_2(\cos\theta_p)\right), \tag{112}$$

depends on the photon conical angle θ_k, and not on the projection m_γ of the total angular momentum of the photon.

At $\theta_k = 0$, this distribution coincides with the standard one [compare with formula (108)]. One can also see that *this distribution is a universal function independent of the photon helicity Λ and parameter ν*. This circumstance justifies the application of the Born approximation in the calculation of the normalized angular distribution in Ref. [61]. Distribution (112) is plotted in Fig. 15 at $\theta_k = 1°$, $30°$, and $70°$. Unlike the distribution in the plane-wave case [see expression (105)], this distribution has a minimum in the forward and backward directions only when $\theta_k < \theta_{\rm cr} = \arcsin\sqrt{2/3} \approx 55°$. By contrast, for $\theta_k > \theta_{\rm cr}$, a minimum is reached at $\theta_p = 90°$, while this distribution has maxima in the forward and backward directions. At $\theta_k = \theta_{\rm cr}$, the angular distribution becomes isotropic: $W^{\rm tw}(\theta_p) = 1/(4\pi)$. It is noteworthy that the quantity $W_{\Lambda}^{\rm tw}(\theta_p)$ possesses symmetry with respect to the substitution $\theta_p \to \pi - \theta_p$; this property is violated with the inclusion of relativistic corrections.

Macroscopic target. Twisted photons in the form of a superposition of two states with different values of J_z. Consider the case when a macroscopic target is exposed to a photon beam prepared as a coherent superposition of two twisted Bessel waves with two different values, m_1 and m_2, of the

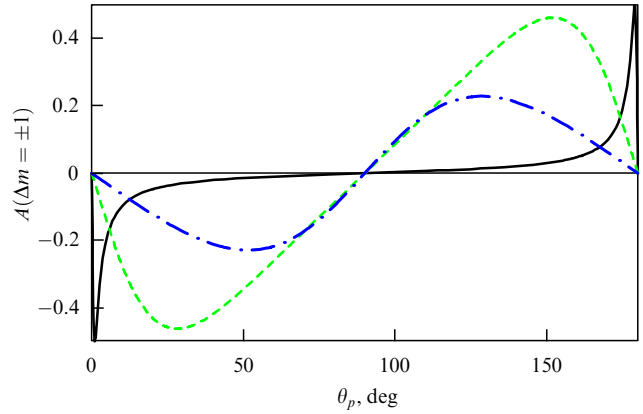

Figure 16. Azimuthal asymmetry parameter $A(\theta_p)$ (114) at $\Delta m = \pm 1$ for three values of the conical angle of a twisted photon: $\theta_k = 1°$ (solid curve), $\theta_k = 30°$ (dashed curve), and $\theta_k = 70°$ (dashed–dotted curve), at $|c_1 c_2| = 1/2$.

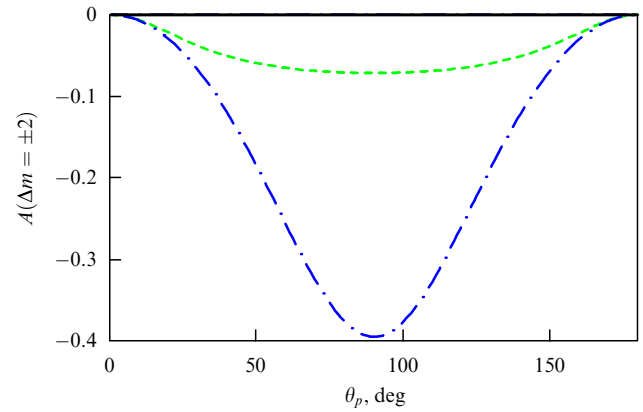

Figure 17. The same as in Fig. 16, but at $\Delta m = \pm 2$.

projection of the total angular momentum but with equal values of longitudinal momentum k_z, transverse momentum modulus $\varkappa$, energy $\omega = \sqrt{\varkappa^2 + k_z^2}$, and helicity Λ [see expression (84)]. In this case, the differential cross section possesses azimuthal asymmetry:

$$\frac{\mathrm{d}\bar{\sigma}}{\mathrm{d}\Omega_p} = \frac{\sigma^{\mathrm{pl}}}{\cos\theta_k}\, W_\Lambda^{\mathrm{tw}}(\theta_p)\left\{1 + A\cos\left[\Delta m\left(\varphi_p - \frac{\pi}{2}\right) + \Delta\alpha\right]\right\}, \tag{113}$$

where the function $W_\Lambda^{\mathrm{tw}}(\theta_p)$ is defined by expression (112) and the parameter of azimuthal asymmetry

$$A = -\frac{3|c_1 c_2|}{4\bigl(1 - P_2(\cos\theta_k)\, P_2(\cos\theta_p)\bigr)} \times \begin{cases} \sin(2\theta_k)\sin(2\theta_p) & \text{at} \quad \Delta m = \pm 1\,, \\ \sin^2\theta_k \sin^2\theta_p & \text{at} \quad \Delta m = \pm 2\,, \\ 0 & \text{for} \quad \Delta m \neq \pm 1, \pm 2\,. \end{cases} \tag{114}$$

The function $A(\theta_p)$ at $\Delta m = \pm 1$ and $\Delta m = \pm 2$ is plotted, respectively, in Figs 16 and 17 for the same opening angles as in Fig. 15 and at $|c_1 c_2| = 1/2$. One can see that the azimuthal asymmetry may be quite significant, ranging up to almost 50%.

Mesoscopic target. In this case, the normalized angular distribution may be obtained by considering expression (91)

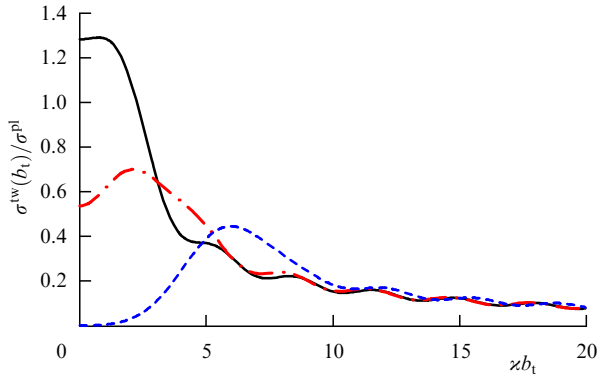

Figure 18. Ratio $\sigma^{\mathrm{tw}}(b_{\mathrm{t}})/\sigma^{\mathrm{pl}}$ from expression (117) plotted as a function of $\varkappa b_{\mathrm{t}}$ at $w = 1/\varkappa$, $\theta_p = 30°$, and $m = 0$ (solid curve), $m = 2$ (dashed–dotted curve), and $m = 5$ (dashed curve).

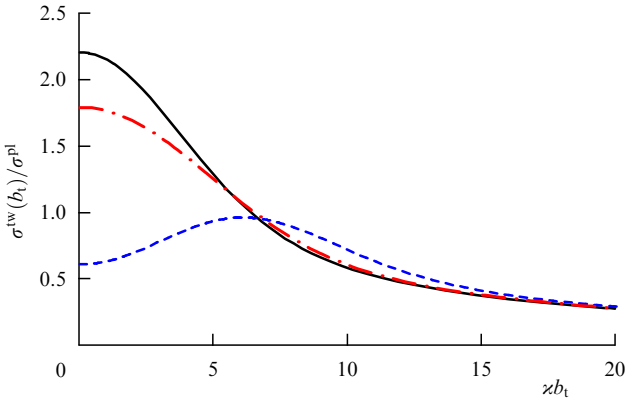

Figure 19. The same as in Fig. 18, but for a target with $w = 3/\varkappa$.

in the form

$$W^{\mathrm{tw}}(\theta_p, \varphi_p) = \mathcal{N}\Bigl\{\mathcal{B} + \mathcal{C}\sin(\varphi_p - \varphi_{b_{\mathrm{t}}}) + \mathcal{D}\cos\bigl[2(\varphi_p - \varphi_{b_{\mathrm{t}}})\bigr]\Bigr\}, \tag{115}$$

where coefficients $\mathcal{B}$, $\mathcal{C}$, and $\mathcal{D}$ depend on angles θ_k and θ_p in terms of functions B, C, and D defined by formulas (92):

$$[\mathcal{B}, \mathcal{C}, \mathcal{D}] = \int_0^\infty \left[BI_0\left(\frac{bb_{\mathrm{t}}}{w^2}\right),\ -CI_1\left(\frac{bb_{\mathrm{t}}}{w^2}\right),\ DI_2\left(\frac{bb_{\mathrm{t}}}{w^2}\right)\right] \times \exp\left(-\frac{b^2 + b_{\mathrm{t}}^2}{2w^2}\right)\frac{b\,\mathrm{d}b}{w^2}\,, \tag{116}$$

while the normalization constant $\mathcal{N}$ is defined by the condition $1/\mathcal{N} = \int \mathcal{B}\,\mathrm{d}\Omega_p$.

Lastly, we indicate that the total cross section averaged over the photon helicities is expressed as

$$\sigma^{\mathrm{tw}}(\varkappa, m, b_{\mathrm{t}}, w) = \frac{1}{2}\sum_\Lambda \int \frac{\mathrm{d}\sigma_\Lambda^{\mathrm{tw}}}{\mathrm{d}\Omega_p}\,\mathrm{d}\Omega_p = \frac{\omega\sigma^{\mathrm{pl}}}{4\pi\mathcal{J}_z} \times \int_0^\infty \Bigl\{2J_m^2(\varkappa b)\sin^2\theta_k + \bigl[J_{m-1}^2(\varkappa b) + J_{m+1}^2(\varkappa b)\bigr](1 + \cos^2\theta_k)\Bigr\} \times I_0\left(\frac{bb_{\mathrm{t}}}{w^2}\right)\exp\left(-\frac{b^2 + b_{\mathrm{t}}^2}{2w^2}\right)\frac{b\,\mathrm{d}b}{w^2}\,, \tag{117}$$

where $\mathcal{J}_z$ is the flux density integrated over ρ with consideration for the ion distribution in the target [see formula (69)]. Figures 18 and 19 demonstrate the ratio of the total cross

section of the process with a twisted photon to the standard cross section as a function of impact parameter b_t for the target center relative to the twisted beam axis for two targets of size $w = 1/\varkappa$ and $w = 3/\varkappa$. By comparing these curves with the twisted-photon density curves in Fig. 3 for the same values of quantum number m, we arrive at a natural result: the target of relatively small size turns out to be more sensitive to the density variations of the incident twisted photon than the target of a larger size.

3. Twisted photon beams in the terahertz range

3.1 General remarks

From the brief consideration in the Introduction (see Section 1.3), it follows that publications on twisted photons may be rather clearly divided into two groups. The first deals with investigations into the interaction of individual photons with atoms and uses the quantum-mechanical formalism to describe the processes occurring therein. The other, greater, group of publications pertains to twisted laser beams. In most cases they are described using the formalism of physical optics. Studied in the overwhelming majority of these papers are only beams in the visible range. Among the studies concerned with other spectral regions, mention can be made of review [45], which deals with twisted ultraviolet beams, and Ref. [47], which demonstrated twisted beams in the radio frequency band. The domains of mid- and far-infrared regions to date remain practically unexplored, and only eight experimental studies [81–88] describing twisted beams in the 0.3–3 THz range are known to us. Although from the viewpoint of electrodynamics the beam properties are the same in all ranges, the techniques for generating twisted beams and recording their characteristics in the terahertz range are largely different from those in the well-studied visible range. That is why a brief consideration of the few experimental studies of terahertz twisted beams will be useful, in our opinion.

However, several remarks are in order prior to turning to this survey. First, although the angular momentum cannot be separated into the spin and orbital angular momenta (SAM and OAM, respectively), with some reservations [89] in the paraxial approximation in optics they are considered independently [see expression (32) and its discussion in Section 2.1.1]. The quantum number for the orbital angular momentum, which was denoted by m_l in the previous sections, in optics is commonly referred to as the *topological charge* and denoted by ℓ. To match the text to the drawings borrowed from the papers cited below, in what follows we use ℓ as the synonym of m_l. Second, it is significant that some papers use the left-handed coordinate system, and therefore one has to be watchful when reading the literature (see Ref. [91]). Following the majority of publications, we use the right-handed coordinate system, in which the azimuthal angle increases in the clockwise direction when looking along the axis of beam propagation (Fig. 20). The wave front equation may be derived from expression (9). At a constant phase $\Phi_* = 0$, the wave front equation takes on the form

$$z = -\frac{\ell\varphi}{k_z}\,, \tag{118}$$

and the phase distribution over the beam cross section is

$$\Phi(\varphi) = \ell\varphi\,. \tag{119}$$

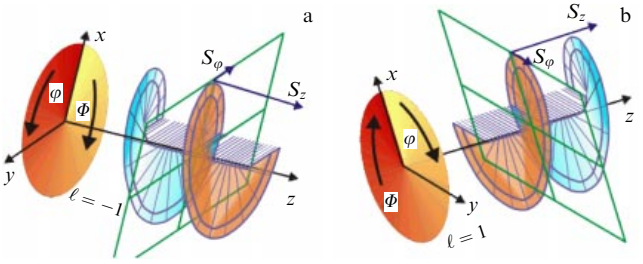

Figure 20. Wave fronts of twisted beams with topological charges $\ell = -1$ (a) and $\ell = 1$ (b). The phase distributions over the beam cross section are shown in the xy section. The arrows denote the components S_φ and S_z of the Poynting vector.

It can be seen in Fig. 20 that a right helicoid corresponds to a negative topological charge in the selected coordinate system, while a left one corresponds to a positive topological charge.

3.2 Production of twisted beams with broadband radiation sources

In each of the experiments mentioned above, use was made of its own technique for twisted beam generation. As is well known, the most common sources of terahertz radiation are wideband oscillators which are based on the employment of femtosecond lasers, so-called time domain spectrometers (TDSs) [92]. In these devices, the spectral characteristics of an object are reconstructed by the inverse Fourier transform of the temporal dependence of the electric field amplitude of the terahertz wave transmitted through the object. To record this dependence, this signal must be scanned in time in an electrooptical crystal by a probe beam using an optical delay line (Fig. 21). Therefore, such measurements call for a significant period of time and real-time measurements are impossible. Such sources were employed to produce twisted beams in Refs [81, 82, 84].

One version of the optical spectrometer configuration with time resolution is depicted in Fig. 21a [82]. Such systems are bound to have a femtosecond pump beam, which generates (in this case, by the method of optical rectification in a nonlinear ZnTe crystal) a short pulse of broadband terahertz radiation and a probing beam split off from the pump beam, which is delayed in an optical delay line and is used to visualize the terahertz radiation. In the configuration depicted, the radiation is reflected from the left boundary of the detecting nonlinear ZnTe crystal, in which it interacts with the terahertz radiation, and carries information about its properties to the recording system [93], which consists of two lenses, a quarter-wave plate, and a Wollaston prism. To transform the terahertz radiation into a Laguerre–Gaussian beam with an orbital angular momentum, in the above configuration use was made of a third ('control') beam. It passed through a liquid-crystal spatial modulator of visible radiation, which served as an amplitude transparency in the form of a fork diffraction grating programmed for controlling the terahertz radiation (Fig. 21b). The control beam transmitted through the transparency was projected with a lens onto a high-resistance silicon plate, on which a copy of the transparency was formed due to the photo-induced generation of charge carriers. The terahertz beam incident on the plate was diffracted by the grating and transformed for a given frequency into a twisted beam propagating towards the recording system. By varying the grating

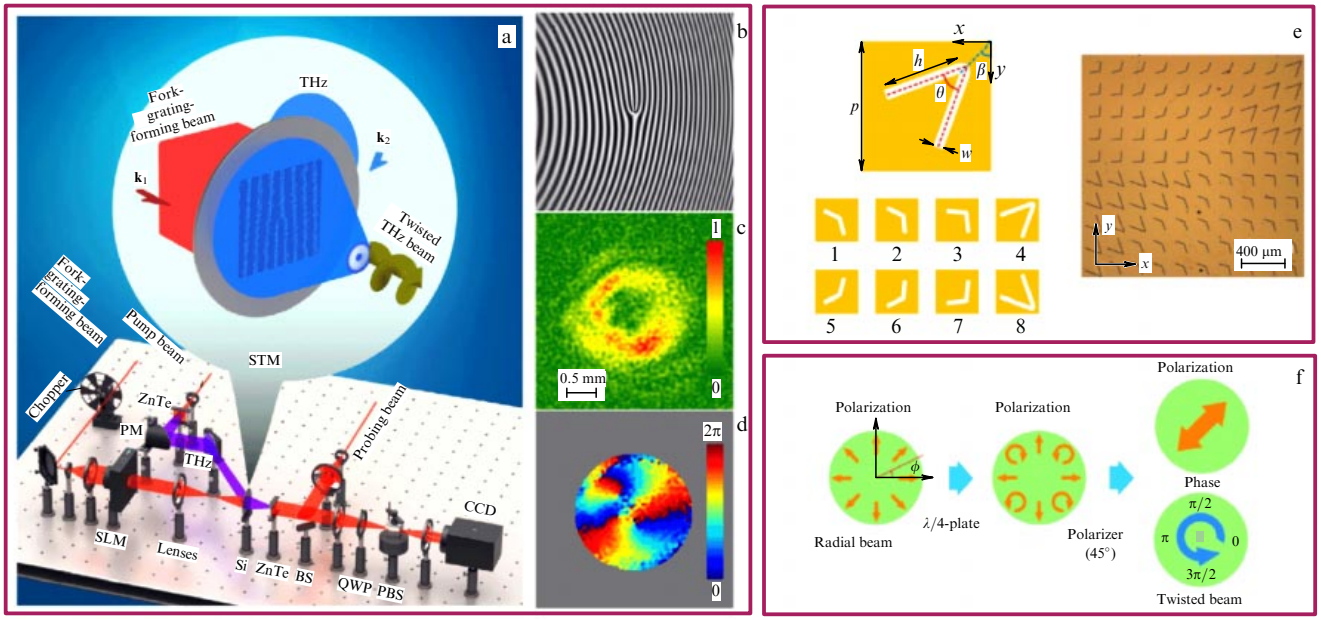

Figure 21. Formation of twisted beams with the use of broadband terahertz radiation sources. (a) Optical system with a spatial modulator of terahertz radiation based on a high-resistance silicon plate, on which a fork diffraction grating is formed using a spatial light modulator in the visible range [82]. STM — spatial terahertz radiation modulator, $\mathbf{k}_1$ and $\mathbf{k}_2$ — wave vectors of the shaping and terahertz beams, ZnTe — ZnTe crystal, PM — parabolic mirror, SLM — spatial light modulator, Si — high-resistance silicon plate, BS — beam splitter, QWP — quarter-wave plate, PBS — polarizing beam splitter, CCD — charge coupled device (CCD camera). (b) Third-order fork grating and (c) amplitude and (d) phase distributions of its formed twisted beam with $\ell = 3$. (e) Transmission phase plate made up of eight modules of V-shaped antenna slots with different opening angles. The azimuthal phase incursion in the radiation transmitted through the plate is equal to 2π, $\ell = 1$ [81]. (f) Transformation of a radially polarized vector beam into a broadband twisted beam with $\ell = -1$ using a quarter-wave plate and a polarizer [84].

parameters, it was possible to produce in this system beams with a topological charge up to 3. A virtue of systems with spatial radiation modulators is the capacity to rapidly change the transmission function of transparencies and to produce beams with almost arbitrary amplitude–phase distribution.

In Ref. [81], a thin metallic film with V-shaped slot antennas (Fig. 21b) was used to produce a twisted beam. By combining into an array of eight modules with different antenna opening angles, which provided wave phase shifts at increments of $\pi/4$, the authors of Ref. [81] obtained a twisted beam for a frequency of 0.75 THz at the output. The principle of operation of this antenna system is comprehensively described in Ref. [94]. This structure is a crude analogue to a first-order spiral phase plate — the simplest device for obtaining beams with an OAM. An analysis of correlation coefficients showed that $\ell = 1$ was the main OAM mode, with a small admixture of -1, -2, and ± 3 modes. The authors observed a phase discontinuity at the lens focus in accordance with the Gouy effect. The modes $\ell = 2$ and $\ell = 3$ were also obtained using this kind of antenna structure. Unlike the optical scheme with a holographic grating, this one does not separate the twisted beam at a prescribed frequency from the radiation of other frequencies transmitted through the grating, and the low mask transmittance significantly restricts the intensity. The possibility of obtaining a twisted beam simultaneously for a broad frequency spectrum is provided by the purely optical transformation scheme depicted in Fig. 21f, which transforms a radially polarized beam into a twisted beam with the aid of a quarter-wave plate and a polarizer [84]. The authors produced and investigated the $\ell = 1$ beam in a frequency range from 0.75 to 2 THz.

3.3 Production of twisted beams with monochromatic sources

In recent years, monochromatic terahertz radiation sources have become increasingly widespread. By way of example, mention can be made of rapidly developing quantum-cascade lasers (see, for instance, Refs [95–97]), which can be produced for any frequency of interest, from the infrared to the terahertz ranges. For research purposes and technique development, it is convenient to take advantage of free electron lasers [98–100], which may smoothly tune the frequency over a wide range and offer a high output power. Such sources permit the formation and rapid transformation of beams of the desired mode composition, real-time image recording, and the study of dynamic processes.

Figure 22a is a layout of the optical configuration [83] intended for twisted beam generation using a spiral plate of Tsurupica polymer material with a refractive index $n = 1.52$ and absorptivity varying from 0.4 to 0.94 cm^{-1} in the 2–6 THz frequency range. The plate's spiral ramp height is equal to 290 μm, which corresponds to a one-turn phase incursion of 2π for a radiation frequency of 2 THz, and to 4π for a frequency of 4 THz. Plate irradiation by a Gaussian beam must give rise to a Laguerre–Gaussian (LG) beam of $\text{LG}_{0.1}$ or $\text{LG}_{0.2}$ modes, respectively. A virtue of the spiral plate is its high transmittance. However, its output beam contains higher-order Laguerre–Gaussian modes due to wavelength departure from the design one or due to plate fabrication defects. The narrowband terahertz radiation with a picosecond pulse duration is generated in the crystal of DAST organic salt at the difference frequency of two optical parametric amplifiers pumped by a laser at a wavelength of 1064 nm. The seed radiation is provided by two diode lasers with wavelengths of about 1.5 μm. The authors of Ref. [83]

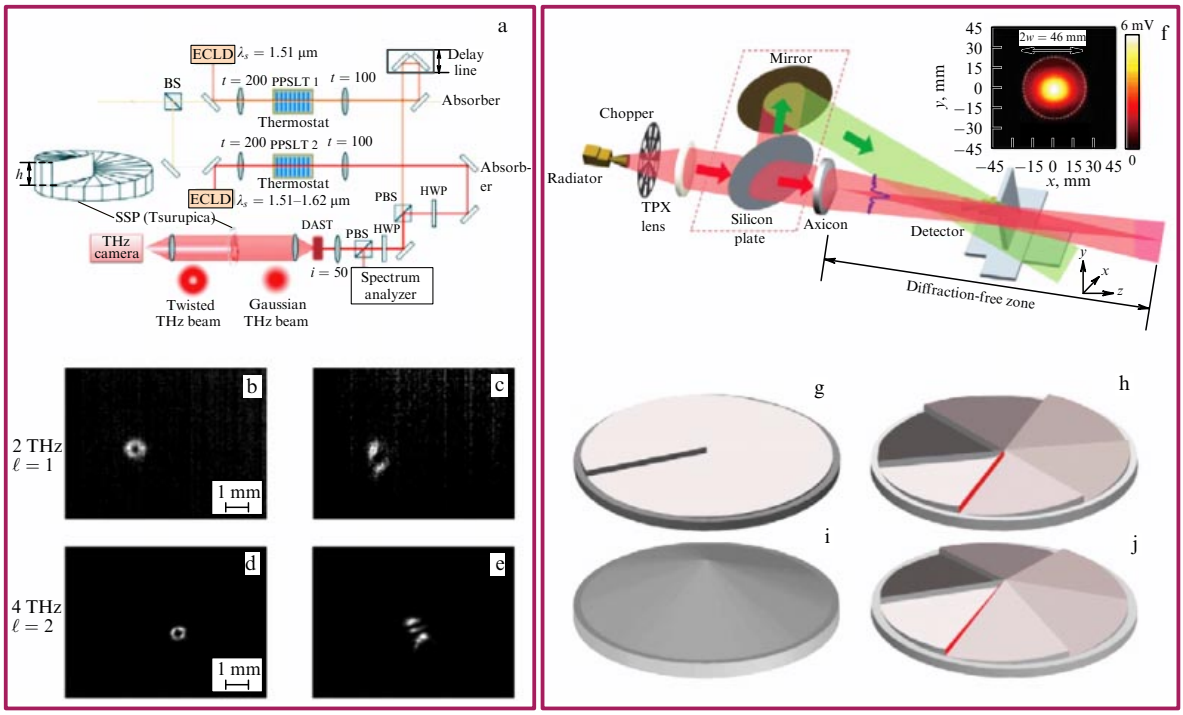

Figure 22. Production of twisted beams with the use of monochromatic terahertz radiation sources. (a) Optical system of two parametric amplifiers and a difference frequency generator for forming Laguerre–Gaussian beams with the help of a spiral phase plate [83]. For a radiation source, use is made of an Nd:YVO_4 laser with a wavelength of 1064 nm, a pulse repetition rate of 1 MHz, a pulse length of 7.4 ps, and an output power of 14 W. Notation: ECLD — external-cavity laser diode, PPSLT — periodically poled stoichiometric lithium tantalate, HWP — half-wave plate, PBS — polarizing beam splitter, DAST — (diethylamino) sulfur trifluoride, SPP (Tsurupica) — spiral phase plate based on the Tsurupica olefin polymer (picarin). Images of beams (b, c) with $\ell = 1$ (frequency: 2 THz) and (d, e) $\ell = 2$ (frequency: 4 THz) using a terahertz camera for normal (b, d) and inclined (c, e) positions of the output lens. (f) Optical system for the formation of Bessel beams [85]. A first-order Bessel beam was obtained using the combination of a spiral phase plate (g) and an axicon (i). To obtain sixth-order beams, use was made of a kinoform spiral plate (h) and the kinoform version of a helicoidal axicon (j). The inset (top right) to Fig. 22f depicts the cross section of the Gaussian beam with the mode radius w, incident on the axicon.

estimated the conversion efficiency of this system at 10^{-6}. Using a system of two lenses and a terahertz camera, it was nevertheless possible to record the LG beams shown in Figs 22b and 22d. Inclining the output lens transformed the beams to Hermit-Gaussian (HG) ones, and it was possible to determine the magnitude of topological charge from the number of fringes (Figs 22c and 22e).

While all previous papers were concerned with obtaining Laguerre–Gaussian beams, Bessel beams were formed in Refs [85, 86]. To this end, in Ref. [86] use was made of a binary phase axicon with spiral zones (we will enlarge on these experiments in Section 3.4). To generate Bessel and Laguerre–Gaussian beams in Ref. [85], use was made of different combinations of the spiral plate described above and an axicon, which were arranged sequentially or integrated into a single element (Figs 22f–22j). All elements were 3D printed using plastic transparent to far terahertz radiation. The elements intended for the formation of high-order beams were fabricated in a kinoform version to reduce their longitudinal dimensions: the phase shift in each zone lay in the range between 0 and 2π. In Ref. [85], the elements were designed for a radiation frequency of 0.3 THz generated by a Gunn diode with a frequency multiplier. Using a single-channel scanning detector, the authors showed that Bessel beams had a smaller cross section and a lower divergence than Laguerre–Gaussian beams. When comparing volume and kinoform ('planar') elements, it is worth bearing in mind that a virtue of the volume elements is the possibility of successfully forming a beam of arbitrary wavelength, while more compact kinoform elements have the capacity to work efficiently in only a rather narrow wavelength range (see, for instance, Refs [101, 102]).

3.4 Experiments on the Novosibirsk free electron laser

3.4.1 Brief history of Bessel beams. Since Bessel beams were obtained in experiments to produce beams with an orbital angular momentum on the Novosibirsk free electron laser (NFEL), we begin with their brief history. An ideal Bessel beam is of infinite cross section, and therefore such beams do not exist in reality, and any real beam of a limited cross section may be classified as a Bessel-like one, whose properties persist only through a limited distance. However, even in this case the beam characteristics may exhibit features dependent on the method of its production. With this reservation, such beams are hereinafter referred to as 'Bessel'.

In 1987, Durnin [103] investigated the solution of the scalar wave equation for the fundamental Bessel beam mode $J_0(\varkappa r)$. The main properties of this beam are the invariability of its cross section in its propagation in space ('diffraction-free' propagation) and the self-recovery of its cross section after passage through an obstacle. These properties are easily explained when it is considered that a Bessel wave may be represented as a set of plane waves which conically converge to the optical axis [104]. Hence, it is evident that the Fourier image of a Bessel beam (the image of the beam in the focal plane of a lens) is a ring [see expression (12)]. Durnin et al. [105] showed by numerical simulations and bore out experi-

mentally that pseudo-diffraction-free beams, whose intensity in a transverse plane remains invariable in its propagation in free space, may be formed in the finite aperture case as well. Lin et al. [106] employed interferometry to find that the zero-order Bessel beams formed using a ring mask have a plane wave front with π phase shifts between adjacent rings. A drawback of the beams produced with an axicon or a ring mask is the oscillation of intensity along the optical axis. Jiang et al. [107] showed that these oscillations may be diminished by using amplitude and phase apodization of the incident beam. Useful information about Bessel beams and their application can be found, for instance, in Refs [108–113].

In the terahertz range, zero-order Bessel beams were first obtained in Refs [114–116] using an axicon, which was proposed back in 1954 [117]. In Refs [114, 116], broadband zero-order Bessel beams were formed using the time-domain spectroscopy technique, with a spatial resolution of 2 mm at a frequency of 0.5 THz achieved at a distance of over 120 mm [116]. A cw terahertz radiation source was utilized in Ref. [115] and a resolution of better than 4 mm at a distance of 100 mm was achieved at a radiation frequency $f = 0.2$ THz. The 'diffraction-free' character and the capacity for self-recovery of Bessel beams may be employed in the terahertz range in optical traps for the nondestructive inspection and visualization of objects partially transparent in the terahertz range.

3.4.2 Binary phase axicons for forming twisted Bessel beams. The most commonly used way of forming twisted Bessel beams is the transformation of a plane wave with the combination of an axicon and a spiral phase plate. One version of this scheme is shown in Fig. 22f. We employed another method of Gauss-to-Bessel beam transformation, which involved the use of binary phase axicons (BPAs) with a spiral configuration of zones (Figs 23a–23c). The zone boundaries are described by the equation $r_\beta = p(\ell\varphi/(2\pi) + \beta/2)$, where $\beta = 0, \ldots, 2\ell - 1$, and p is the period. The relief depth H, which was calculated for the wavelength $\lambda_0 = 141$ μm, viz.

$$H = \frac{\lambda_0}{2(n-1)} = 29.1\ \mu\text{m}\ \ (n = 3.42)\,, \tag{120}$$

corresponded to a phase increment of 2π between the steps. The method of axicon fabrication and testing was described in Ref. [118].The phase spiral axicons of the same configuration were used by Andreev et al. [119] for the formation of first- and fifth-order twisted Bessel beams at a wavelength of 1.06 μm. By way of numerical experiment, Degtyarev et al. [120] showed the possibility of obtaining a photon microspiral in the near-field zone of the laser beam diffraction by such an axicon.

We consider after Choporova et al. [87] the propagation of a plane wave through a spiral axicon described by the following phase function:

$$h(r, \varphi) = F(\ell\varphi - \varkappa r)\,, \tag{121}$$

where $\varkappa$ is the radial wave number. In the binary axicon case, $F(\ell\varphi - \varkappa r)$ is a meander:

$$F(\ell\varphi - \varkappa r) = \begin{cases} -\dfrac{\pi}{2} & \text{for}\ \ 2s\pi \leqslant \ell\varphi - \varkappa r < (2s+1)\pi\,, \\ \dfrac{\pi}{2} & \text{for}\ \ (2s+1)\pi \leqslant \ell\varphi - \varkappa r < 2(s+1)\pi\,, \end{cases} \qquad s = 0, \ldots, \ell - 1\,. \tag{122}$$

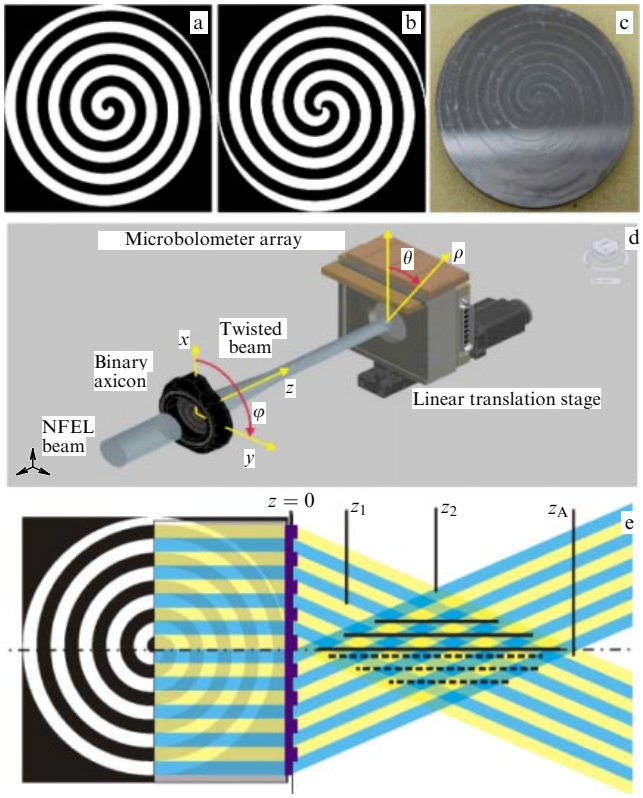

Figure 23. Zone structures of binary spiral phase axicons made of high-resistance silicon, which form beams with topological charges $\ell = 1$ (a) and $\ell = 2$ (b, c). The axicon diameters are equal to 30 mm, and the radial period is equal to 3.1 mm. To obtain beams with a negative topological charge, the axicons should be rotated by 180° about the vertical axis. (d) Layout of the experiment and coordinate system. (e) Schematic of plane wave diffraction by the binary axicon in the formation of a Bessel beam with $|\ell| = 1$. For clarity, only the converging waves of −1st order are shown.

Using the Rayleigh–Sommerfeld integral, we can write out the electric field amplitude in the plane with coordinates $\{z, \rho, \theta\}$ (Fig. 23d) in the paraxial approximation:

$$E(z, \rho, \theta) = -\frac{\mathrm{i}k}{2\pi z} \exp\left[\mathrm{i}k\left(z + \frac{\rho^2}{2z}\right)\right] \int_0^a S_1 \exp\left(\frac{k}{2z}\, r^2\right) r\, \mathrm{d}r\,, \tag{123}$$

where

$$S_1 = \int_0^{2\pi} \exp\left[\mathrm{i}h(r, \varphi) - \mathrm{i}\,\frac{k}{z}\, r\rho\cos(\varphi - \theta)\right] \mathrm{d}\varphi\,. \tag{124}$$

For the phase function described by Eqn (122), the factor S_1 assumes the form

$$S_1 = \sum_{s=0}^{2\ell-1} (-1)^{s+1} \int_{s\pi/\ell}^{(s+1)\pi/\ell} \exp\left[-\mathrm{i}\,\frac{k}{z}\, r\rho\cos\left(\varphi' + \frac{\varkappa r}{\ell} - \theta\right)\right] \mathrm{d}\varphi'\,, \tag{125}$$

where $\varphi' = \varphi - \varkappa r/\ell$.

The Fourier expansion of expression (125) contains only odd harmonics ($n = 2q + 1$) with amplitudes proportional to $J_{\ell(2q+1)}(kr\rho/z)/(2n+1)$. When the higher-order harmonics corresponding to the higher orders of diffraction by our grating are disregarded, expression (125) takes on the form

$$S_1 = 8(-\mathrm{i})^{\ell-1} J_\ell\left(\frac{k}{z}\, r\rho\right) \sin(\varkappa r - \ell\theta)\,. \tag{126}$$

The field behind the axicon can now be written out in the following way:

$$E(z,\rho,\theta) \approx \frac{4k}{\pi z}(-\mathrm{i})^{\ell}\exp\left[\mathrm{i}k\left(z+\frac{\rho^2}{2z}\right)\right] \times \int_0^a J_\ell\left(\frac{k}{z}r\rho\right)\sin(\varkappa r-\ell\theta)\exp\left(\mathrm{i}\,\frac{k}{2z}\,r^2\right)r\,\mathrm{d}r\,. \quad (127)$$

Since the radiation near the optical axis is formed by the waves which conically converge at an angle $\arcsin(\varkappa/k)\approx\varkappa/k$, the space behind the binary axicon of radius a may be divided into two zones (Fig. 23e). At distances shorter than $z_\mathrm{A}=ka/\varkappa$, inside the circular cone $\rho<a(1-z/z_\mathrm{A})$, the wave field to a first approximation (when the small divergence due to diffraction by the aperture is ignored) is independent of the axicon radius and forms a tubular beam near the axis. In Fig. 23e, the domain of constructive interference of converging waves is shown with solid horizontal lines, while that of destructive interference with dashed lines. It is clear that the Bessel beam forms at some distance from the axicon and begins to decay when approaching z_A. At long distances in the far-field zone, the beam becomes annular. According to the theory, the diffraction efficiency of Bessel beam formation is equal to 42%.

The integral in expression (127) may be evaluated using the high-frequency ($k\gg\varkappa\gg 1/a$) paraxial ($z\gg a,\rho$) approximation [121, 122]. Upon transformations, we obtain three spatial domains presented in Table 1, for which the following expressions for the wave electric field are legitimate:

$$E(z,\rho,\theta) \approx \begin{cases} \dfrac{2\varkappa}{\pi}(-\mathrm{i})^{\ell-1}\sqrt{\dfrac{2\pi\mathrm{i}z}{k}}\exp\left[\mathrm{i}\ell\theta+\mathrm{i}k\left(z+\dfrac{\rho^2}{2z}\right)-\mathrm{i}\,\dfrac{\varkappa^2}{2k}\,z\right]J_\ell(\varkappa\rho)\,, & (128a)\\ -\dfrac{4}{\pi}(-\mathrm{i})^{\ell}\exp\left[\mathrm{i}k\left(z+\dfrac{\rho^2}{2z}\right)\right]J_\ell\left(\dfrac{k}{z}a\rho\right)\exp\left(\mathrm{i}\,\dfrac{k}{2z}\,a^2\right) \times\dfrac{ka}{\varkappa z}\cos(\varkappa a-\ell\theta)\,, & (128b)\\ -\dfrac{2}{\pi z}(-\mathrm{i})^{\ell}\exp\left[\mathrm{i}kz\left(1+\dfrac{\rho^2}{2z^2}\right)\right]\sqrt{\dfrac{2ka^3z}{\pi\rho}}\,S_2\,, & (128c)\end{cases}$$

where

$$S_2=\int_0^1\sin\left[\left(\frac{\rho}{z}-\frac{\varkappa}{k}\right)kax+\ell\left(\theta-\frac{\pi}{2}\right)-\frac{\pi}{4}\right] \times\exp\left(\frac{\mathrm{i}x^2ka^2}{2z}\right)\sqrt{x}\,\mathrm{d}x\,.$$

Hence, we obtain expressions for the beam intensity distribution:

$$I(z,\rho,\theta)\propto\begin{cases} J_\ell^2(\varkappa\rho)\,\dfrac{8\varkappa^2z}{\pi k}\,, & (129a)\\ J_\ell^2\left(\dfrac{k}{z}a\rho\right)\left(\dfrac{4ka}{\pi\varkappa z}\right)^2\cos^2(\varkappa a-\ell\theta)\,, & (129b)\\ \dfrac{8ka^3}{\pi^3z^2}\,\dfrac{z}{\rho}\,|S_2|^2\,. & (129c)\end{cases}$$

The range of interest to us is the domain $a\ll z<z_\mathrm{A}$, where the beam is Besselian. From expression (129a) it follows that the diameters of beam rings are constant along the optical axis. They are independent of the wavelength and increase with the topological charge, provided the axicon period $p=2\pi/\varkappa$ persists. If the axicon is illuminated by a plane wave, the beam intensity in this domain will increase proportionally to the distance. Using tabular data for the maxima and minima of the Bessel function and substituting the axicon parameters, we obtain the expected beam radii given in the second row of Table 2.

Table 1. Applicability domains of expressions (128) and (129).

$a\ll z<z_\mathrm{A}$	$\rho\sim z/(ka)$	(128a), (129a)
$z\gg z_\mathrm{A}$	$\rho\sim z/(ka)$	(128b), (129b)
$z\gg z_\mathrm{A}$	$\rho\gg z/(ka)$	(128c), (129c)

Table 2. Calculated and measured parameters of first- and second-order Bessel beams.*

Parameter	$I_1^{\max}$	$I_1^{\min}$	$I_2^{\max}$	$I_2^{\min}$
$\varkappa\rho$	1.84	3.83	3.05	5.14
ρ^{calc}, mm	0.9	1.9	1.5	2.6
ρ^{exp}, mm	0.9	1.9	1.5	2.7
$\Delta z_{\mathrm{nondifr}}$, mm	200		150	
$\Delta z_{\mathrm{PitchCalc}}$, mm	246		340	
$\Delta z_{\mathrm{PitchSim}}$, mm	225 ± 13		327 ± 42	

* ρ^{calc} and ρ^{exp} are the calculated and measured values of the radius of the first ring, $\Delta z_{\mathrm{nondifr}}$ is the diffraction-free propagation distance, $\Delta z_{\mathrm{PitchCalc}}$ and $\Delta z_{\mathrm{PitchSim}}$ are the pitch of the complete revolution of the Poynting vector for the peak of first Bessel ring calculated by formula (134) and obtained by numerical simulations, respectively.

3.4.3 Formation of twisted Bessel beams at the Novosibirsk FEL. Twisted beams with an orbital angular momentum were obtained at the NFEL facility [100], which now is the highest-power source of terahertz radiation. Radiation with a line width $\Delta\lambda/\lambda=0.003-0.010$ is a continuous sequence of pulses with a duration on the order of 100 ps, which are emitted at a repetition rate of 5.6 MHz. The average output power at the workstation has ranged up to 100 W in experiments. The experiments were performed at a wavelength of 141 μm, at which the phase step between the axicon zones was equal to π. The NFEL radiation was linearly polarized, with wire or photolithographic polarizers employed to control its intensity.

The axicon was illuminated by a beam of Gaussian intensity distribution $I=I_0\exp(-2r^2/w^2)$, where $w\simeq$ 17 mm, and a nearly plane wave front. The transmitted wave intensity distribution behind the axicon (Fig. 23d) was measured with a microbolometer array (MBA) [123–126] with 320 by 240 sensitive elements 50 μm in size for a matrix size of 16.32 by 12.24 mm. Since the wavelength exceeded the pixel size, the detector resolution was wavelength-limited. The detector has been mounted on a linear translation stage. The intensity distribution over the beam cross section was recorded by moving the MBA along the optical axis in the form of a 'terahertz' video film. The measured longitudinal and transverse intensity distributions are shown in Fig. 24.

As is clear from Fig. 24, beams with intensity distributions very close to the distributions expected for Bessel beams are formed with the use of spiral axicons. The measurement data agree nicely with the numerical simulations performed in the framework of the scalar diffraction theory. The special features of numerical diffraction calculations in the case of measurements by detectors with smaller-than-wavelength

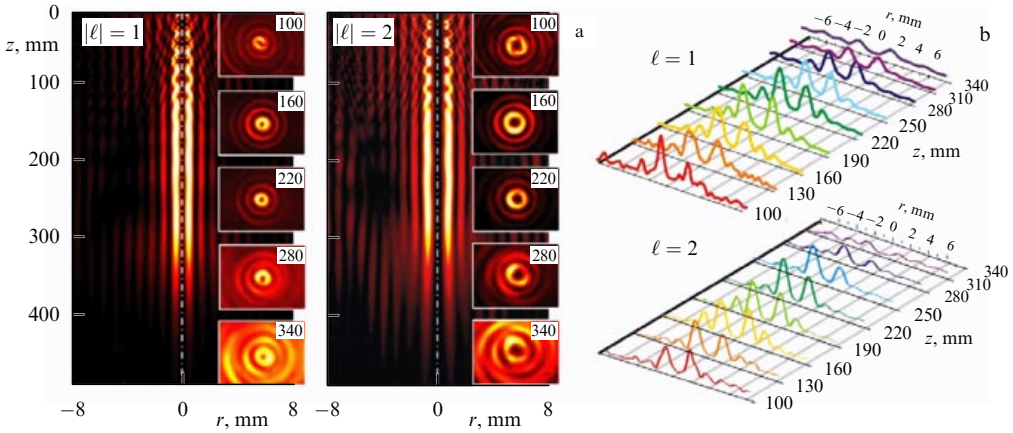

Figure 24. (Color online.) (a) Intensity distributions $I(r, z)$ along the optical axis, obtained by numerical simulations. The insets show the frames of the cross sections of twisted beams recorded by a microbolometer array. The frames measure 16.32×12.24 mm^2. The numbers in the frames show the distance from the axicon in millimeters. (b) Experimental intensity distributions over the beam cross sections [127].

sensitive elements are described in Ref. [128]. In all cases when we could compare the data of numerical simulations with experimental data, they were in excellent agreement (the only exception is discussed below), which made it possible to investigate the wave field in domains inaccessible due to geometrical restrictions.

Figure 25a plots the intensity distributions in beams with various topological charges and with imposed on them phase distribution, which corresponds in magnitude to the color scale given at the top of the drawing. One can see that the beams are completely formed at a distance $z \approx 130$ mm and their cross sections remain invariable at distances of up to $z \approx 300-350$ mm. These figures are consistent with the distance $z_A = 360$ mm, at which the intersecting plane waves diverge. Therefore, the resultant beams may be treated as nondivergent through a length $\Delta z_{\text{nondifr}} \approx 200$ and 150 mm for $|\ell| = 1$ and $|\ell| = 2$, respectively, which is borne out by the experimental distributions shown in Fig. 24b. The diameters of experimentally observed maxima and minima of the beam rings given in Table 2 agree well with the calculated values.

3.4.4 Features of Bessel beams formed by binary axicons. As mentioned above, the characteristics of Bessel beams produced in a laboratory must, to one degree or another, bear the traces of their origin. This is clearly demonstrated by experiments on the investigation of the beam Fourier spectrum and the evolution of the phase distribution of a beam propagating along the z-axis, which was produced by a binary phase axicon. Figure 25b shows the intensity distributions recorded by the matrix detector at the focus of a lens mounted at a distance of 160 mm from the axicon. Instead of a solid ring corresponding to the Fourier spectrum of an ideal Bessel beam, we observe a ring divided into spiral segments, whose number is equal to twice the magnitude of the topological charge 2ℓ. Numerical simulation data, which are presented in Fig. 25c, suggest that the phases of adjacent spirals in the Fourier spectrum differ by π. Inside the main ring, we observe a system of nested, less intense spirals. As would be expected, the far-field intensity distribution of the beam itself is the same as in the Fourier plane. This is borne out by the form of the far-field radiation intensity distribution calculated with the use of expression (129c) and plotted in the red square (FF) in Fig. 25b.

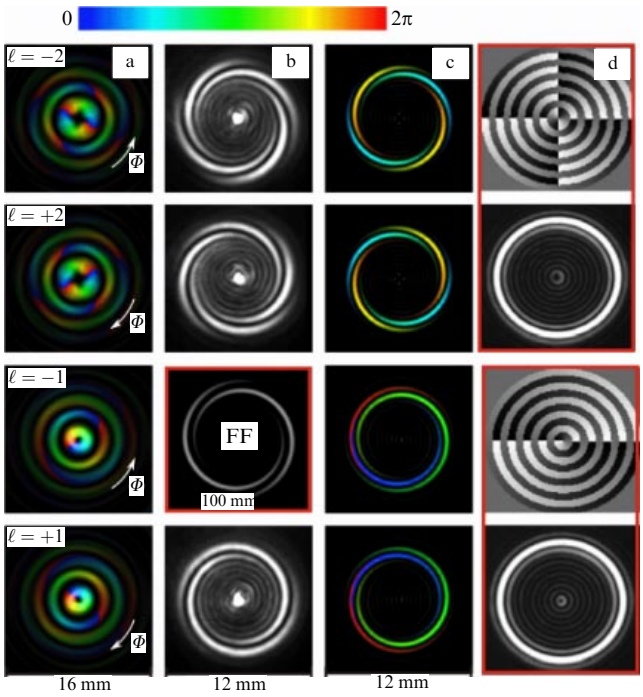

Figure 25. (Color online.) (a) Calculated distributions of intensity and phase (2π in modulus) in beams formed by spiral binary phase axicons at a distance $z = 160$ mm; the arrows indicate the direction of increasing phase Φ. Spatial Fourier spectra of these beams in the focal plane of a lens with $f = 100$ mm obtained experimentally (b) and calculated numerically (c). The far-field beam intensity distribution calculated analytically at a distance $z = 1000$ mm for $\ell = -1$ with the use of Eqn (129c) is shown in the red square (FF). The frame size is shown in the lower part of the drawing. (d) Multilevel phase axicons (first and third frames from top) and Fourier spectra of their formed Besselian beams of the first (fourth frame from top) and second (second frame from top) order recorded in experiments at a wavelength of 632 nm [129].

We will now explain the origin of the bright central spot in the focal plane of the lens. This effect, which has repeatedly been noted in the literature, is due to Fresnel reflections inside the binary phase plate. Since the reflection coefficient of silicon is quite high, it would be sufficient to take into account the radiation reflected once from the front and rear facets and outgone after the twisted beam. Its intensity

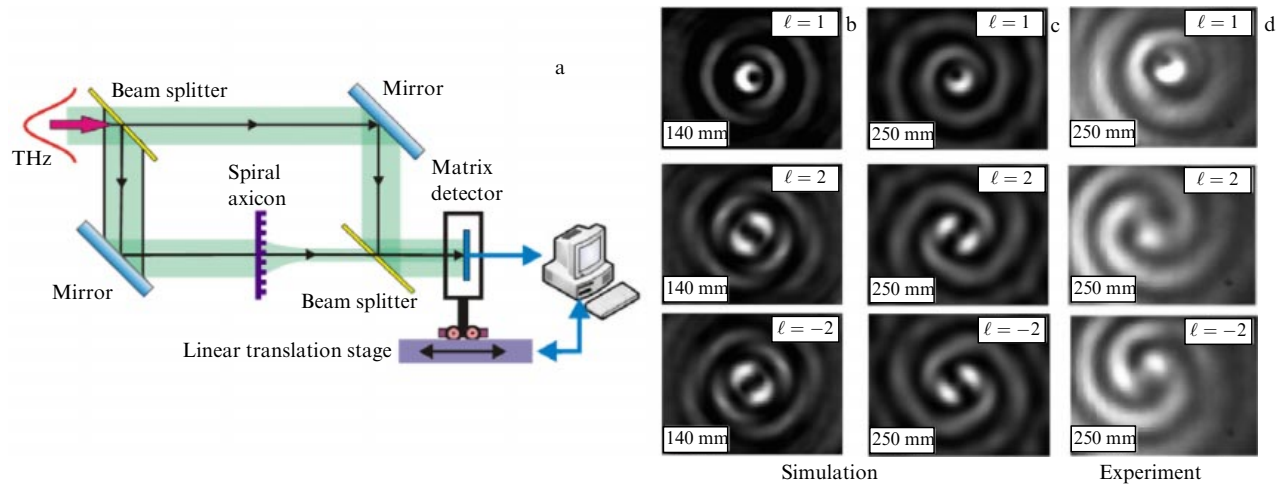

Figure 26. (a) Schematic of the experiment to investigate the phase of a quasi-Bessel beam with the aid of a Mach–Zender interferometer. Interference between a twisted beam and a Gaussian beam possessing a plane wave front at distances of 140 and 250 mm from the axicon; (b, c) numerical simulation data, and (d) experimental data.

$|E_{\text{plane}}|^2/|E_{\text{diff}}|^2 = [(n-1)/(n+1)]^4$ amounts to about 10% of the twisted beam intensity. For a path difference between the steps equal to π, the difference between optical wavelengths outgone through different levels [see formula (120)] is expressed as

$$\Delta L_{12} = H(3n-1)\,. \tag{130}$$

In our case, the phase difference $\Delta\Phi_{12} = 3.84\pi \approx 4\pi$. These secondary waves interfere constructively to form a zero-order plane wave with an efficiency of 93.7%. The remaining fraction of the secondary wave diffracts to the first order. For an arbitrary wavelength, the phase difference of these waves in our axicons takes on the form

$$\Delta\Phi = \frac{\lambda_0\pi(3n-1)}{\lambda(n-1)}\,. \tag{131}$$

We note that the refractive index of silicon is practically constant in the terahertz range. It is possible to get rid of Fresnel reflection in this frequency range by depositing an antireflection coating onto the silicon surface. In the terahertz range, a parelene layer may be used for this purpose [130].

It would be interesting to compare the Fourier spectra presented here with the Fourier spectra of the first- and second-order Bessel (quasi-Bessel) beams recorded in the focal plane of the lens, which were obtained in Ref. [129] with the aid of a multilevel phase axicon. Its phase distribution is shown in Fig. 25d. In Ref. [129], the phase axicon (a computerized hologram) was formed with a spatial light modulator for a wavelength of 632 nm. The solid ring is formed due to a smooth phase increase in the azimuth, while the inner rings, like ours, are formed due to the stepwise phase function in the radial direction and the finite aperture of the hologram (for details, see Ref. [129]). A comparison of the images in Figs 25b and 25d suggests that the form of ring discontinuities in the spiral axicon case is related to the fact that its phase function along the azimuthal angle is a piecewise constant function $\Phi(\varphi) = (\pi/2)\,\text{sgn}\,[\sin(l\varphi)]$, whose zeroes describe one complete revolution with increasing radius by a value equal to the axicon period: $\Delta r = p$. From the Fourier spectrum of the beam formed by the spiral phase axicon, it follows that the system of beam-forming plane waves converges not on the optical axis but on a ring surrounding the optical axis. An obvious way to achieve an annular Fourier spectrum is to use a kinoform spiral axicon.

One more difference between our resultant beam and the ideal Bessel one may be revealed in Ref. [131] by studying the phase in the cross sections at different distances from the axicon with the aid of a Mach–Zender interferometer (Fig. 26a). The phase distribution was visualized with a microbolometer array in the interference of a Gaussian beam with a plane wave front with the twisted beam formed by the axicon [131]. Because of geometrical restrictions, there was no way of recording the interference pattern at close distances, and so we first compare the interference patterns obtained by numerical simulations (Figs 26b and 26c). One can see that the interference pattern at a distance $z = 140$ mm from the axicon corresponds precisely to the interference pattern whereby both beams have a plane wave front (Fig. 26b). At a distance $z = 250$ mm, however, when the beam is still well formed (see Fig. 24), the interference patterns, both calculated (Fig. 26c) and experimentally recorded (Fig. 26d), testify that the wave front of one of the beams acquires a spherical shape. Since the Gaussian wave hardly changes through this distance, it is safe to say that the twisted beam acquires divergence.

3.4.5 Self-recovery of a Bessel beam. Since, as is clear from Section 3.4.4, twisted beams obtained with the help of spiral axicons are similar but are somewhat different from Bessel ones, there is good reason to determine whether the main properties of Bessel beams are retained. One of the most important properties of a Bessel beam, which is exploited in many applications, is the capacity to recover its spatial distribution after passage through an obstacle. Experiments in Ref. [132] suggest that the beam recovers after passing through both amplitude and phase obstacles.

Figure 27 depicts the cross sections of the beam incident on a phase scatterer, and of the beams at distances of 60 and 100 mm from the scatterer. Despite the fact that the beam structure is markedly disturbed after passage through a strong scatterer, at 100 mm from the scatterer we see that the first ring of the beam is nearly completely recovered. Of

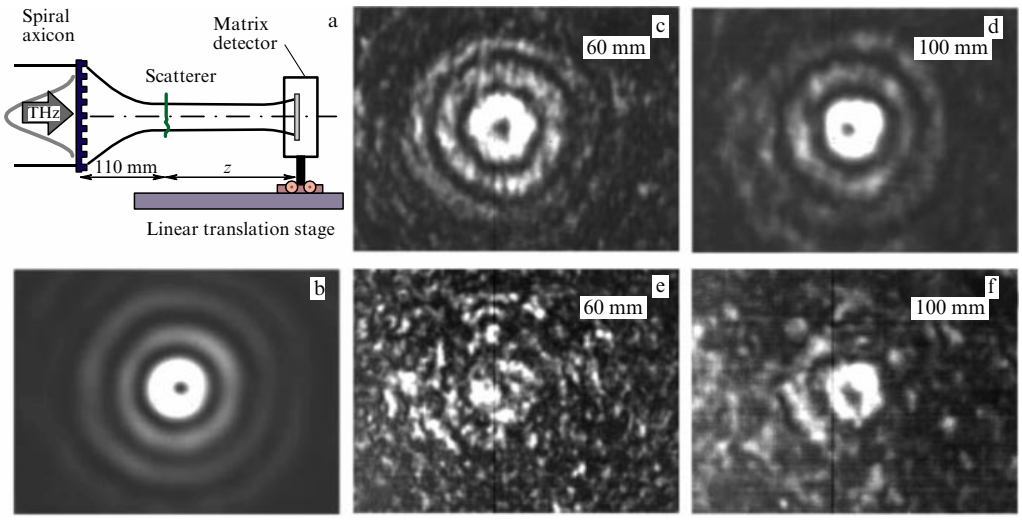

Figure 27. Schematic of the experiment (a) to investigate the self-recovery of a Bessel beam with $|\ell| = 1$ (b) formed by the spiral axicon and transmitted through scatterers of foamy polypropylene 3 mm (c, d) and 10 mm (e, f) thick.

course, the property of self-recovery exists only in the domain $z \leqslant z_A$ (see Table 1). However, calculations in Ref. [133] and subsequent experiments have shown that the 'diffraction-free' domain lengthens by a factor of $(f_2/f_1)^2$ with increasing beam radius by a factor of f_2/f_1 with the use of a telescopic system. These results allow us to assume that the terahertz or radio frequency band beams formed by a spiral axicon and expanded with a telescopic system may seemingly be employed for information transmission through turbulent media, which naturally calls for experimental confirmation. An advantage of long-wavelength radiation is lower Rayleigh and particle scatterings.

3.4.6 Rotation of a Bessel beam. The Poynting vector of twisted beams has an azimuthal component, and hence they may rightfully be termed 'rotating beams' [134–136]. For a linearly polarized Bessel beam, the energy flux is expressed as

$$\mathbf{S}(\rho) = S_0 J_\ell^2(\varkappa\rho)\left(\frac{\ell}{k\rho}\,\mathbf{e}_\theta + \mathbf{e}_z\right), \tag{132}$$

whence it is clear that its absolute value depends only on the radius. The derivative of the azimuthal angle θ of Poynting vector trajectory taken with respect to the longitudinal z-coordinate has the form

$$\frac{\mathrm{d}\theta}{\mathrm{d}z} = \frac{1}{\rho}\,\frac{S_\theta}{S_z} = \frac{\ell}{k\rho^2}\,. \tag{133}$$

From Eqn (133), we find the complete revolution of the Poynting vector about the axis:

$$\Delta z_{\mathrm{PitchCalc}} = \frac{2\pi k\rho^2}{\ell}\,. \tag{134}$$

The closer it is to the axis, the faster the revolution of the lines of energy flux. The outer beam rings revolve more slowly than the inner ones. Data from numerical simulations for beams obtained with the help of axicons (Fig. 28) suggest that the rates of inner ring revolution are equal to $(1.63 \pm 0.10)^\circ\ \mathrm{mm}^{-1}$ for $|\ell| = 1$ and to $(1.10 \pm 0.15)^\circ\ \mathrm{mm}^{-1}$ for $|\ell| = 2$. The turn lengths $\Delta z_{\mathrm{PitchSim}}$ calculated using these values are given in Table 2 along with the lengths calculated by Eqn (134). The experimentally observed beam rotation (see Fig. 30 in Section 3.6) coincides with the calculated one. Therefore, a small difference in the phase structures does not affect the beam characteristics. Similar experiments with twisted Laguerre-Gaussian and Bessel beams were performed in Ref. [137] in the visible domain with the use of an He–Ne laser. Interestingly, the lines of energy flux of Laguerre–Gaussian beams, unlike those of Bessel beams, are straight lines on the hyperboloid surface [22].

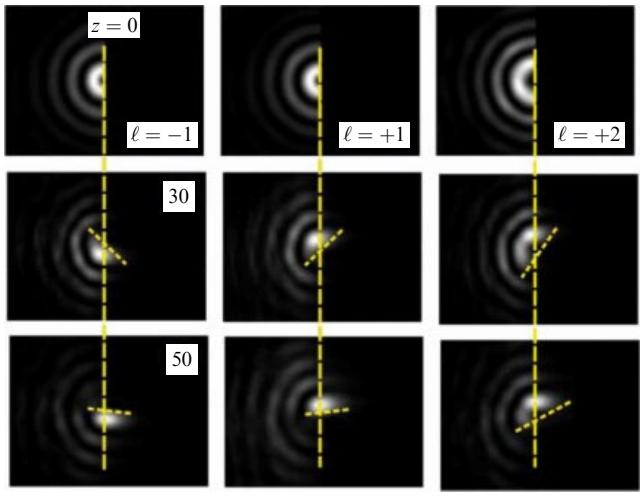

Figure 28. Rotation of Bessel beams possessing various topological charges upon diffraction by a half-plane (results of numerical simulations). The distances of the plane of observation from the half-plane are equal to 30 and 50 mm.

3.5 Diagnostics of twisted beams

When we are not dealing with time-domain spectroscopy (TDS), the imaging systems record beam intensity distributions. The presence of a singularity in a beam testifies, as a rule, to the presence of an optical vortex. However, determining the twistedness parameters requires finding the phase distribution. To date, a multitude of techniques have been demonstrated for determining the magnitude and sign of the

topological charge of a twisted beam. The parameters of twisted beams are commonly identified in classical diffraction experiments. To identify the values of the beam topological charge, different diffraction structures are presently used: a single slit [138, 139], a half-plane [86, 140], a round aperture [141]. Also employed to this end have been more complex structures: a triangular aperture [142] and arrays of many apertures [143, 144]. In our opinion, the simplest structures (the half-plane described above and Young diffraction by a double slit [87, 145, 146]) are the most convenient and intuitively intelligible way of determining the magnitude and sign of the topological charge.

In the diffraction of a twisted beam by a half-plane, the direction of its revolution (see Fig. 28) unambiguously defines the sign of its topological charge, but the angle of rotation is not measured very accurately. The topological charge is determined more accurately in the Young experiment. When a twisted beam is incident on the slits, for $a \ll z$ the interference fringes bend along the coordinate parallel to the slits in the following way [87]:

$$x(y,z) = -a \tan\left(\frac{2\pi a y}{\ell z \lambda} + \frac{u\pi}{\ell} + \frac{\pi}{2}\right), \quad u = 0, \ldots, \ell - 1 . \quad (135)$$

The fringe spacing $\Delta y = \lambda z/(2a)$ is independent of the topological charge, while the fringe bend increases with ℓ. Figure 29a shows the diffraction of our resultant beams by a double slit. The arrangement of the slits, with the incident beam intensity distribution superimposed on them, is depicted in Fig. 29c. In the case of a Bessel beam, the wave electric field on the screen is described by the expression

$$E(x,y) \approx \frac{2\mathrm{i}^{\ell}}{\sqrt{\lambda z}} \exp\left(\mathrm{i}kz + \mathrm{i}k\,\frac{a^2 + y^2}{2z}\right) \times \cos\left(\ell\varphi - k\,\frac{ay}{z} - \ell\,\frac{\pi}{2}\right) J_{\ell}\left(\varkappa\sqrt{x^2 + a^2}\right) . \quad (136)$$

The calculated intensity distributions agree nicely with the experimental ones (Fig. 29b). The calculated phase values are superimposed on the intensity distribution in the form of a color scale. One can see that the phase changes by π in the passage from one ring to another, as it must be in the case of a Bessel beam.

In experiments with broadband terahertz radiation [81, 82, 84] (time-domain spectroscopy), the result is immediately obtained in the form of amplitude and phase distributions in the beam, and additional measurements are not required. In experiments with monochromatic radiation in Ref. [83], the topological charge of a terahertz beam was determined using the transformation of a Laguerre–Gaussian beam to a Hermit–Gaussian one (Figs 22a–22e). This was effected through breaking the axial symmetry by inclining the imaging lens. In doing this, the beam transforms from an $LG_{0\ell}$ mode to an $HG_{0\ell}$ one, which permits determining the magnitude of the topological charge from the number of spots. However, the sign of this charge was determined in additional experiments to measure the direction of beam revolution with an irregularity introduced into the beam. In Ref. [85], the magnitude and sign of the topological charge were determined from the fork interference pattern emerging at the intersection of a twisted beam and an inclined Gaussian beam. These methods are evidently more complicated than the Young experiment, and so the latter is the method of choice.

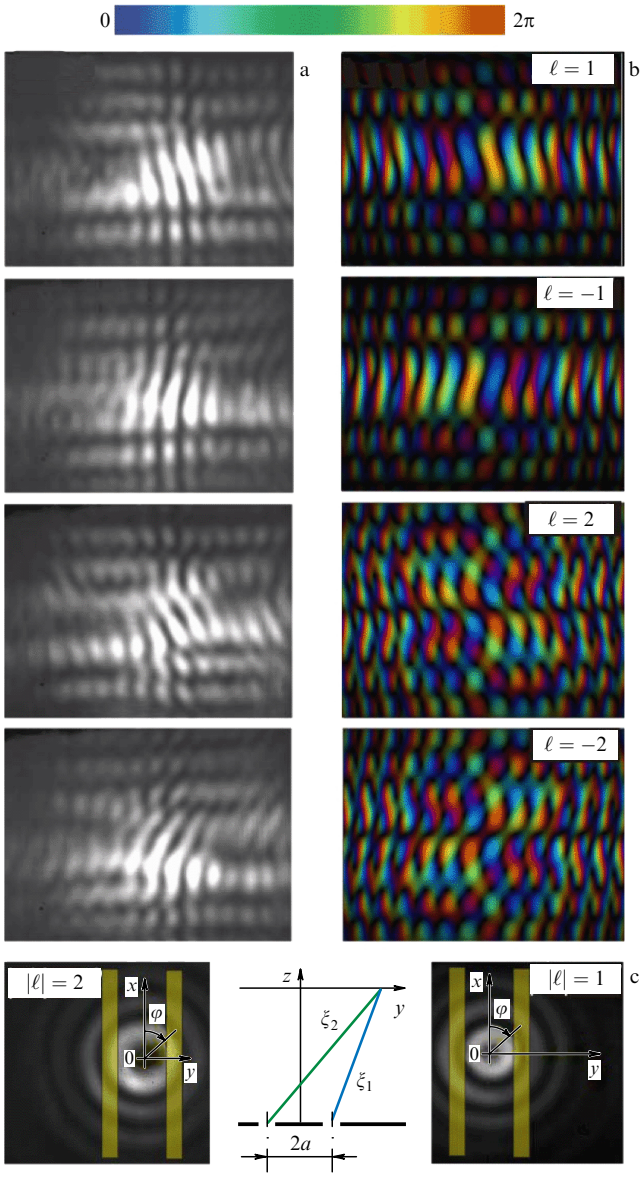

Figure 29. (Color online.) (a) Interference fringes recorded with a matrix detector at a distance of 40 mm from the slits. (b) Data of numerical simulations. The magnitude of the phase corresponds to the color scale in Fig. 25. (c) Employment of the Young configuration for determining the topological charge of the beams. The slits are spaced 4.5 mm apart.

3.6 Prospects for employing twisted terahertz beams

In Section 1.3.2, we spoke about different applications of beams with an orbital angular momentum. In the terahertz range, the history of such beams is only a few years old and the number of studies concerned with this subject is small for the present. The majority of them is dedicated to the problems of generating the beams and the development of their diagnostic techniques, and only in two experiments, which were performed by our team, twisted beams were used as a radiation source for experiments in other areas of optics. In this connection, we briefly outline the results of our experiments and discuss in what instances the use of twisted terahertz beams may offer advantages over the employment of twisted short-wavelength beams.

In many optical phenomena, an important role is played by surface plasmon-polaritons (surface electromagnetic waves) [147, 148], which have long been subjects of research

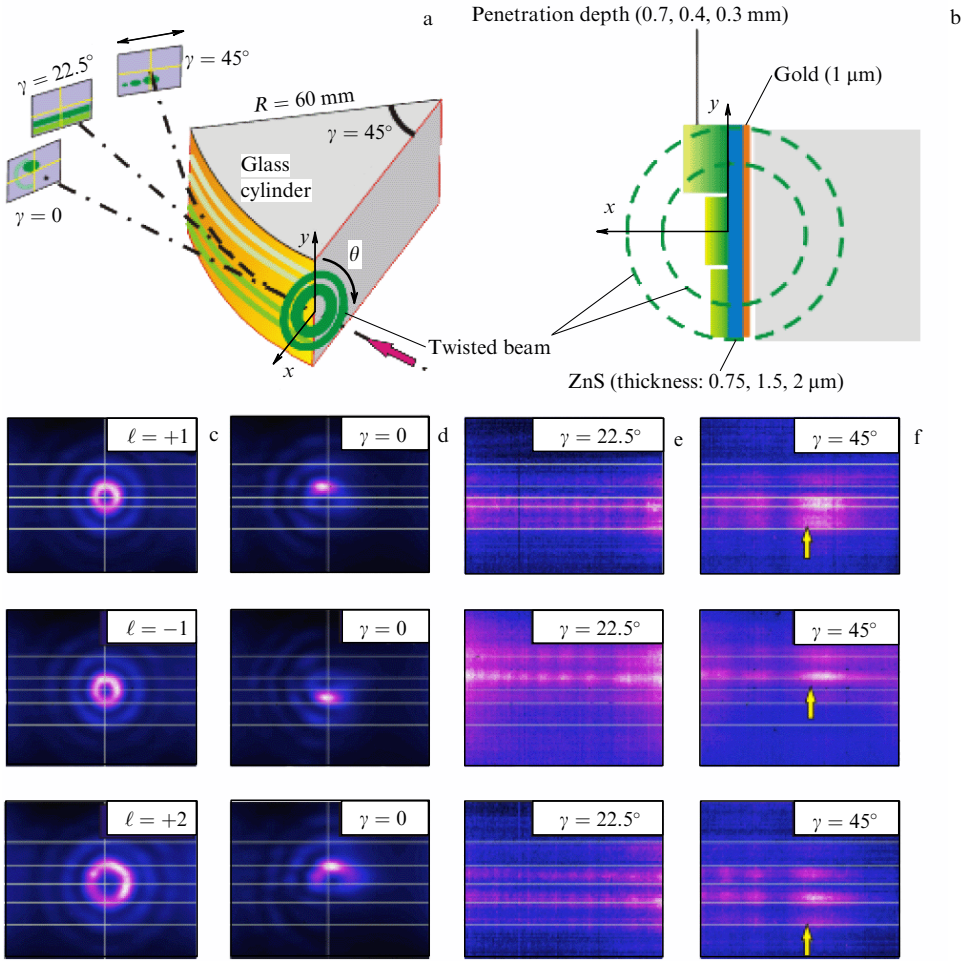

Figure 30. (Color online.) Plasmon generation by twisted beams for a wavelength of 141 μm. (a) Schematic of the experiment. Microbolometer array (MBA) was displayed to the three indicated positions such that the tangential distance from the corresponding surface points measured 70 mm. (b) Characteristic beam scale in comparison with the penetration depth of the surface electromagnetic wave to the air. Frames taken by the MBA: (c) beam incident on the sample end, (d–f) images recorded behind the sample, which was coated with a 1.5-μm thick ZnS layer, along the tangent to its surface at angles of 0, 22.5°, and 45° (the dashed–dotted lines in figure (a)).

and have enjoyed wide application in modern photonics [149–151]. While the plasmon propagation length in the visible range amounts to several dozen micrometers, in the terahertz range it is as long as several centimeters or tens of centimeters, depending on the thickness of the dielectric layer on a metal [152–154]. Another important property of terahertz plasmons is the capacity to 'jump' from one conducting surface to another [155] over a distance of up to 100 mm [156]. These two facts suggest that plasmons of the terahertz and infrared ranges may be employed to transmit information in integrated optical circuits. That is why, upon forming Bessel beams, we employed them for generating plasmon-polaritons [86].

The experiment is schematized in Fig. 30a. Plasmons were generated at the metal–dielectric–air interface in the diffraction of twisted Bessel beams by the sample's edge. This method of plasmon generation (end-fire coupling technique [157]) turned out to be convenient and quite efficient for terahertz radiation. The thickness of a ZnS layer on gold-coated samples, which were one eighth of a glass cylinder, ranged from 0.75 to 2 μm. Although the dielectric thickness was much smaller than the wavelength, dielectric deposition appreciably shortened the depth of penetration to the air for the exponentially decreasing field of the surface electromagnetic wave (SEW). The beam was normally incident on the end face of the sample. In the $\gamma = 0$ direction, one can see a diffraction pattern which is consistent with the beam rotation pattern obtained by numerical simulation and depicted in Fig. 28. At an angle $\gamma = 22.5°$, observed on the matrix detector is a fan of the radiation 'broken off' along the tangent to the surface arc, i.e., SEW radiation loss. The loss mechanism is discussed at length in Refs [153, 154]. The intensity of this radiation decreases smoothly with increasing angle, which was borne out in special experiments to measure its distribution with an acoustooptical detector. The interference fringes observed in Fig. 30d are an artifact — Fresnel diffraction inside the detector in the gap between the germanium window and the array of sensitive elements made of vanadium oxide. Lastly, seen in Fig. 30f ($\gamma = 45°$) is a free wave (indicated by an arrow), which results from the transformation of a surface plasmon that reaches the rear face of the sample. The diffraction pattern agrees nicely with the theoretical predictions [158].

The very fact that the surface plasmon emerges in the diffraction of an electromagnetic wave by the sample edge is trivial, and we describe this experiment because the plasmon production efficiency turned out to be dependent on the beam rotation direction. The images in Fig. 30d clearly testify in

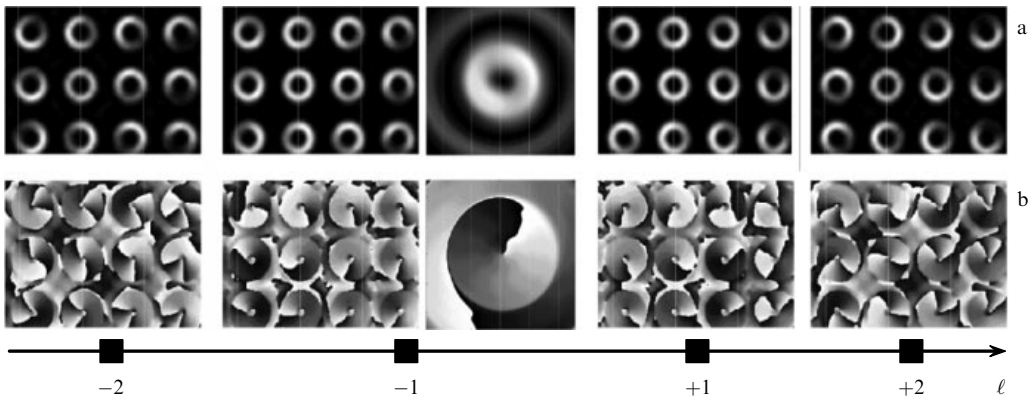

Figure 31. Periodic structures of twisted annular microbeams produced in the Talbot plane $z = L_T/2$ in the passage of Bessel beams, which are formed by spiral axicons and telescopically expanded five-fold, through an array (grating) of 1-mm diameter apertures with a period $p = 4$ mm. The wavelength is equal to 130 μm. (a) Intensity distribution. (b) Phase distribution. Shown in the central column are the intensity and phase of a Bessel beam with $\ell = -1$ incident on the copper grating. The phase values in the interval from 0 to 2π are color coded.

favor of the fact that the plasmon origin is preferred at the points of beam intersection with the interface, where the azimuthal component of the Poynting vector is aligned with the x-axis along the normal to the surface. This phenomenon has yet to be investigated in detail. However, in principle, considering the capacity of plasmons to 'jump' from surface to surface and the possibility of promptly switching the beam rotation direction, it may be used as a version of a 'plasmonic switch', maybe in other spectral regions as well. Control of plasmons is of considerable interest. By way of example, mention can be made of Ref. [159], which described a method to realize ultrafast all-optical NOT, AND, OR, and XOR operations with the use of interference effects in structures with dielectric crossed waveguides.

We found one more possibility of harnessing twisted Bessel beams. By irradiating a two-dimensional periodic array of round apertures by a beam expanded with a telescopic system, an array of twisted microbeams can be obtained in several Talbot planes. This phenomenon is analogous to the Talbot effect for twisted beams but depends on a greater number of parameters than the classical Talbot effect. The results of experiments and simulations of this effect are described in Ref. [160]. Figure 31 shows the intensity and phase distributions of a first-order ($\ell = -1$) Bessel beam incident on the array. The azimuthal microbeam phase distribution is opposite for a beam with $\ell = 1$. Interestingly, when use is made of the above axicons, for an incident beam with $|\ell| = 2$ the ring diameters are precisely the same as with $|\ell| = 1$, although the incident beam diameter is larger. One can see that this simple setup may be employed, for instance, to make regularly arranged optical traps for microparticles.

The angular momentum-to-energy flux ratio [see expression (132)], which may be written out with the inclusion of the spin angular momentum as [161]

$$\frac{|\mathbf{J}|}{c|\mathbf{P}|} = \frac{(\ell + \sigma_z)\lambda}{2\pi}\,, \tag{137}$$

where the radiation polarization, $-1 \leqslant \sigma_z \leqslant 1$, is proportional to the radiation wavelength. This circumstance makes advantageous the use of terahertz radiation in applications that involve angular momentum transfer to objects, for instance, for the rotation of microturbines [51]. 'Diffraction-free' Bessel beams may be employed for probing long objects which are partially transparent in the terahertz range, in inspection and security systems, as well as in multiplex communication systems [162].

4. Conclusions

Active theoretical and experimental research on twisted photon beams has been pursued for 25 years. Initially this work dealt only with the domain of light waves related to laser physics. At present, these investigations span a broad spectrum, from radio waves to X-rays. During this period, it became clear that twisted photons, which possess an additional degree of freedom, namely the projection of the total angular momentum onto the direction of motion, are new efficient tools of research, which may find wide use in different realms of physics. Furthermore, an original line of research involving the generation and application of twisted electrons emerged and gained impetus. Pioneering work on twisted neutrons has been carried out. In its infancy is the active study of the feasibility of generating twisted hadrons and of their role in nuclear and high-energy physics. Numerous reviews dedicated to specific issues pertaining to twisted particles have come out.

Our review touches upon a relatively small set of topics that have been actively explored in recent times (2013–2017) and have not been reflected in reviews. Furthermore, we restricted ourselves to primarily the discussion of those investigations in which we participated actively. And so we are in fact dealing with the following two major lines of research.

In Section 2, we reviewed recent theoretical work concerned with the fundamental interactions between twisted photons and atoms. When considering the photoexcitation and photoionization of atoms, we ascertained the linkage between the standard transition probabilities induced by plane-wave photons and the corresponding probabilities induced by twisted particles. We endeavored to reveal the new features of these processes connected with twisted photon participation: the emergence of new selection rules, the variation of excitation probabilities of individual sublevels, and changes in the angular distribution and polarization of final particles.

Section 3 was concerned with twisted photon beams in the terahertz spectral domain. Investigations in this area commenced only a few years ago, and we made the first attempt to

generalize the results obtained to date. One can see from our consideration that the methods of generating twisted terahertz beams are quite diverse: both quasioptical and diffraction elements. The large wavelength greatly facilitates the fabrication of diffraction optical elements and microantenna arrays employed for twisted beam formation. A typical disadvantage of the two is the fact that most of them are intended for operation at a certain wavelength. We showed that binary phase axicons (BPAs) with a spiral zone structure transform plane waves into twisted 'diffraction-free' Bessel beams with a prescribed topological charge in a broad spectral range. The cross section of the BPA-formed beams is the same for all wavelengths. This BPA property is especially valuable in wavelength-tunable radiation sources like free-electron lasers.

To date, the scope of research involving terahertz twisted beams has been primarily limited to the study of their production techniques and the investigation of their characteristics. We are inclined to think, however, that the nearest future will see practical applications of terahertz twisted beams. One of the physical factors that favor this inference is a linear increase in the angular momentum-to-energy flux ratio with the wavelength of a twisted beam, which may be employed in microturbines and optical traps. Our demonstrated feasibility of producing an array of twisted microbeams with an analogue of the Talbot effect, for instance, may be employed for making a periodic trapped microparticle array. In all likelihood, terahertz beams may also find application in multiplex communication systems.

In summary, it should be noted that we are at the beginning of a long and fruitful journey leading to the use of twisted terahertz beams and the application of twisted photons for studying light–matter interactions.

Acknowledgments

V G S acknowledges numerous helpful discussions with A V Afanasev, V A Zaitsev, I P Ivanov, G L Kotkin, and A Surzhikov. B A K expresses his sincere gratitude to N A Vinokurov, V N Zhabin, O E Kameshkov, G N Kulipanov, N D Osintseva, V S Cherkasskii, Yu Yu Choporova, and M A Shcheglov for their contribution to experiments, discussion of results, and preparation of original manuscripts; to B O Volodkin and V S Pavel'ev for the planning of experiments, calculation and fabrication of diffraction optical elements, and discussion of results; as well as to A M Shalagin and S K Turitsin for stimulating discussions. The reliable operation of the unique research facility, the Novosibirsk Free Electron Laser, in the course of experiments was provided by Ya V Getmanov, V V Kubarev, T V Salikova, D A Skorokhod, and O A Shevchenko. The papers whose results were presented in our review have been supported by the Russian Science Foundation under grant No. 14-50-00080 (Section 3) and the Russian Foundation for Basic Research under grant No. 15-02-06444 (Section 2). Used in this work was equipment at the Center of Collective Use supported by the Ministry of Education and Science of the Russian Federation (unique project identifier: RFMEFI62117X0012). The authors are grateful to A E Bondar, who initiated the writing of this review.

5. Appendix. Twisted electrons and neutrons

To make the picture complete, we give a brief description of twisted states for nonrelativistic electrons and neutrons, as well as for relativistic electrons. For definiteness, we will speak of twisted electrons. Below, we follow primarily Ref. [163].

In the *nonrelativistic* case, we use the Schrödinger equation for a free electron

$$-\frac{\hbar^2}{2m_\mathrm{e}}\,\nabla^2\Psi(\mathbf{r},t)=\mathrm{i}\hbar\,\frac{\partial\Psi(\mathbf{r},t)}{\partial t}\,, \tag{138}$$

where m_e is the electron mass. For a monochromatic wave of frequency $\omega=E/\hbar$,

$$\Psi(\mathbf{r},t)=\psi(\mathbf{r})\exp\left(-\mathrm{i}\omega t\right), \tag{139}$$

we obtain the Helmholtz equation

$$(\nabla^2+k^2)\,\psi(\mathbf{r})=0\,,\quad k=\frac{\sqrt{2m_\mathrm{e}E}}{\hbar}\,, \tag{140}$$

where E is the electron kinetic energy. The solution of equation (140) in the form of a *plane wave* with a certain helicity $\lambda=\pm1/2$ is of the form

$$\psi_{\mathbf{k}\lambda}(\mathbf{r})=w_{\mathbf{k}\lambda}\exp\left(\mathrm{i}\mathbf{k}\mathbf{r}\right). \tag{141}$$

Here, the two-component spinor $w_{\mathbf{k}\lambda}$ is the eigenfunction of electron helicity operator $\hat{\lambda}=\hat{\mathbf{s}}\mathbf{k}/k$:

$$\hat{\lambda}w_{\mathbf{k}\lambda}=\lambda w_{\mathbf{k}\lambda}\,, \tag{142}$$

where $\hat{\mathbf{s}}=\boldsymbol{\sigma}/2$ is the electron spin operator, and $\boldsymbol{\sigma}=(\sigma_x,\sigma_y,\sigma_z)$ are the Pauli matrices. In what follows, we conveniently expand this spinor in terms of the eigenfunctions $w^{(\sigma)}$ of the electron spin projection $\hat{s}_z$ onto the z-axis:

$$\hat{s}_z w^{(\sigma)}=\sigma w^{(\sigma)}\,,\quad \sigma=\pm\frac{1}{2}\,, \tag{143}$$

where

$$w^{(1/2)}=\begin{pmatrix}1\\0\end{pmatrix},\quad w^{(-1/2)}=\begin{pmatrix}0\\1\end{pmatrix},\quad w^{(\sigma')*}w^{(\sigma)}=\delta_{\sigma'\sigma}\,. \tag{144}$$

This expansion is of the form [compare with expression (25)]

$$w_{\mathbf{k}\lambda}=\sum_{\sigma=\pm1/2}\exp\left(-\mathrm{i}\sigma\varphi_k\right)d^{1/2}_{\sigma\lambda}(\theta_k)\,w^{(\sigma)}\,, \tag{145}$$

where $d^{1/2}_{\sigma\lambda}(\theta)=\delta_{\sigma\lambda}\cos(\theta/2)-2\sigma\delta_{\sigma,-\lambda}\sin(\theta/2)$. The electron flux density in the plane wave turns out to be a constant vector independent of coordinates and electron helicity:

$$\mathbf{j}=-\frac{\mathrm{i}\hbar}{2m_\mathrm{e}}\left[\psi^+_{\mathbf{k}\lambda}(\mathbf{r})\,\nabla\psi_{\mathbf{k}\lambda}(\mathbf{r})-\left(\nabla\psi^+_{\mathbf{k}\lambda}(\mathbf{r})\right)\psi_{\mathbf{k}\lambda}(\mathbf{r})\right]=\frac{\hbar\mathbf{k}}{m_\mathrm{e}}\,. \tag{146}$$

Cylindrical (Bessel) waves for a *twisted electron* may be constructed in the form of a superposition of spinor plane waves (141) by analogy with the twisted photon case (22):

$$\psi_{\varkappa mk_z\lambda}(\mathbf{r})=\int a_{\varkappa m}(\mathbf{k}_\perp)\,w_{\mathbf{k}\lambda}\exp\left(\mathrm{i}\mathbf{k}\mathbf{r}\right)\frac{\mathrm{d}^2k_\perp}{(2\pi)^2}\,, \tag{147}$$

$$\psi_{\varkappa mk_z\lambda}(\mathbf{r})=\sum_{\sigma=\pm1/2}\mathrm{i}^{-\sigma}\,d^{1/2}_{\sigma\lambda}(\theta_k)\,J_{m-\sigma}(\varkappa\rho)\exp\left[\mathrm{i}(m-\sigma)\varphi_r\right]\times w^{(\sigma)}\exp\left(\mathrm{i}k_z z\right). \tag{148}$$

In can be seen from formula (148) that the twisted electron resides a state with a certain longitudinal momentum $\hbar k_z$, transverse momentum modulus $\hbar\varkappa$, energy $\hbar\omega = E = \hbar^2 c^2(\varkappa^2 + k_z^2)/(2m_e)$, and helicity λ. Furthermore, individual terms

$$\exp\left[\mathrm{i}(m-\sigma)\varphi_r\right] w^{(\sigma)} \tag{149}$$

in sum (148) are the eigenfunctions of the operators $\hat{L}_z$, $\hat{s}_z$, and $\hat{J}_z = \hat{L}_z + \hat{s}_z$ with the eigenvalues $m-\sigma$, σ, and m, respectively. That is why the twisted electron also possesses a certain value $\hat{J}_z$ of the z-projection of the total angular momentum, equal to a half-integer $m = \pm 1/2, \pm 3/2, \ldots$. At the same time, the twisted electron is the superposition of states in which the z-projection $\hat{s}_z$ of the spin angular momentum assumes the values $\pm 1/2$, and the z-projection $\hat{L}_z$ of the orbital angular momentum assumes the integer values $m \mp 1/2$. The electron flux density along the z-axis in the Bessel wave depends on the coordinate ρ and quantum numbers:

$$j_z^{(m\varkappa k_z\lambda)}(\rho) = \frac{\hbar k_z}{m_e} \sum_{\sigma=\pm 1/2} \left[d_{\sigma\lambda}^{1/2}(\theta_k)\, J_{m-\sigma}(\varkappa\rho)\right]^2 . \tag{150}$$

We consider the generalization of these formulas to the case of *a relativistic twisted electron*. We will proceed from the plane-wave solution of the Dirac equation, corresponding to the state with a certain momentum $\hbar\mathbf{k}$, relativistic energy $\varepsilon = \hbar\omega = c(\hbar^2 k^2 + m_e^2 c^2)^{1/2}$, and helicity λ:

$$\psi_{\mathbf{k}\lambda}(\mathbf{r}) = u_{\mathbf{k}\lambda} \exp(\mathrm{i}\mathbf{k}\mathbf{r}) , \tag{151}$$

where $u_{\mathbf{k}\lambda}$ is the Dirac bispinor [78]:

$$u_{\mathbf{k}\lambda} = \begin{pmatrix} \sqrt{\varepsilon + m_e c^2}\, w_{\mathbf{k}\lambda} \\ 2\lambda\sqrt{\varepsilon - m_e c^2}\, w_{\mathbf{k}\lambda} \end{pmatrix}, \quad \bar{u}_{\mathbf{k}\lambda'} u_{\mathbf{k}\lambda} = 2m_e c^2 \delta_{\lambda'\lambda} . \tag{152}$$

The relativistic electron flux density in the plane wave turns out to be a constant vector:

$$\mathbf{j} = c\psi_{\mathbf{k}\lambda}^{+}(\mathbf{r})\, \boldsymbol{\alpha} \psi_{\mathbf{k}\lambda}(\mathbf{r}) = 2\hbar\mathbf{k}c^2 \tag{153}$$

(here, $\boldsymbol{\alpha} = (\alpha_x, \alpha_y, \alpha_z)$ are the Dirac matrices).

Cylindrical (Bessel) waves for *a relativistic twisted electron* are now obtained in the form of a superposition of these plane waves:

$$\psi_{\varkappa m k_z \lambda}(\mathbf{r}) = \int a_{\varkappa m}(\mathbf{k}_\perp)\, u_{\mathbf{k}\lambda} \exp(\mathrm{i}\mathbf{k}\mathbf{r})\, \frac{\mathrm{d}^2 k_\perp}{(2\pi)^2} , \tag{154}$$

and we find their explicit form with the use of expansion (145):

$$\psi_{\varkappa m k_z \lambda}(\mathbf{r}) = \sum_{\sigma=\pm 1/2} \mathrm{i}^{-\sigma}\, d_{\sigma\lambda}^{1/2}(\theta_k)\, J_{m-\sigma}(\varkappa\rho) \exp\left[\mathrm{i}(m-\sigma)\varphi_r\right] \times \exp(\mathrm{i}k_z z) \begin{pmatrix} \sqrt{\varepsilon + m_e c^2}\, w^{(\sigma)} \\ 2\lambda\sqrt{\varepsilon - m_e c^2}\, w^{(\sigma)} \end{pmatrix} . \tag{155}$$

The density of relativistic electron flux along the z-axis in a Bessel wave depends on coordinate ρ and quantum numbers and is not a positively defined function [compare with expression (42)]:

$$j_z^{(m\varkappa k_z\lambda)}(\rho) = 2\hbar k_z c^2 (2\lambda) \sum_{\sigma=\pm 1/2} 2\sigma \left[d_{\sigma\lambda}^{1/2}(\theta_k)\, J_{m-\sigma}(\varkappa\rho)\right]^2 . \tag{156}$$

Additional references and discussion may be found in Ref. [163].

References

1. Poynting J H *Proc. R. Soc. Lond. A* **82** 560 (1909)
2. Beth R A *Phys. Rev.* **50** 115 (1936)
3. Allen L et al. *Phys. Rev. A* **45** 8185 (1992)
4. Baranova N B, Zel'dovich B Ya *Sov. Phys. JETP* **53** 925 (1981); *Zh. Eksp. Teor. Fiz.* **80** 1789 (1981)
5. Vasara A, Turunen J, Friberg A T *J. Opt. Soc. Am. A* **6** 1748 (1989)
6. Bazhenov V Yu, Vasnetsov M V, Soskin M S *JETP Lett.* **52** 429 (1990); *Pis'ma Zh. Eksp. Teor. Fiz.* **52** 1037 (1990)
7. Bazhenov V Yu et al. *J. Mod. Opt.* **39** 999 (1992)
8. He H et al. *Phys. Rev. Lett.* **75** 826 (1995)
9. Fickler R et al. *Proc. Natl. Acad. Sci. USA* **113** 13642 (2016)
10. Bliokh K Y et al. *Phys. Rep.* **690** 1 (2017); arXiv:1703.06879
11. Clark C W et al. *Nature* **525** 504 (2015)
12. Afanasev A, Serbo V G, Solyanik M *J. Phys. G* **45** 055102 (2018); arXiv:1709.05625
13. Abramochkin E G, Volostnikov V G *Phys. Usp.* **47** 1177 (2004); *Usp. Fiz. Nauk* **174** 1273 (2004)
14. Abramochkin E G, Volostnikov V G *Sovremennaya Optika Gaussovykh Puchkov* (Modern Gaussian Beam Optics) (Moscow: Fizmatlit, 2010)
15. Torres J P, Torner L (Eds) *Twisted Photons* (*Application of Light with Orbital Angular Momentum*) (New York: Wiley-VCH, 2011)
16. Andrews D L, Babiker M (Eds) *The Angular Momentum of Light* (Cambridge Univ. Press, 2013)
17. Coullet P et al. *Opt. Commun.* **73** 403 (1989)
18. Korolenko P V *Soros. Obraz. Zh.* (6) 94 (1998)
19. Vasil'ev K, Kompanets P *Prostranstvennye Modulyatory Sveta* (Spatial Light Modulators) (Moscow: Radio i Svyaz', 1987)
20. Saleh B E A, Teich M C *Fundamentals of Photonics* (Hoboken, N.J.: Wiley Intersci., 2007); Translated into Russian: *Optika i Fotonika: Printsipy i Primeneniya* (Dolgoprudnyi: Intellekt, 2012)
21. Alekseev A N et al. *Tech. Phys. Lett.* **24** 694 (1998); *Pis'ma Zh. Tekh. Fiz.* **24** (9) 68 (1998)
22. Volyar A V, Shvedov V G, Fadeeva T A *Tech. Phys. Lett.* **25** 203 (1999); *Pis'ma Zh. Tekh. Fiz.* **25** (3) 87 (1999)
23. Kennedy S A et al. *Phys. Rev. A* **66** 043801 (2002)
24. Berry M V, Jeffrey M R, Mansuripur M *J. Opt. A* **7** 685 (2005)
25. Marrucci L, Manzo C, Paparo D *Phys. Rev. Lett.* **96** 163905 (2006)
26. Allen L, Padgett M *J. Mod. Opt.* **54** 487 (2007)
27. Wang X-L et al. *Phys. Rev. Lett.* **105** 253602 (2010)
28. Marrucci L et al. *J. Opt.* **13** 163905 (2011)
29. Mirhosseini M et al. *Opt. Express* **21** 30196 (2013)
30. Karpeev S V, Alferov S, Khonina S N *Opt. Eng.* **52** 091718 (2013)
31. Yu H et al. *Sci. Rep.* **3** 3191 (2013)
32. Mokhun I et al. *Appl. Opt. B* **53** 38 (2014)
33. Yu N, Capasso F *Nature Mater.* **13** 139 (2014)
34. Khonina S N, Almazov A A *Komp. Opt.* **24** 102 (2002)
35. Hemsing E et al. *Nat. Phys.* **9** 549 (2013)
36. Bekshaev A Ya, Bekshaev A S, Mohammed K A *Ukr. J. Phys. Opt.* **15** 123 (2014)
37. Sasaki S, McNulty I *Phys. Rev. Lett.* **100** 124801 (2008)
38. Afanasev A, Michailichenko A, arXiv:1109.1603
39. Bahrdt J et al. *Phys. Rev. Lett.* **111** 034801 (2013)
40. Jentschura U D, Serbo V G *Phys. Rev. Lett.* **106** 013001 (2011)
41. Jentschura U D, Serbo V G *Eur. Phys. J. C* **71** 1571 (2011)
42. Sakai Y et al. *Phys. Rev. ST Accel. Beams* **18** 060702 (2015)
43. Taira Y, Hayakawa T, Katoh M *Sci. Rep.* **7** 5018 (2017)
44. Katoh M et al. *Phys. Rev. Lett.* **118** 094801 (2017)
45. Hernández-García C et al. *Photonics* **4** 28 (2017)
46. Peele A et al. *J. Opt. Soc. Am. A* **21** 1575 (2004)
47. Leyser T B et al. *Phys. Rev. Lett.* **102** 065004 (2009)
48. Thide B et al. *Phys. Rev. Lett.* **99** 087701 (2007)
49. Soifer V A et al. *Phys. Part. Nucl.* **35** 733 (2004); *Fiz. Elem. Chastits At. Yadra* **35** 1368 (2004)
50. Ladavac K, Grier D G *Opt. Express* **12** 1144 (2004)
51. Ganchevskaya S V, Skidanov R V "The microturbine rotation by not circular light beam formed by vortex axicon" *CEUR Workshop Proc.* **1638** 24 (2016)

52. Klar T A, Engel E, Hell S W *Phys. Rev. E* **64** 066613 (2001)
53. Popiolek-Masajada A, Masajada J, Kurzynowski P *Photonics* **4** (2) 38 (2017)
54. Swartzlander G A et al. *Opt. Expr.* **16** 10200 (2008)
55. Lee J H et al. *Phys. Rev. Lett.* **97** 053901 (2006)
56. Tamburini F et al. *New J. Phys.* **14** 033001 (2012)
57. Willner A E et al. *Adv. Opt. Photon.* **7** 66 (2015)
58. Padgett M J *Opt. Expr.* **25** 11265 (2017)
59. Ivanov I P *Phys. Rev. D* **83** 093001 (2011)
60. Ivanov I P, Serbo V G *Phys. Rev. A* **84** 033804 (2011); *Phys. Rev. A* **84** 069906 (2011)
61. Matula O et al. *J. Phys. B* **46** 205002 (2013); arXiv:1306.3878
62. Varshalovich D A, Moskalev A N, Khersonskii V K *Quantum Theory of Angular Momentum* (Singapore: World Scientific Publ., 1988); Translated from Russian: *Kvantovaya Teoriya Uglovogo Momenta* (Leningrad: Nauka, 1975)
63. Scholz-Marggraf H M et al. *Phys. Rev. A* **90** 013425 (2014)
64. Peshkov A A et al. *Phys. Scripta* **91** 064001 (2016)
65. Picón A et al. *Opt. Expr.* **18** 3660 (2010)
66. Afanasev A, Carlson C E, Mukherjee A *Phys. Rev. A* **88** 033841 (2013)
67. Afanasev A, Carlson C E, Mukherjee A *J. Opt.* **18** 074013 (2016)
68. Afanasev A, Carlson C E, Solyanik M *J. Opt.* **19** 105401 (2017)
69. Rodrigues J D, Marcassa L G, Mendonca J T *J. Phys. B* **49** 074007 (2016); arXiv:1512.05933
70. Jáuregui R *Phys. Rev. A* **91** 043842 (2015)
71. Kaplan L, McGuire J H *Phys. Rev. A* **92** 032702 (2015)
72. Surzhykov A et al. *Phys. Rev. A* **91** 013403(2015)
73. Schmiegelow C T et al. *Nature Commun.* **7** 12998 (2016)
74. Afanasev A et al. *New J. Phys.* **20** 023032 (2018); arXiv:1709.05571
75. Picón A et al. *New J. Phys.* **12** 083053 (2010)
76. Serbo V G, Surzhykov A, Zaytsev V A "Ionization of hydrogenlike atoms by twisted photons: Going beyond the Born approximation", in preparation
77. Zaytsev V A, Serbo V G, Shabaev V M *Phys. Rev. A* **95** 012702 (2017); arXiv:1610.09648
78. Berestetskii V B, Lifshitz E M, Pitaevskii L P *Quantum Electrodynamics* (Oxford: Butterworth-Heinemann, 1999); Translated from Russian: *Kvantovaya Elektrodinamika* (Moscow: Fizmatlit, 2001)
79. Salvat F et al. *Comput. Phys. Commun.* **90** 151 (1995)
80. Muller R A et al. *Phys. Rev. A* **94** 041402(R) (2016)
81. He J X et al. *Opt. Express* **21** 20230 (2013)
82. Xie Z et al. *Sci. Rep.* **3** 03347 (2013)
83. Miyamoto K et al. *Appl. Phys. Lett.* **104** 261104 (2014)
84. Imai R et al. *Opt. Lett.* **39** 3714 (2014)
85. Wei X et al. *Appl. Opt.* **54** 10641 (2015)
86. Knyazev B A et al. *Phys. Rev. Lett.* **115** 163901 (2015)
87. Choporova Yu Yu et al. *Phys. Rev. A* **96** 023846 (2017)
88. Wu Z et al. *Opt. Express* **26** 1506 (2018)
89. Bliokh K Y et al. *Phys. Rev. A* **82** 063825 (2010)
90. Born M, Wolf E *Principles of Optics* (Oxford: Pergamon Press, 1968)
91. Guenther R D *Modern Optics* (New York: Wiley, 1990)
92. Dexheimer S L (Ed.) *Terahertz Spectroscopy. Principles and Applications* (Boca Raton: CRC Press, 2008)
93. Wang X et al. *Opt. Commun.* **283** 4626 (2010)
94. Yu N et al. *Science* **334** 333 (2011)
95. Vitiello M S et al. *Opt. Express* **23** 5167 (2015)
96. Vaks V L et al. *Phys. Usp.* **57** 684 (2014); *Usp. Fiz. Nauk* **184** 739 (2014)
97. Vaks V L et al. *Radiophys. Quantum Electron.* **59** 821 (2017); *Izv. Vyssh. Uchebn. Zaved. Radiofiz.* **59** 916 (2016)
98. Knyazev B A, Kulipanov G N, Vinokurov N A *Meas. Sci. Technol.* **21** 054017 (2010)
99. Seidel W et al. *38th Intern. Conf. Infrared Millimeter Terahertz Waves 2013* 1 (2013) https://doi.org/10.1109/IRMMW-THz.2013.6665462
100. Kulipanov G N et al. *IEEE Trans. Terahertz Sci. Technol.* **5** 798 (2015)
101. Soifer V A (Ed.) *Difraktsionnaya Komp'yuternaya Optika* (Computerized Diffraction Optics) (Moscow: Fizmatlit, 2007)
102. Goncharskii A V et al. *Vvedenie v Komp'yuternuyu Optiku* (Introduction to Computer Optics) (Moscow: Izd. MGU, 1991)
103. Durnin J *J. Opt. Soc. Am. A* **4** 651 (1987)
104. Goodman J W *Introduction to Fourier Optics* (San Francisco: McGraw-Hill, 1968); Translated into Russian: *Vvedenie v Fur'e Optiku* (Moscow: Mir, 1970)
105. Durnin J, Miceli J J (Jr.), Eberly J H *Phys. Rev. Lett.* **58** 1499 (1987)
106. Lin Y et al. *Appl. Opt.* **31** 2708 (1992)
107. Jiang Z, Lu Q, Liu Z *Appl. Opt.* **34** 7183 (1995)
108. McGloin D, Dholakia K *Contemp. Phys.* **46** 15 (2005)
109. Pyatnitskii L N *Volnovye Besselevy Puchki* (Besselian Wave Beams) (Moscow: Fizmatlit, 2012)
110. Simon D S "Bessel beams, self-healing, and diffraction-free propagation", in *A Guided Tour of Light Beams: From Lasers to Optical Knots* (Santa Clara, CA: Morgan Claypool Publ., 2016)
111. Duocastella M et al. *Laser Photon. Rev.* **6** 607 (2012)
112. Courvoisier F et al. *Appl. Phys. A* **112** 29 (2013)
113. Purnapatra S B, Bera S, Mondal P P *Sci. Rep.* **2** 692 (2012)
114. Bitman A, Moshe I, Zalevsky Z *Opt. Lett.* **37** 4164 (2012)
115. Ok G et al. *Sensors* **13** 71 (2013)
116. Busch S F et al. *J. Infr. Millimeter Terahertz Waves* **36** 318 (2015)
117. Mcleod J H *J. Opt. Soc. Am.* **44** 592 (1954)
118. Volodkin B et al. *Opt. Quantum Electron.* **48** 223 (2016)
119. Andreev N E et al. *Quantum Electron.* **26** 126 (1996); *Kvantovaya Elektron.* **23** 130 (1996)
120. Degtyarev S A et al. *Komp. Opt.* **38** 237 (1992)
121. Lavrent'ev M A, Shabat B V *Metody Teorii Funktsii Kompleksnogo Peremennogo* (Methods of the Theory of Complex Variable Functions) (Moscow: Nauka, 1987)
122. Landau L D, Lifshitz E M *Quantum Mechanics: Non-Relativistic Theory* (Oxford: Pergamon Press, 1977); Translated from Russian: *Kvantovaya Mekhanika: Nerelyativistskaya Teoriya* (Moscow: Nauka, 1989)
123. Dem'yanenko M A et al. *Appl. Phys. Lett.* **92** 131116 (2008)
124. Dem'anenko M A et al. *J. Opt. Technol.* **76** 739 (2009)
125. Dem'yanenko M A et al. *Optoelectron. Instrum. Data Process.* **47** 109 (2011)
126. Knyazev B A et al. *J. Infr. Millimeter Terahertz Waves* **32** 1207 (2011)
127. Knyazev B A et al. *EPJ Web Conf.* **149** 05001 (2017)
128. Choporova Yu Yu, Knyazev B A, Mitkov M S *IEEE Trans. Terahertz Sci. Technol.* **5** 836 (2015)
129. Arrizón V et al. *Opt. Lett.* **34** 1456 (2009)
130. Agafonov A N et al. *Optoelectron. Instrum. Data Process.* **49** 189 (2013)
131. Choporova Y Y et al. *EPJ Web Conf.* **149** 05003 (2017)
132. Knyazev B A et al. *41st Intern. Conf. Infrared Millimeter Terahertz Waves* (2016)
133. Choporova Y et al. *Phys. Procedia* **84** 175 (2016)
134. Allen L, Padgett M J *Opt. Commun.* **184** 67 (2000)
135. Berry M V, McDonald K T *J. Opt. A* **10** 035005 (2008)
136. Bekshaev A, Bliokh K Yu, Soskin M *J. Opt.* **13** 053001 (2011)
137. Arlt J *J. Mod. Opt.* **50** 1573 (2003)
138. Ghai D P, Senthilkumarana P, Sirohic R S *Opt. Laser Eng.* **47** 123 (2009)
139. Ferreira Q S et al. *Opt. Lett.* **36** 3106 (2011)
140. Masajada J *Opt. Commun.* **175** 289 (2000)
141. Kumar A, Vaity P, Singh R P *Opt. Commun.* **283** 4141 (2010)
142. Hickmann J M et al. *Phys. Rev. Lett.* **105** 053904 (2010)
143. Guo C-S, Yue S-J, Wei G-X *Appl. Phys. Lett.* **94** 231104 (2009)
144. Berkhout G C G, Beijersbergen M W *J. Opt. A* **11** 094021 (2009)
145. Sztul H I, Kartazayev V, Alfano R R *Opt. Lett.* **31** 2725 (2006)
146. Emile O, Emile J *Appl. Phys. B* **117** 487 (2014)
147. Agranovich V M, Mills D L (Eds) *Surface Polaritons: Electromagnetic Waves at Surfaces and Interfaces* (Oxford: Oxford Univ. Press, 1982)
148. Maier S A *Plazmonika: Teoriya i Prilozheniya* (Plasmonics: Theory and Applications) (Moscow–Izhevsk: RKhD, 2011)
149. Klimov V *Nanoplasmonic*s (Boca Raton, FL: CRC Press, Taylor and Francis Group, 2014); Translated from Russian: *Nanoplazmonika* (Moscow: Fizmatlit, 2010)
150. Remnev M A, Klimov V V *Phys. Usp.* **61** 157 (2018); *Usp. Fiz. Nauk* **188** 169 (2018)

151. Novotny L, Hecht B *Principles of Nano-Optics* (Cambridge: Cambridge Univ. Press, 2006); Translated into Russian: *Osnovy Nanooptiki* (Moscow: Fizmatlit, 2009)
152. Jeon T-I, Grischkowsky D *Appl. Phys. Lett.* **88** 061113 (2006)
153. Gerasimov V V et al. *J. Opt. Soc. B* **30** 2182 (2013)
154. Gerasimov V V et al. *J. Opt. Soc. B* **33** 2196 (2016)
155. Nazarov M et al. *Opt. Commun.* **277** 33 (2007)
156. Gerasimov V V et al. *Opt. Express* **23** 33448 (2015)
157. Stegeman G I, Wallis R F, Maradudin A A *Opt. Lett.* **8** 386 (1983)
158. Kotelnikov I A, Gerasimov V V, Knyazev B A *Phys. Rev. A* **87** 023828 (2013)
159. Birr T et al. *Opt. Express* **23** 31755 (2015)
160. Knyazev B et al. *Opt. Express* **26** 14174 (2018)
161. Heckenberg N R et al., in *Optical Vortices* (Horizons in World Physics, Vol. 228, Ed. M Vasnetsov) (Hauppauge, NY: Nova Sci. Publ., 1999) p. 75
162. Gatto A et al. *J. Opt.* **13** 064018 (2011)
163. Serbo V G et al. *Phys. Rev. A* **92** 012705 (2015); arXiv:1505.02587